Facial Age Analysis using an Absorptive Rough Laminar Light Scattering Model

Hadi Affendy Bin Dahlan

Doctor of Philosophy

University of York

Computer Science

November 2017

Dedication

To My Family, My Supervisor, and My Colleagues

Abstract

Facial aging research concerns the way aging affects a person's appearance and how we can use knowledge of this process. It has been an interesting topic for fields such as human perception, pattern recognition, computer vision, graphics, and skin optics. Most studies acknowledge that facial appearance changes with age. As a person grows older, certain characteristics of their skin will change, notably the light scattering. If a model is used to predict a person's skin light scattering, its parameter(s) may be used to predict the age of its owner. The aim of this thesis is to observe whether a light scattering model parameter is suitable to be used as an age estimator/classifier. This is done by investigating and analyzing the relationship between the parameter of an analytical-based light scattering model and skins of various ages (henceforth, this will be called "the parameter-age test"). Thus, for this parameter-age test, new laminar light scattering models are introduced, which include an absorption term that is defined using the rule of light energy conservation (reflectance, transmission, and absorption). Multiple models (including the new models) are used to investigate the relationship between the model parameters and the subject's age. The final results show that all of the models' roughness parameters have the significant positive correlation with age ($p < 0.05$), making it a suitable parameter to be used for estimating/classifying age. This has been proven in this thesis age classification experiment using the estimated roughness parameters. In the end, this thesis has shown that the parameter(s) for an analytical-based light scattering model can be used as an alternative method for estimating/classifying a person's age. Moreover, it can also be used to work with other age extractor/estimator/classifier, for the purpose of designing a more robust age estimation/classification method.

Contents

Abbreviations and Symbols

Abbreviations:

AAM Active Appearance Model

AGES Aging Pattern Subspace

ASM Active Shape Model

BIF Biologically Inspired Features

BRDF Bidirectional Reflectance Distribution Function

BSSRDF Bidirectional Surface-Scattering Distribution Function

CUReT Columbia-Utrecht Reflectance and Texture

DOP Degree of Polarization

LBP Local Binary Pattern

MFDA Multi-Feature Discriminant Analysis

PCA Principle Component Analysis

RMS Root Mean Square

SIFT Scale Invariant Feature Transform

SVM Support Vector Machine

UTIA Ústav Teorie Informace a Automatizace

Symbols:

L	Light radiance
θ	The zenith angle
ϕ	The azimuth angle
σ/T	Surface Root-Mean-Square slope
σ'/T'	Subsurface Root-Mean-Square slope
K_G	Coefficients for the surface equations of Gaussian
K_E	Coefficients for the surface equations of Exponential
$d\omega'$	Solid angle under mean surface level
n	Standard refractive index
β	Balance parameter
Rf	Reflectance
Tr	Transmission
Ab	Absorption
a	Absoption percentage
Δ_{RMS}	Root-Mean-Square fitting error
ρ	Degree of polarization
k_{model}	Model coefficient

List of Tables

List of Figures

Acknowledgements

My utmost gratitude to my supervisor Professor Edwin R. Hancock for his guidance and patience. I may not have gone far without his excellent supervision. I am also grateful to Dr. William Smith for providing me constructive and technical advice regarding my research problem. Moreover, I am grateful to my father who encouraged me to complete my studies until the end, and to my mother who keeps reminding me to stay focused. I would also like to thank my siblings who support me intellectually, even though they have their own studies to complete. My colleagues deserve to be acknowledged for sharing their experience and knowledge with me. In particular, I would like to thank those who have given their time to become volunteers for my research. Finally, thanks to my sponsorship, Majlis Amanah Rakyat (MARA) of the Malaysian government, who granted me the needed financial support.

Declaration

I declare that this thesis is a presentation of original work and I am the sole author. This work has not previously been presented for an award at this, or any other, University. All sources are acknowledged as References.

Some parts of this thesis have been published in conference proceedings; where the author of this thesis is responsible for the material presented here. For each published item the primary author is the first listed author.

- H. A. Dahlan and E. R. Hancock, "Absorptive scattering model for rough laminar surfaces," 2016 23rd International Conference on Pattern Recognition (ICPR), Cancun, 2016, pp. 1905-1910. [10]

- H. A. Dahlan, E. R. Hancock and W. A. P. Smith, "Reflectance-aware optical flow," 2016 23rd International Conference on Pattern Recognition (ICPR), Cancun, 2016, pp. 2860-2865. [11]

Chapter 1

Introduction

Facial aging is a complex process, but a human has the capability to estimate the age of others accurately most of the time. This is usually done by just observing a person's facial appearance. Most literature on facial aging has shown that age can be estimated by just observing the changes in the craniofacial shape and the face texture [25, 82, 86]. However, how does this change affect the skin light scattering? Researchers have discovered that the inner characteristics of the skin, such as the dermis and the epidermis layers, will change with age [20,22,39,112], which means that the light scattering on the skin may also change in some way. Can this change be modeled with a light scattering model? And can the model be used as an alternative method to estimate the age?

Computer vision and graphics field provide, amongst other, techniques for creating a light reflecting/scattering model that can make near photo-realistic graphical image of a given object. Most of these models can also be used to render human skin. In this case, the model parameters were defined to be either statistical or empirical. These parameters are the ones that control the outgoing radiance behavior, hence, the ones that may be affected by the skin aging, making them a potential tool to estimate a person's age. Nevertheless, very few authors have thoroughly investigated the relation between their model parameter(s) and the age of the person (whose skin is) modeled. The reason is that most model parameters are difficult to measure directly, especially skin traits such as the refractive index, hence, some authors [36, 53, 81] usually made them into a constant value based on other sources. It would be interesting to analyze how these traits can affect the light reflectance/scattering model. The information obtained from the study can be beneficial not only in the computer vision but also to other fields as well, such as the pattern recognition and the skin optic.

In this thesis, the author investigates how the aging affects the parameter(s) of a light scattering model. This is done by analyzing the correlation results between the subject age and the estimated parameter(s). In the experiment, the parameter(s) are estimated by fitting the model to the skin light scattering measurements. Moreover, the new model will also be tested on other materials to observe its model fitting and rendering accuracy. Figure 1.1 shows the area that this research is focused on.

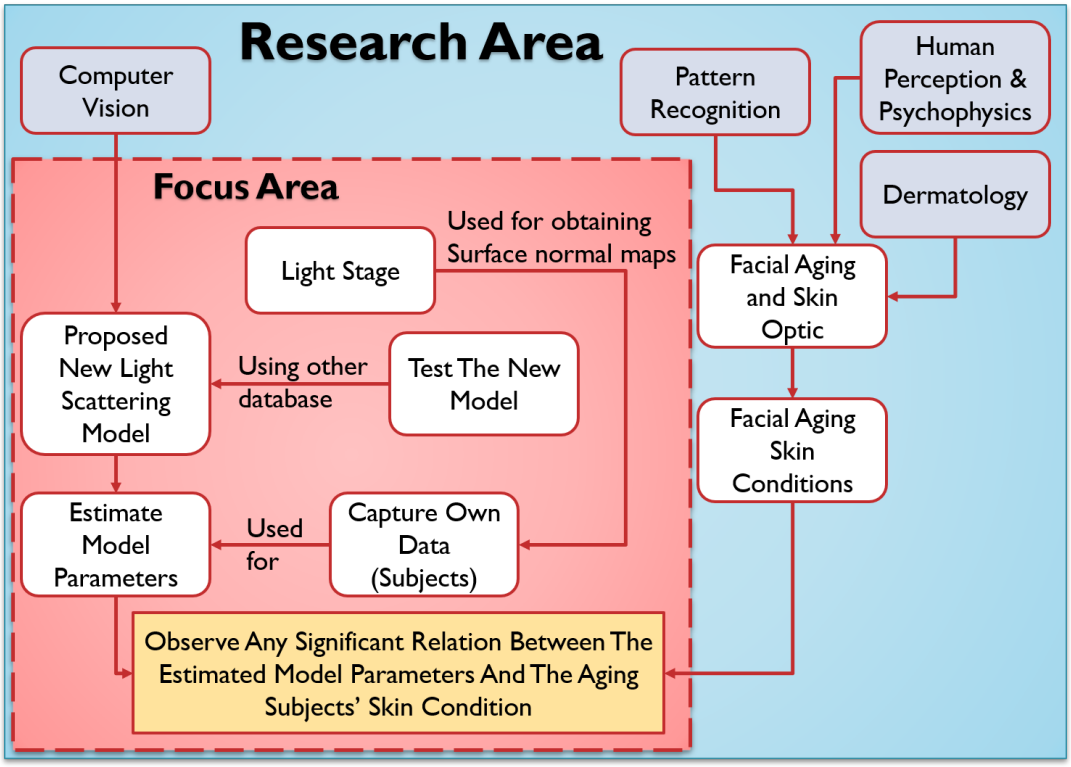

Figure 1.1: Focus Research Area

1.1 Problem Statement

How does facial aging affect the light scattering on the facial skin? What model will be used in the study? What relation will the model parameter have with the skin trait (e.g. surface roughness or refractive index)? Which parameter(s) effect the aging? Would the parameter behave similarly to what one would expect - e.g. would the model roughness parameter value increase with aging? How would the model fare as a standard light scattering model when applying on materials that are not skin?

1.2 Aim

The aim of this thesis is to investigate and analyze the relationship between the parameter of an analytical-based light scattering model and the different aging skins; for the purpose of observing whether the parameter is suitable to be used as an age estimator/classifier. Multiple models will be selected and compared against each other; this includes the new light scattering model that will be presented in this thesis. Additionally, the new model will also be tested on other materials to observe its model fitting accuracy.

1.3 Research Contributions

The novel contributions of this study are:

- Presenting a new absorptive laminar light scattering model that can be used for statistical analysis.
- Testing the functionality and the accuracy of the new model using both the isotropic (CUReT database) and anisotropic (UTIA database) samples.
- Making a justifiable relation between the model parameters and the characteristic of the sample, such as the sample degree of polarization (DOP).
- Presenting and testing a new image alignment technique for aligning image sequence captured in disparate illumination environments.
- Making correlation analysis between the subject age and the model parameters. The test is done using the newly proposed models and four other model, for comparison. Later identified and highlighted results that agree with the skin optic, human perception, and computer vision literature.

1.4 Brief Thesis Structure

Chapter 2 first explores some facial aging discoveries from the perspective of Human Perception and Psychophysics field. Afterward, the chapter will continue reviewing several works of literature regarding reflectance and scattering model progression until the current studies that mainly focus on the studies of light scattering models for human skin. In Chapter 3, the new model is introduced and explained thoroughly. The new absorption

term is defined in this chapter and its importance is mentioned. The evaluation of the model is also included in the chapter by comparing it with other models using available databases.

Next, Chapter 4 explains how we select the appropriate parameters for an investigation. The chapter also describes the experimental setup and its pre-processing step. Additionally, a new image alignment technique is presented in this chapter. Afterward, Chapter 5 will be the main experiment, which is the correlation test between the subject age and the interest parameters. The analysis will be focused on any significant results, behaviours or other unforeseen circumstances. Finally, Chapter 6 concludes the overall thesis and evaluates any shortcoming of the experiment for future improvement.

1.5 Summary

Most pattern recognition, computer vision, and graphics that studies facial aging know that the facial appearance will change with age. However, few have studied the aging effects on the skin light scattering. A light scattering model parameter has a potential to be used as an alternative method to estimate facial age. But can it really be used as a tool to estimate a person's age? Moreover, if a model parameter is used to control the skin light scattering behavior, how are the different aging skins going to affect these parameter(s) and how strongly they are affected? These are the questions this thesis tries to answer. Additionally, the new model will also be tested on other sample materials to observe how good the new model is when it is used as a standard light scattering model and find its limitation when tested on the different type of samples.

Chapter 2

Field Survey and Review

Facial aging is an interesting topic that has been studied by various authors from multiple fields. The knowledge gleaned from the studies can be used in numerous real world settings, such as in plastic surgeries, biometrics, criminology, and even animation. Nevertheless, there is still more that we need to learn because facial aging is a very complex process. As mentioned above, the aim of this thesis is to investigate and analyze the light scattering behavior of the facial skin for subjects of different ages, using a light scattering model. This will allow us to explore an alternative method of estimating a person's age using the model parameters and also, to further understand how aging of the skin affects the light scattering. A review of the relevant literature and related works will be conducted prior to the experiment. This is so the process surrounding the development of the problem statement can be explained in sequential order.

The author will first review facial aging literature from specific related fields, starting with the Medical, Skin Optics, Human Perception, Psychophysics, Computer Science, and Pattern Recognition fields. This is so we can understand what previous authors have discovered about facial aging and what information is lacking or requires further evaluation. In the remaining sections of this chapter, the author will review some of the light reflectance and scattering model studies completed by academics in the Computer Vision and Graphics field. Facial skin reflectance studies have also been included in the review. At the end of this chapter, the author will outline the problem statement that this thesis intends to address.

2.1 Face Aging Research

Estimation of a person's age based on their face play an important role in everyday communication and human social activity generally. People have the instinctive capability to estimate the age of others. Assigning this ability into a machine capable of learning and applying it to a wide variety of fields, such as in law enforcement, security control, soft-biometric access system, and even in the entertainment industry, has been an interesting and important development. In recent years, there has been a positive progression in facial aging research, especially in the fields of human perception, psychophysics, computer science, and pattern recognition.

2.1.1 Face Aging Research in Medical, Skin Optics, Human Perception and Psychophysics Fields

The innate ability of humans to estimate a person's age based on observations of the facial appearance is impressive. This ability has been explored by members of the Human Perception and Psychophysics fields in an effort to find a method to convey it as an algorithm for a machine to learn. From their studies, multiple facial traits that help determine a person's age have been identified, including shape of the face, skin texture, skin features, and skin color contrast [86, 112].

The two following predetermined features are the main features that contribute to the perception of chronological aging by others: 1) The face shape changing, in particular the cranium bones grow as time passes. This occurs predominately during the transition from childhood to the adult stage, and; 2) The face develops wrinkles (or face texture), as facial muscle wastes due to decreasing elasticity. This occurs during the transition from adulthood to the senior stage [25, 83, 84, 112]. Figure 2.1 shows both of these facial aging features. This information is important for both humans and machines when deciding which facial signature to use in order to estimate age any stage (e.g. child to adult or adult to senior) and, indeed, these features have been used by the computer science and pattern recognition fields during the construction of face age synthesis systems or a face age estimator systems.

The physiological aging of the human body is also an important consideration. In addition to the chronological aging process, there are two physiological forces that can cause the face to age progressively or regressively. They are the internal force (e.g. genetic, gender, ethnic, body fat) and the external force (e.g. dietary habit, smoking, climatic

condition, exposure to the sun) [25, 84, 87].

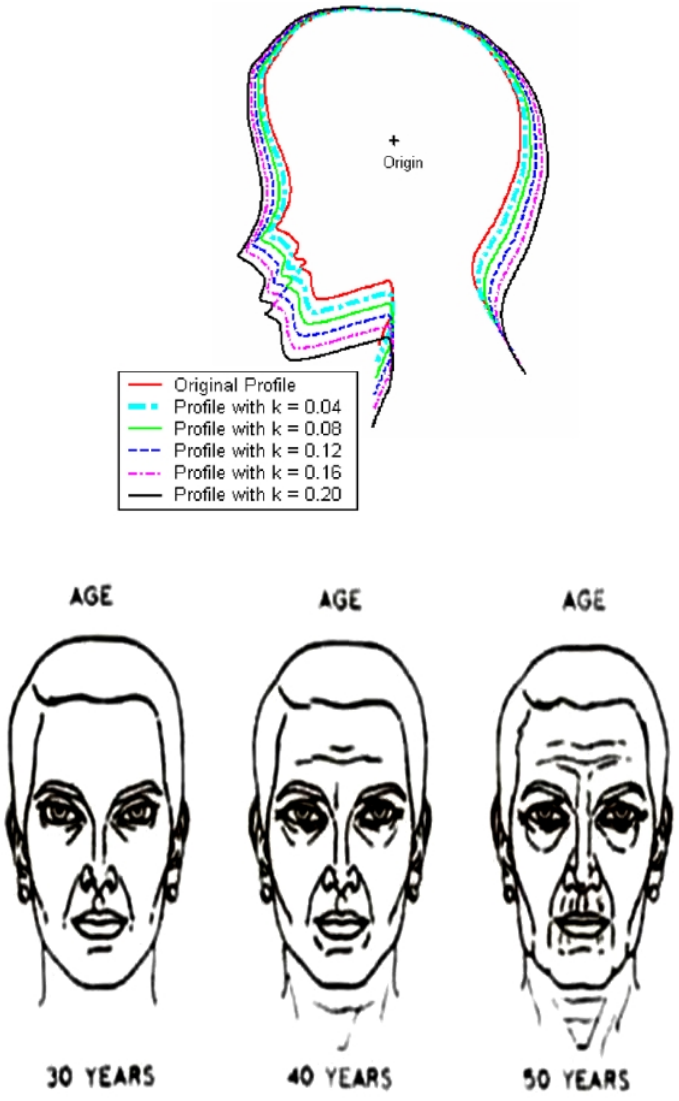

Figure 2.1: The facial aging in term of shape or craniofacial growth (top) and texture (bottom). Images taken from [25, 84, 112]

Skin is the outermost tissue and the largest organ in a human body with many components and complex structures being evident in its layers. The visual properties of the skin depend on the constituent components in the skin. As light shines upon the skin, reflectance can be viewed as a result of the combined effect of the optical phenomena induced by the physio–anatomical components of all the skin layers, with each component emitting a specific optical effect [2, 3, 71]. As a person grows older, internal and external forces act upon the outer and inner skin causing some level of retardation, which later changes the appearance of the skin and its light scattering. This is demonstrated in [20,22],

wherein the young skin was perceived to have different color contrast and luminosity than the older skin.

Healthy, young skin has a smooth, uniformly fine texture that reflects light evenly. It is also plumper and emits radiant color. Meanwhile, aged skin tends to be rough and dry, with more wrinkles, freckles, and age spots, and tends to emit dull color [20, 22, 39, 112]. Additionally, in one study on age estimation using viewer quantitative surveys done by Fink et al. [22], the authors discovered that the concentration and distribution of the chromophores, have a strong correlation with age, implying that their distribution prompts the majority of tone dependent age perceptions.

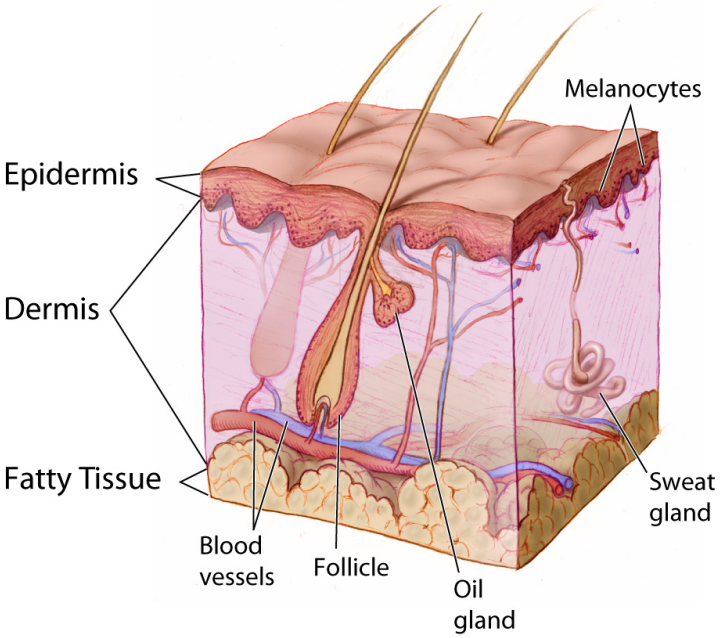

Figure 2.2: The general structure of the skin. (Image illustrate by Don Bliss [40])

Chromophores control the pigment concentration in the skin. The two chromophore components that affect the brightness and the reflectance colour are melanin and hemoglobin. Melanin is located in the bottom layer (the stratum basale) of the skin's epidermis and is perceived as the brown colored pigment, which is responsible for the different tones in skin (ethnicity) and tanning. While the hemoglobin, which is located within blood vessels, contribute to the highly diffuse bloom of pink coloration evident in the skin when it is carrying oxygen. Meanwhile, collagen is one of the components responsible for scattering the

light back out from the skin like a mirror [20, 22, 39, 112]. Young, healthy skin would have an even distribution of pigment concentration and collagen in the skin. However, as the age increases chronologically and as a result of multiple injuries from external forces, such as excessive sun exposure, the chromophores and collagen distribution in the skin become disturbed, ultimately resulting in uneven concentration, damaged cells, reduction of cell density, and drop in skin elasticity [17, 72, 96, 97]. This later produces aging features (e.g. wrinkles, age spots and elastosis), including skin contrast, dull luminosity complexion and uneven light diffusion. [20, 22, 47, 51, 62, 91, 112].

2.1.2 Face Aging Research in Computer Science and Pattern Recognition Field

The discoveries made within the Medical, Human Perception and Psychophysics fields have been applied in the construction of the face aging system in the Computer Science and Pattern Recognition fields, where different frameworks and methodologies have been constructed to create robust and accurate facial aging systems. There are two uses for common facial aging research in the field of computer vision and pattern recognition. They are: 1) face age synthesis focusing on aesthetically rendering the facial image to be either younger or older than its original; and 2) face age estimation exploring a method to estimate the age of a person pictured in a given image by labeling it either as a function of age group (certain age range) or by their true age [25, 84].

Face age synthesis typically uses research to replicate the facial aging model. It often begins with the construction of a generic face model, in which the face model type can be an empirical or knowledge-based, and then uses either shape or texture to synthesize a target aging appearance [31, 61, 75, 76, 82, 102]. They can include other aging features, such as age spots and freckles. This shows that using the skin color contrast can also help determine the age of the skin. However, these authors did not specifically analyze the light reflectance behavior of facial skin of various ages. Table 2.1 displays some of the face age synthesis literature.

Meanwhile, face age estimation studies have tended to focus on developing accurate age estimators. This is usually done by introducing a combination of one or more feature extractors and machine learning methods. One of the early studies was conducted by Kwon and Lobo [54] who created three categories of age - infant, adult, and senior. It is one of the earlier studies that considered the different facial shape features and texture

Table 2.1: Several Age Synthesis Representations

Author(s)	**Representation**	**Additional Note(s)**
Lanitis, Taylor and Cootes, 2002 [55]	Face Shape:- Active Appearance Model (AAM)	Extended AAM for facial aging to obtained shape and texture simultaneously while also constructing aging function in term of PCA (Principle Component Analysis)
Ramanathan and Chellappa, 2006 [82]	Face Shape:- Using the ratios for their Craniofacial growth model	Revised the cardioidal strain transformation on the child face profile
Wang et al., 2006 [103]	Face Shape:- Active Shape Model (ASM)	Used aging function with polynomial structure to indicate relationship between the feature vector and age
Suo et al. 2007 [93]	Face Texture/Features:- High resolution facial components using AAM, Gabor wavelets and Blobs (for wrinkle and pigment)	Followed a grammatical face model method and enhanced it with age and additional hair features.
Li, Park and Jain, 2011 [57]	Face Features:- Scale invariant feature transform (SIFT) and multi-feature discriminant analysis (MFDA)	Used the discriminative analysis method with densely sampled local descriptor scheme.
Kemelmacher-Shlizerman, Suwajanakorn and Seitz, 2014 [46]	Face Shape, Texture and Illumination:- Averaging image subspace and Illumination subspace flow	Accounting for pose, expression, and illumination.

Table 2.2: Several Age Estimation Representations

Author(s)	**Representation**	**Additional Note(s)**
Kwon and Lobo, 1996 [54]	Face Shape and Texture:- Anthropometric Model (Ratios) and Snakelets	Used face ratios (shape) to estimate infant compared to adult, and snakelets (wrinkle) to estimate adult compared to senior.
Geng, Zhou and Smith-Miles, 2007 [28]	Face Shape and Texture:- Aging Pattern Subspace (AGES)	Implemented AAM to represent pattern sequence of same individual in progressing age. However, texture wasn't encoded well.
Fu, Xu and Huang, 2007 [26]	Face Features:- Low-dimensional representation in the embedded subspace	Utilized an aging pattern developed after analyzing many individuals at specific ages.
Choi et al., 2011 [9]	Face Shape and Texture:- AAM, Gabor filter and Local Binary Pattern (LBP)	Extracted multiple features using AAM (shape); Gabor (wrinkle); and LBP (skin texture e.g. spots).
Han et al., 2015 [35]	Face Shape and Texture:- biologically inspired features (BIF)	Presented a generic framework for automatic demographic (age, gender and race) estimation from a given face image.

features that enable the differentiation of a child from an adult, and an adult from a senior.

In the past decades, researchers have introduced various age estimation methods. The method usually consists of one (or more) feature extractors and one (or more) age classifiers (or estimators). Certain feature extractors can only extract specific facial aging signatures, which can be either holistic (e.g. facial shape and texture), local (e.g. the aging wrinkle or the hair color), or a combination of both. However, none so far have considered using the skin light scattering as an aging feature. Table 2.2 tabulates some of the reviewed face age estimation studies.

Overall, facial age can be estimated by just observing the structure of the skull and/or the skin texture. Nevertheless, most of these authors did not thoroughly analyze the affect of aging on the light reflectance/scattering. It is important to understand the change in reflectance as a function of aging since it can broaden our knowledge on facial skin morphology, which has potential applications in a number of fields.

2.2 Reflectance and Scattering Model

Throughout the search for a reflectance model for human skin, authors from the computer vision and graphics fields have constructed an appropriate skin reflectance model based on statistical and analytic discoveries. This helps current animators tremendously in their efforts to render realistically looking 3D actors in their films. Most reflectance models need specific parameter(s) values for them to produce the desired radiance output. These values can be either measured directly or based on skin optics literature.

As mentioned in Section 2.1, aging affects facial features, especially the skin texture. This might produce different light scattering results for people of different ages, which means that the standard skin reflectance model might not predict these changes properly. After analyzing the literature regarding facial aging, it can be hypothesized that the changes in the skin due to aging may have a certain correlation with the behavior of skin diffuse reflectance. One such trait is the surface roughness, which is a feature most computer vision and graphics authors use as one of the light scattering model's parameters [24, 34, 63, 108]. The subsection below will outline the design of early models before proceeding to discuss a more specific facial reflectance model.

2.2.1 The Bidirectional Reflectance Distribution Function

The purpose of the general reflectance model is to characterize the directional distribution of the reflectance of a certain material using physical models that are suitable for the design of efficient global illumination computation algorithms. Reflection is a process during which an electromagnetic power flux travels incidentally towards a point of a surface, and leaves that point without any change in frequency. The function that is used to model this phenomena is called the Bidirectional Reflectance Distribution Function (BDRF) [24, 63, 108]. The function defines the model that demonstrates how reflected radiance is distributed in terms of the distribution of incident radiance.

The light reflection depends on the characteristics of the light, and the composition of the material, and its physical traits. As a notation, the BRDF function can be written as:

$$BRDF_{\lambda}(\theta_i, \phi_i, \theta_o, \phi_o, u, v)$$

where λ is an indication that the BRDF depends on the wavelength, θ_i and ϕ_i represent the light incident in spherical coordinates, θ_o and ϕ_o represent light reflected in spherical coordinates, and u and v represent the points of the surface. The positional variance for

this BRDF is introduced through the use of a detail texture. To reasonably approximate a spatially variant BRDF, the texture is added or modulated to the result of a BRDF lookup. Although a BRDF is a function of position, it is common to find a BRDF written as a function of just the incoming and outgoing direction and wavelength. In these cases, the positional variance is excluded in the BRDF description, such as, for example, $BRDF_\lambda(\theta_i, \phi_i, \theta_o, \phi_o)$. This BRDF is known as a position-invariant BRDF. Given that the spatial position is not included as a parameter of this type of BRDF, the function must assume that the reflectance properties of a material do not vary with spatial position, meaning that this type of BRDF is limited to homogenous materials [108]. From hereon, when describing a BRDF function, the λ subscript is omitted for the sake of notation simplicity. It is to be noted that the values produced by a BRDF do depend on the wavelength or color channel under consideration. In practice, in terms of the RGB color convention, each color channel has its own BRDF value, so each color channel must be determined separately (i.e. R, G, and B separately).

Before defining the BRDF, it is necessary to define a differential solid angle. As mentioned before, BRDFs measure how light reflects off a surface when viewed under various viewing positions. This can be described generally in terms of the quantity of light arriving at or passing through a certain area. Light is measured in terms of flow through a specific area and can be defined in terms of the amount of energy per-unit surface area (i.e. Watts/meter^2). Hence, to determine the amount of light that arrives at or leaves a surface, we need to calculate the amount of light passing through a small cross-sectional area surrounding a direction. Essentially, a solid angle can be described as being the area of the specific patch on the surface of the sphere (see Figure 2.3).

Figure 2.3 shows a unit sphere and a unit vector positioned at the origin. The pyramid region highlighted on the inside of the sphere represents a volume of directions. The portion of the unit sphere bound by the intersection of the pyramid and the unit sphere form the boundary of the small patch on the sphere's surface; the area of this small patch is the differential solid angle [108]. Describing the vectors in terms of the spherical coordinates (θ, ϕ), their small differential angular changes as $d\theta$ and $d\phi$, the differential solid angle $d\omega$ can thus be defined as:

$$d\omega = (height)(width) = (d\theta)(\sin\theta\, d\phi) = \sin\theta\, d\theta\, d\phi$$

Where both the width and the height of the rectangular patch on the sphere are measured in radians, and the area quantity is measured in units of radians squared or steradians, sr.

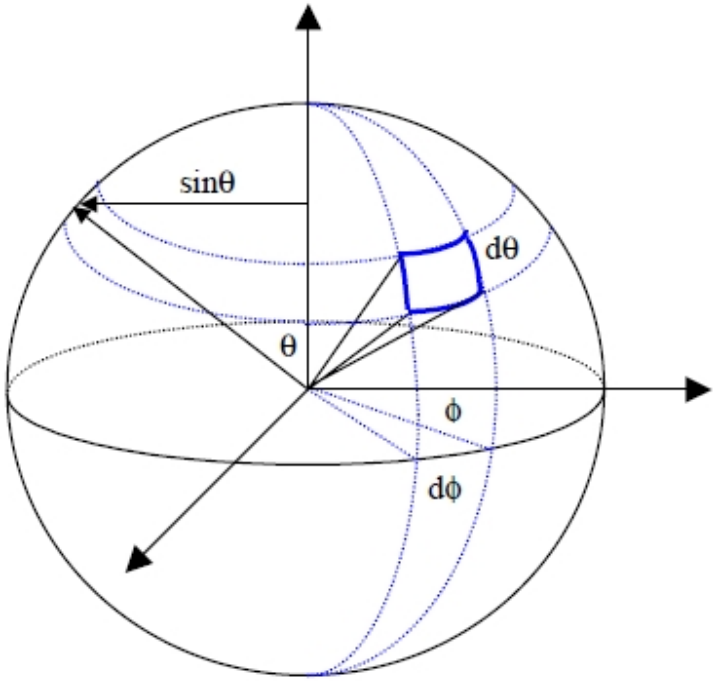

Figure 2.3: The differential solid angle on a sphere. Taken from [108]

After understanding the notion of a differential solid angle, the definition of a BRDF can now be given. The BRDF is the ratio of the quantities of the reflected light from the outgoing direction w_o, to the amount of incident light that reaches the point at the surface from the incoming direction w_i [88, 108] (see Figure 2.4). The quantity of incoming and outgoing light can be written as E_i and L_o respectively.

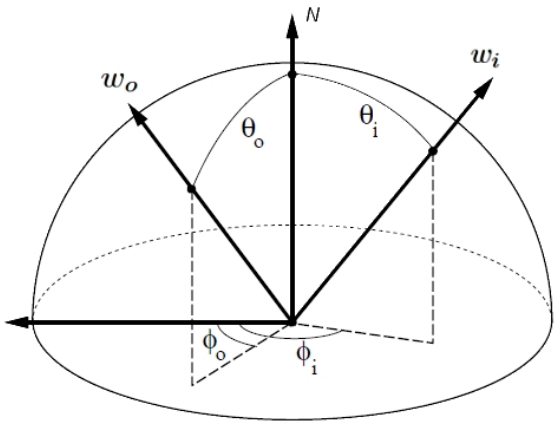

Figure 2.4: BRDF as a function of (θ_i, ϕ_i) and (θ_o, ϕ_o). Figure adapted by the author from [88]

The differential solid angle is the area of a small rectangular region on a unit sphere (the 'blue square patch' in Figure 2.4). The amount of light arriving from direction of the light source is proportional to the amount of light arriving at the differential solid angle. Suppose the light source has intensity L_i, and since the differential solid angle is small, the region is uniformly illuminated as the same quantity of light, L_i, arrives for each position on the differential solid angle. This allows the total amount of incoming light arriving through the region to be $L_i\, dw_i$ to be calculated. To determine the amount of light with respect to the surface element, the incoming light must be "spread out" or projected onto the surface element. This projection is accomplished by modulating that amount by $\cos\theta_i = N \cdot w_i$, where N is the normal of the surface. Meanwhile, the outgoing light can be determined by $E_i = L_i \cos\theta_i\, dw_i$. The BRDF can then be defined as:

$$BRDF(\theta_i, \phi_i, \theta_o, \phi_o) = \frac{L_o(\theta_o, \phi_o)}{L_i(\theta_i, \phi_i)\cos\theta_i\, dw_i}$$

Where L_o is the quantity of reflected light from point surface in direction w_o with units of $\mathrm{W/sr^{-1}m^{-2}}$ and E_i is the amount of arriving light to point surface from direction w_i with units of $\mathrm{W/m^2}$. Since the BRDF definition includes a division by the solid angle, this results in the BRDF having units of inverse steradians, $\mathrm{sr^{-1}}$.

2.2.2 Past Reflectance and Scattering Models

In modeling natural reflectance, there are many properties that need to be considered, such as retro-reflection, occluding, isotropic or anisotropic surface, and conservation of energy. Additionally, they must contemplate the reflectance characteristics they want to model, namely the specular and the diffuse. It is difficult to design a model that covers all of the properties that affect the behavior of light. So, most authors design their model to focus on a specific goal instead, each with their own formulation, conditional setup, and applicability [63, 74, 79, 95, 101, 106].

Torrance and Sparrow model is one of the earlier models that introduced physical reflection for isotropic materials [63]. The model has become a precursor for others that account for polarized light and rough surfaces in their model design. Torrance and Sparrow defined the surface roughness as microscopic concavities, called 'microfacets', which they have assumed to be in V-form of equal length. The microfacets have random orientation and their distribution is controlled using specific parameter values that simulate varying degree of roughness.

In the case of modeling reflectance for a rough surface, Oren and Nayar [74] have developed a diffuse reflectance model based on Torrance and Sparrow roughness model that also uses the microfacets [95]. The Oren and Nayar model is considered to be an improved version of the classic Lambertian interpretation for diffuse materials [63]. The roughness of the surface is specified using a probability function for the facet slopes. The model assumes that each facet followed Lambert's law and that the facet area is larger than the incident light wavelength. The model can be derived using geometric optics because of the large facet area. The model also accounts for the complex geometric effects, such as masking, shadowing, and inter-reflection.

Meanwhile, as a complement to the rough surface models, Wolff et al. [106] developed the reflectance model for smooth surfaces, which accounts for subsurface refraction using Fresnel attenuation and Snell refraction. The Wolff model assumes that subsurface optical scattering and air-dielectric boundary conditions exist. Using the Fresnel coefficient, the model describes how incident light and subsurface scattered light distribution behave at the smooth air-dielectric surface boundary. This model, however, differs from Lambertian when the Fresnel reflection terms become significant.

Ragheb and Hancock [79] first attempted to create a light scattering model based on the Beckmann–Kirchhoff model for moderately rough surfaces by adding the Fresnel term to describe the subsurface scattering effects for surfaces of intermediate roughness. Their objective was to extend the Beckmann–Kirchhoff model to account for the subsurface refractive attenuation of light prior to wave scattering. Based on the Beckmann–Kirchhoff model, Ragheb and Hancock used two variant correlation functions, the Gaussian and the Exponential, to derive closed-form solutions for the process of light scattering from random rough surfaces. Ragheb and Hancock also demonstrated that the best proposed modified model occur when the model is incorporated with the Wolff et al. version of the Fresnel coefficient [106] and the Vernold–Harvey version of the geometrical factor [101]. Ragheb and Hancock continued to test their model in [80], where they showed that their modified model was able to give a good estimation of the surface roughness parameters for dielectric surfaces using the pixel brightness measurements obtained from a digital camera.

Afterward, Ragheb and Hancock further improved their model in [81] by extending their previous modified model from [79, 80] so that it would work on rough, laminar surfaces for dielectrics. The new version modeled light scattering using their previous

modified Beckmann–Kirchhoff model, but modified it so that the scattering geometry of the material is split into two layers, namely the surface layer and the subsurface layer. The new model can produce surface scattering and subsurface scattering separately with the later accounting for any additional refraction, which is known as the Fresnel layer transmission. Additionally, the new model has been shown to give excellent quality of model fitting results when tested using the BRDF data of human skin.

All of these models can be used to model reflectance (or scattering) for various types of material. In Subsection 2.2.3, I will consider several articles drawn from literature that are aimed specifically at modeling light scattering on human skin. Authors developing the skin reflectance model have also often worked on the acquisition method in parallel. The acquisition method will be further reviewed in Section 2.3.

2.2.3 Human Skin Light Scattering Models

In their efforts to create the appearance of soft skin, Hanrahan and Krueger [36] introduced the subsurface scattering model for the skin. Their model was motivated by the optical properties of the skin surface (epidermal and dermal layers). The reflection of the material outer surface was modeled using the Torrance and Sparrow's microfacet model and they designed their own subsurface scattering based on 1D linear transport theory. The model relates the physical properties of the layered material to its subsurface reflectance properties. The authors assumed the physical material to be a layered homogeneous scattering medium. However, the model ignores the light scattering aspect.

Koenderink and Pont [50] introduced the asperity scattering model that adds a 'surface lobe' to the usual skin reflectance (diffuse and specular). Aesthetically, the model gives the skin a more 'soft' and 'velvety' appearance. The model assumes that sparse scattering occurs where thin layer scatterers cover the surface, such as hair follicles and/or dust. The authors claim that it is an important effect as many materials are covered with scatterers. Meanwhile, Tsumura et al. [98] have managed to model different skin color and texture. Using their E-cosmetic function, they can change the strength of the skin pigmentation (melanin and hemoglobin) by using the extraction completed previously during independent component analysis. Even though the authors were able to synthesize the way facial images changed due to tanning or alcohol consumption, no analysis was made on how the aging affects the melanin and hemoglobin.

Krishnaswamy and Baranoski [53] presented a BIOSPEC model to describe the human

skin structure. The model comprised of components that emulate five skin layers, namely the stratum corneum, epidermis, dermis (papillary and reticular) and hypodermis. However, due to the high quantity of parameters and the complex interaction between them, it relies on the brute-force Monte Carlo estimation.

Weyrich et al. [104] developed a skin reflectance model wherein the parameters were estimated using multiple measurements that they captured using custom built devices. They measured three types of data, namely the 3D face geometry, light reflection, and subsurface scattering. They use the measurements to then estimate the parameters, which are the spatial-varying analytic reflectance model (Torrance-Sparrow or Blinn-Phong), a diffuse albedo map and the diffuse scattering coefficients. The paper also reported a face reflectance analysis. They claimed that from their analysis that the absorption and scattering parameters have no correlation with age. However, they may not have found any correlation between the parameters and age as a result of the inclusion of too few senior subjects in the experiment (total subjects are 149).

Donner and Jensen [14] presented the first biophysically motivated Bidirectional Surface-Scattering Distribution Function (BSSRDF). They modeled human skin as a double layered component with biophysical-based user parameters and intuitive behavior, such as the melanin and the hemoglobin fraction. Other parameters for the model, however, were fixed, based on the authors' reasoning that they have a low impact on the overall skin appearance.

In a follow up study, Donner et al. [15] improved the model by introducing the layered, heterogeneous light scattering model for the skin. The model was designed to capture spatial variation without applying albedo textures to the skin's outer surface. They used intuitive parameter maps over the surface of the individual scattering layers with thin absorbing layers between them. Even though the model is appearance-centric in its data acquisition, it was reported that the model was able to reproduce the complex variations in skin pigmentation. Nevertheless, the authors did not make any analysis on the aging effects on the skin.

Meanwhile, Iglesias–Guitian et al. [38] introduced a model that simulates the changes in the appearance of human skin due to aging. The model is a time-varying, multi-layered, biophysical-based model that relies on biophysical parameters from medical and optical tissue literature. The model is aimed more at synthesizing the appearance of aging skin, rather than parameter analysis. Nevertheless, the authors did undertake significant

analytic review of the available medical and optical tissue literature regarding the impact of aging on the skin. They determined that the aging process is similar for all skin types, regardless of gender, and that the skin tends to appear paler and less glossy as the age of the subject increases.

In one report, Igarashi, Nishino and Nayar [39] surveyed the appearance of human skin based on studies from four different fields: 1) computer vision, 2) computer graphics, 3) Medicine and 4) Cosmetology - and presented them as a single unified framework. The authors have made an outline of the physioanatomical characteristics of skin that are important and later relate it to the studies conducted to each of the structural components of the skin.

2.3 Acquisition Methods

Generally, the face reflectance/appearance data acquisition can be categorized into two approaches: 1) the Image-based approach and 2) the Parametric approach [49]. The first uses the captured data directly for rendering and is not bound to a specific model. It also able to reproduce all real-world effects. Meanwhile, the second uses the measurement data to determine the parameters of some parametric forward appearance model used during rendering [49]. It is able to use fewer measurements in circumstances where the parametric models have been appropriately chosen.

One of the earlier works that considered acquiring the face reflectance/appearance was undertaken by Debevec et al. [13]. This followed the Image-based approach. They developed a method of acquiring the reflectance field of the human face by densely sampling the incident illumination directions from two fixed viewpoints, and then separating the face specular-diffuse reflectance components using linear combination computation. The Debevec et al. method can produce high-quality visual synthesis, but it is very data intensive.

Weyrich et al. [104] proposed a parametric acquisition method for measuring per-pixel specular BRDF, diffuse albedo map, and diffuse subsurface scattering. The device they use to acquire the specular BRDF and diffuse albedo measurements is a geodesic dome with 150 Light Emitting Diodes (LED) and 16 cameras. In order to measure the translucency (subsurface scattering), they used a custom built contact probe consisting of a linear array of optical fiber detectors. The acquisition method, however, requires extensive sampling and a relatively long capture time.

Ma et al. [64] developed a technique that mimicked the spatial-varying illumination acquisition method proposed by Debevec et al. [13] but incorporated a parametric approach with a lower set of lighting conditions. The authors used four spherical gradient illumination patterns, as this lighting condition is capable of acquiring independent estimation of specular and diffuse reflectance surface normal across the entire object surface.

As this thesis is required to analyze the parameter estimation of the model, a parametric acquisition method is needed. The capturing device will closely resemble the design of Ma et al. [64] with a small modification in the capturing sequence process.

2.4 Summary

In this chapter, literature from multiple fields related to facial aging, light reflecting/scattering models, and acquisition methods have been reviewed. Literature in the medical, human perception and skin optical fields have shown that the skin characteristics change as the age increases. However, none of the current papers on reflectance/scattering models have thoroughly analyzed how aging really affects the reflectance/scattering model predictions or its parameter estimation. So, an investigation on the topic is needed.

2.5 Research plan, methodology and thesis structure

Facial aging research in computer vision and pattern recognition mostly use the aging features for their aging estimator system. However, the study never goes further to investigate what effects that cause the aging features to appear in the first place. It would be interesting if we can study the inner working of the skin in term of a model-based that can obtain multiple parameter values that have meaning (e.g. the surface roughness and light absorption) and study its relation to the process of aging. Not only we can use the parameter values as input for age estimation system, we can relate it to the medical condition of the skin. For example, a young healthy person has a bright skin, while an older person has a dull skin. The surface roughness between the two would be different, but how about their skin light absorption? Is it also different? Which one plays a major role in affecting the light scattering behavior between the two; the surface roughness or the light absorption?

This paper will investigate whether the light scattering model parameters change together with the aging skin, and if so, whether the changes occur in a positive or negative

manner. This will help determine whether the parameters of a model can be used as a tool for estimating age. An analytic-base light scattering model seems to be the best choice for this experiment. By choosing this type of model, the parameters can be estimated by using the inverse rendering technique, which is an easier method than attempting to directly measure it using *in–vitro* type measurements.

Before conducting the aging experiment, the choice of light scattering model and the experimental setup need to be addressed. The light scattering model must be able to model the outer and the inner layer of the material (e.g. skin). In Chapter 3, a new light scattering model is introduced. It is a modified version of the Ragheb–Hancock (R-H) model [81] with added light absorption function. The R-H model was chosen due to its simple dual layer representation (surface and subsurface layer). They are other better model to be based upon for this experiment such as the BIOSPEC model [53] or the Donner's model [15]. However, the author chooses the R-H model due to that the model is much simpler to modify by the author. The new model's functionality and accuracy will be tested using database samples that are either isotropic [12] or anisotropic [18] in nature. This is to observe and compare it with another model for its rendering capability. To observe how good the new model is when it is used as a standard light scattering model and to investigate its limitation when test on the different type of samples.

In order to investigate the model parameter relationship with aging, appropriate parameters from the model need to be selected first. The selected parameters need to have a rational relationship with the skin properties, such as the surface skin roughness or the refractive index [20, 22, 38, 39, 47, 51, 62, 91, 112]. However, due to equipment and resource limitation at the time, the real measurements such as the surface roughness cannot be done (need roughness measuring instrument). Hence, an alternative method is used, by comparing the light scattering with that of the material's polarization state. It was known that polarization is directly related to how a material scatters light. The material properties such as surface roughness, subsurface roughness, and light absorption can directly affect how polarization will behave. To validate the model parameter relation with the material's known measurement, the author decided to use the degree of polarization (DOP) as the material's measurement. The relationship between the two is analyzed by doing a correlation test. Furthermore, the test will be conducted using materials with varying degree of properties (e.g. very rough surface; highly chromatic). This is to observe whether the model can estimate the parameters as closely as the material physical

properties (logically) and for varying type of materials. The parameter selection for the later parameter-age test (Chapter 5) is based on a comparison between the new model parameters with the sample degree of polarization (DOP).

Meanwhile, angle measurements are needed for the model prediction, so the samples surface normal map and image light scattering will be captured using the spherical gradient illumination photometry technique proposed by Ma et al. [64]. The reason for this choice is that the technique is more accurate and faster than the 3D scanner. However, aligning the image sequence captured in disparate illumination environment would not work normally if we used the standard alignment method. So, a new alignment technique for handling this particular problem is also presented in this thesis. Accuracy tests for the new alignment technique will also be conducted and detailed in Chapter 4.

Finally, Chapter 5 will consider the correlation test between the subject age and the chosen parameters. Results will be analyzed based on specific categories such as gender, skin type, and facial section. The discussion will highlight any significant findings, interesting behavior, limitations, and any unforeseen circumstances. The conclusion, which will summarize the findings and evaluate any experiments shortcoming for future improvement, will also be detailed in Chapter 6.

Chapter 3

Absorptive Scattering Model for Rough Laminar Surface

Here, a new analytic–based light scattering model is introduced. The new model is an extension of the Ragheb–Hancock (R–H) model [81], in which it was previously designed to model rough laminar surface boundaries for dielectric materials. The new model modified the R–H model by adding a light absorption function, defined in the subsurface layer part of the model. To investigate the aging effect on the skin light scattering, this model is created for studying how the model parameters behave when tested on different aging subjects and whether they are suitable to be used as a tool for estimating/classifying age. Nevertheless, the new model is foremost a light scattering model, it is essential to investigate how the new model's rendering and fitting accuracy fare with other models; especially with R–H model. Hence, the fitting tests were done on two different databases: 1) the CUReT database (isotropic samples), and 2) the UTIA database (anisotropic samples). The reason for using different range of samples on the model is to observe how good the new model is and what its limit when it is used as a standard light scattering model. Further explanation of the new model and its accuracy test results will be mentioned in this chapter.

Firstly, the (R–H) model [81] will be reviewed in Section 3.1, where the section described how Ragheb and Hancock modeled the diffuse light scattering for the surface and subsurface layers of a material. Afterward, Section 3.2 introduced the new model and also highlights some of its behavior. Section 3.3 then provides an experimental evaluation of the new model done on two reflectance measurement databases, captured either in isotropic condition (CUReT database [12]) or anisotropic condition (UTIA database [18]).

3.1 R–H model for layered rough surfaces

In [81], Ragheb and Hancock (R–H) have presented a detailed diffuse light scattering model using the wave scattering theory. The model assumes that the diffuse radiance is scattered from bi-layered rough surfaces, consisting of an opaque sub-surface layer below a transparent one. The top or surface layer was modeled by a single surface scattering component, while the bottom or subsurface layer was modeled using the combination of both the effects of radiance transmission through the surface layer and a single subsurface scattering component. Here, the authors used Vernold and Harvey version of the Beckmann model for both the surface and subsurface rough scattering effects, while, the Fresnel theory and the Snell's law are used for modeling the attenuation factor and the light transmission [81].

The surface scattering geometry of the R–H model [81] was based on Kirchoff theory, as shown in Figure 3.1 (Left). The vector S points in the direction of the light source, which means that incident light with radiance L_i propagates in the $-S$ direction. The scattered radiance L_o is in the direction V, which is the position of the viewer. The light beam is incident on the surface with zenith angle θ_i and azimuth angle ϕ_i. Additionally, Beckmann's geometry applies so $\phi_i = \pi$ [81]. The light beam is then scattered at zenith angle θ_s and azimuth angle ϕ_s.

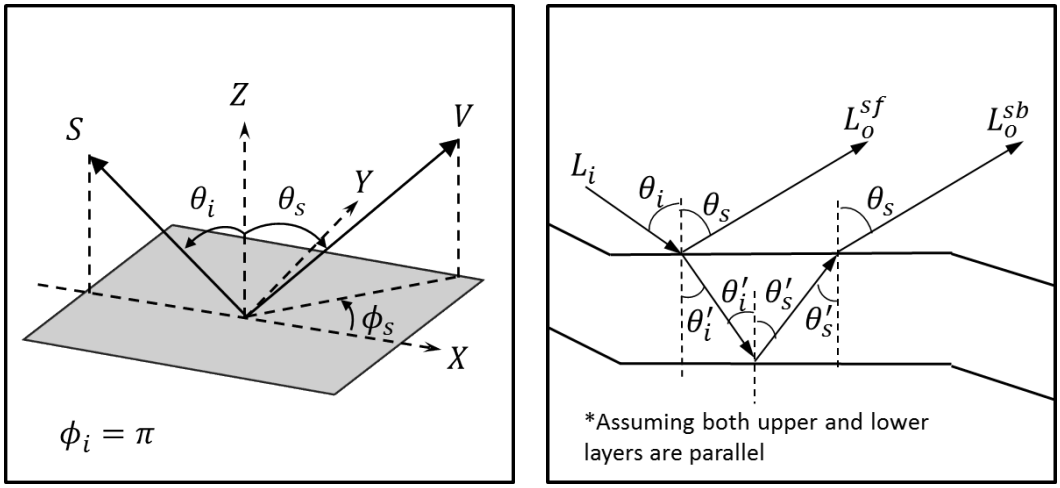

Figure 3.1: Tangent plane coordinate system (Left) and Layered rough surface under study (Right).

Ragheb and Hancock defined the subsurface layer part of the R–H model using the Snell's law and the Fresnel theory to account for the refractive distortion and the atten-

uation factor respectively [81]. Figure 3.1 (Right) shows the process for the subsurface scattering. It first starts with: 1) the light enters the surface at angle θ_i, 2) next, it refracted to angle θ_i', 3) then undergoes single scattering on the lower surface layer (lower boundary), at angle θ_s', and 4) finally exits the surface layer (upper boundary) with zenith and azimuth angles θ_s and ϕ_s. Both of the outgoing radiance components (surface and subsurface) are considered identical by the authors. The total outgoing radiance is the linear combination of both components with β as its relative balance control. The R–H model is given as:

$$L_o = \beta L_o^{sb} + (1-\beta) L_o^{sf} \tag{3.1}$$

where the surface scattered radiance is $L_o^{sf} = L_o^{sf}(\theta_i, \theta_s, \phi_s, \sigma/T)$ and the subsurface scattered radiance is $L_o^{sb} = L_o^{sb}(\theta_i, \theta_s, \phi_s, \sigma'/T', n)$. The parameter β control which two components (surface or subsurface) scatter the light the most. If β is higher, then the light mostly scatter from the subsurface layer, making the surface layer more transparent (example material –dielectric). If it is lower, then the light mostly scatter from the surface layer, making the surface layer less transparent, meaning less light penetrates the surface layer (example material –metal). In physical term, Equation 3.1 basically describes how the light incident is scattered either by the surface or through subsurface interactions. The notations used are summarized in Table 3.1.

Following the Beckmann model, the R–H model used two parameters to account the material roughness property; a) the root-mean-square (RMS) height deviation σ of the surface relief distribution about the mean surface level and b) the correlation length T, which defined in terms of surface correlation function that characterizes the relative spacing of peaks and valleys in the surface profile. R–H in [81] also presented two different model variants, which are i) the Gaussian and ii) the Exponential, in which both refers to the nature of the correlation function for the surface and subsurface roughness. From [81], the scattered surface radiance when the correlation function is Gaussian is given by:

$$L_G^{sf}(\theta_i, \theta_s, \phi_s, \sigma/T) = K_G \left[\frac{\cos(\theta_i)}{v_z^2(\theta_i, \theta_s)}\right] \times \exp\left[\frac{-T^2 v_{xy}^2(\theta_i, \theta_s, \phi_s)}{4\sigma^2 v_z^2(\theta_i, \theta_s)}\right] \tag{3.2}$$

and when surface correlation function is Exponential:

$$L_E^{sf}(\theta_i, \theta_s, \phi_s, \sigma/T) = K_E \left[\frac{\cos(\theta_i)}{v_z^2(\theta_i, \theta_s)}\right] \times \left(1 + \left[\frac{T^2 v_{xy}^2(\theta_i, \theta_s, \phi_s)}{\sigma^2 v_z^2(\theta_i, \theta_s)}\right]\right)^{-\frac{3}{2}} \tag{3.3}$$

where $v_{xy}^2(\theta_i, \theta_s, \phi_s) = [k(\sin(\theta_i) - \sin(\theta_s)\cos(\phi_s))]^2 + [-k(\sin(\theta_s)\sin(\phi_s))]^2$; $v_z(\theta_i, \theta_s) = -k(\cos(\theta_i) - \cos(\theta_s))$; and $k = 2\pi/\lambda$. The coefficients K_G and K_E are both proportional

Table 3.1: The formula notation.

Notation	**Description**
L_i	Incident radiance
L_o	Total scattered radiance
L_G^{sf}	Surface scattered radiance with Gaussian correlation function
L_G^{sb}	Subsurface scattered radiance with Gaussian correlation function
L_E^{sf}	Surface scatter radiance with Exponential correlation function
L_E^{sb}	Subsurface scattered radiance with Exponential correlation function
θ_i	Surface incident zenith angle
θ_s	Surface scattering zenith angle
θ_i'	Subsurface incident zenith angle
θ_s'	Subsurface scattering zenith angle
ϕ_s	Scattered azimuth angle
σ/T	Surface Root-Mean-Square (RMS) slope
σ'/T'	Subsurface Root-Mean-Square (RMS) slope
K_G or K_E	Coefficients for the surface equations of Gaussian and Exponential respectively
$d\omega'$	Solid angle under mean surface level
n	Standard refractive index
β	Balance parameter

to $(\sigma/T)^2$ and can be normalized. Meanwhile, the subsurface scattered radiance when the correlation function is Gaussian is given by:

$$L_G^{sb}(\theta_i, \theta_s, \phi_s, \sigma'/T', n) = L_G^{sf}(\theta_i', \theta_s', \phi_s, \sigma'/T') \times [1 - f(\theta_i, n)][1 - f(\theta_s', 1/n)]d\omega' \quad (3.4)$$

and when the subsurface correlation function is Exponential:

$$L_E^{sb}(\theta_i, \theta_s, \phi_s, \sigma'/T', n) = L_E^{sf}(\theta_i', \theta_s', \phi_s, \sigma'/T') \times [1 - f(\theta_i, n)][1 - f(\theta_s', 1/n)]d\omega' \quad (3.5)$$

where, the subsurface solid angle is:

$$d\omega' = \frac{\cos(\theta_i)}{n^2 \cos(\theta_i')} d\omega \tag{3.6}$$

Meanwhile, the Fresnel coefficient, which models the refraction effects of the layers, is given:

$$f(\alpha_i, r) = \left[\frac{\sin^2(\alpha_i - \alpha_t)}{2\sin^2(\alpha_i + \alpha_t)}\right] \times \left[1 + \frac{\cos^2(\alpha_i + \alpha_t)}{\cos^2(\alpha_i - \alpha_t)}\right] \tag{3.7}$$

$$r = \frac{\sin(\alpha_i)}{\sin(\alpha_t)} \quad and \quad \alpha_t = \sin^{-1}\left[\frac{\sin(\alpha_i)}{r}]\right] \tag{3.8}$$

In Equation 3.8, where light is transmitted from air to dielectric, then $r = n$ and $\alpha_i = \theta_i$. If, on the other hand, light is transmitted from dielectric to air, then $r = 1/n$ and $\alpha_i = \sin^{-1}[\sin(\theta_s)/n]$.

Single layer scattering model designs are simpler and do not need to account the light transmission or the light absorption aspects. However, in nature, many surfaces have the laminar structure that composed of translucent layer and opaque layer with a certain degree of roughness. Moreover, varying substance in the layer can affect how light transmits and/or absorb. For such surface, it is best to use a light scattering model that accounts the two layers (upper and lower) and the light behavior inside the layer (transmission and absorption). Examples of these surfaces would be the human skin and plants. A non-layer model can be considered simpler than a model that account the material's laminar structure. However, its simplicity cost it the ability to analyze the inner layer property of a material.

3.2 The new model with light absorption

One of the main reason R–H model was based upon, is because of the model simple dual-layer design (Figure 3.2 .Right) can resemble a general skin layer (see Figure 3.2 for the simple depiction of the young skin layer and the old skin layer). The top layer of the model resembles the surface of the skin, while the bottom layer of the model resembles the skin inner layer between the skin surface and the collagen (Figure 3.2). The only limitation that R–H model is that it does not model the light absorption, in which, is one of the properties of skin that can affect the light scattering. This does not limit to skin only, other dielectric materials also have a varying degree of light absorption. The new model

should put that into consideration as to make a model that not just focus on skin, but also other materials as well.

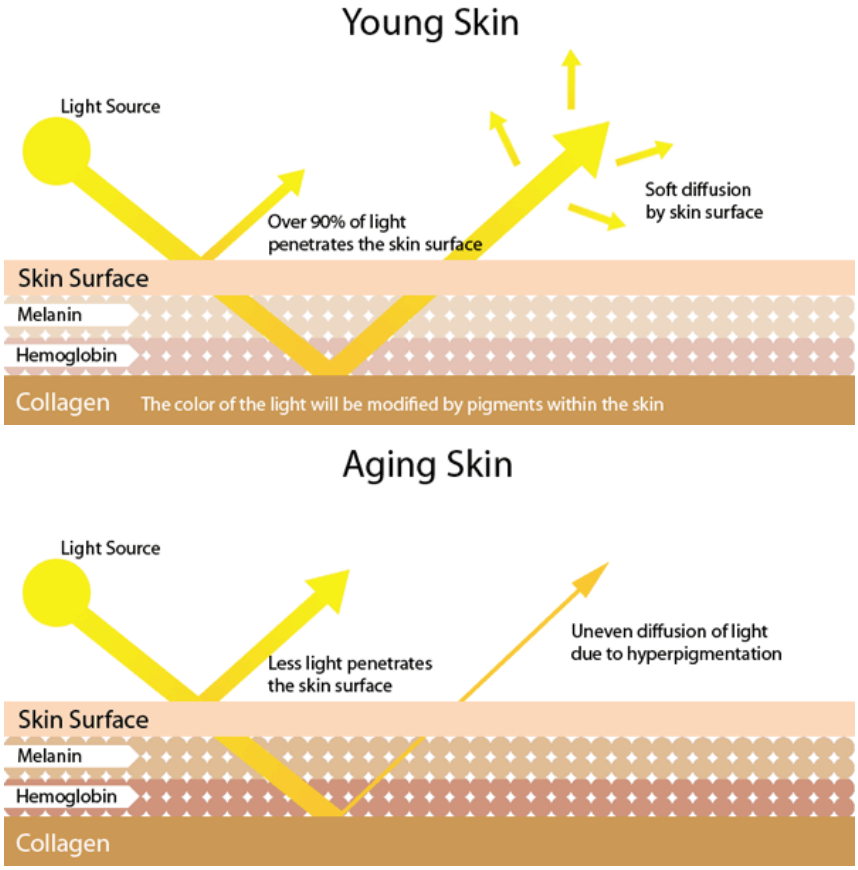

Figure 3.2: Diagram of light scattering on the skin. (Diagram was taken from [73].

The new model in this thesis is a modified version of the R–H model [81]. The R–H model is detailed but it does not account for light absorption. The new model extent the R–H model by adding an absorption term; defining it using the conservation of energy for light transmission, reflectance, and absorption. Moreover, the absorption parameter is unit-less and can be used as an alternative representation for light absorption in a dielectric.

3.2.1 Defining the light absorption in the subsurface layer

There are different light absorption representations/parameters that can be used to define a reflectance/scattering model. One example is the complex refractive index, which was used in Mie Theory to describe the absorption of electromagnetic radiation by spherical particles [6]. However, defining a light reflectance/scattering model using the complex refractive index can be difficult to manage due to the problem of trying to solve its imaginary

component.

Instead of using a predefined function as the absorption term (e.g. complex refractive index), the new model derives the light absorption using the principle of conservation of energy during light transfer and a newly defined absorption function. In Ragheb and Hancock's model [81], the reflectance is governed by the Fresnel coefficient and the conservation of energy was assumed to be satisfied provided the normalization $1 = Rf + Tr$ held. However, for the new model, the conservation energy is expressed via a different normalization:

$$1 = Rf + Tr + Ab \tag{3.9}$$

Where Rf is reflectance, Tr is transmission and Ab is absorption. Using the equation above and applying it to the subsurface scattering equations (Equation 3.4 and 3.5) would then extended R–H model to include the light absorption property. The geometry of the new layered rough surface under study would then look like Figure 3.3.

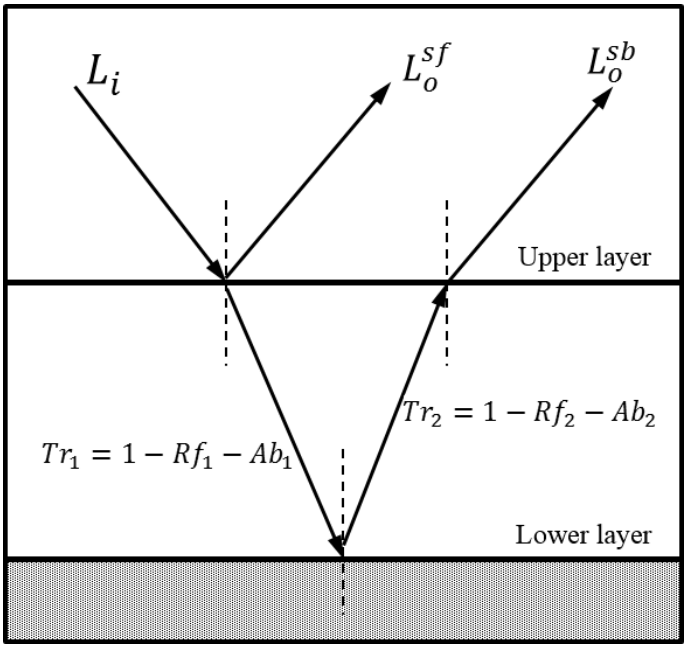

Figure 3.3: Light transfer and absorption in the layered surface under study.

Before modifying Equation 3.4 and 3.5, the absorption term Ab need to be derived first. Following the conservation energy in Equation 3.9, the light attenuation in the material must now govern by both the transmittance and the absorbance. To formulate and define how the attenuation is handled between transmission and absorption, we need to explore how the polarized light actually behave inside a material (e.g. dielectric). This can be

considered as its own study in its self. However, the study is beyond the scope of this thesis. Instead, I considered a much simpler approach in defining how the absorption would behave in a dielectric, semi-translucent surface.

Aiming to create a new absorption definition that is unit-less and simple, the function follows two assumptions. The first assumption is that the light absorption is assumed to be affected by the angle of penetration at the point of the incident on the surface of the material. The logic behind it follows that light transmission and absorption would have an inverse relationship when penetrating a surface dielectric at a specific angle of incidence. As an example, imagine a light penetrating a water surface, as the angle of incidence increases and reaching perpendicular angle to the water surface, the attenuation from the transmission would decrease, while the attenuation from the absorption increases. To represent the mentioned absorption behavior, cosine with even number power would be the suitable choice; replicating how light fully penetrate the surface at angle perpendicular to the surface of the material and zero penetration when the angle is parallel to the surface. Different cosine power were tested to observe which would be the best selection; they are $\cos\theta$, $\cos^2\theta$, $\cos^3\theta$, $\cos^4\theta$, and $\cos^6\theta$ (see Figure 3.4). The absorption should not be of negative value, therefore, the power must be an even number. Meanwhile, when using $\cos^4$ or $\cos^6$, the absorption term becomes zero when $\geq 75^o$. Compare to $\cos^4$ and $\cos^6$, $\cos^2$ still have a small amount of absorption when $\geq 75^o$ before becoming zero at 90^o. Moreover, $\cos^2$ has the average flexibility that it gives to the radiance curve. Hence, cosine squared is selected. This makes the new model a non-physical model.

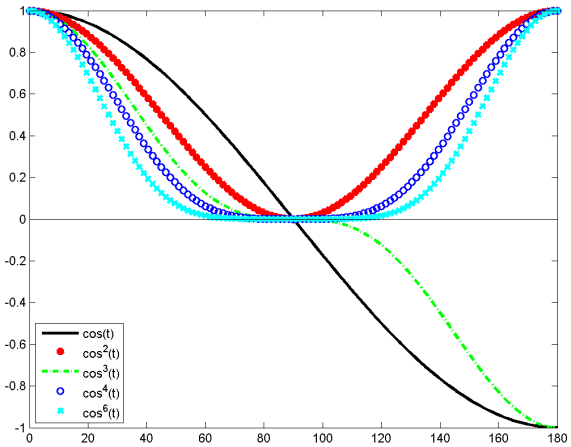

Figure 3.4: Different cosine power for defining the absorption term.

The second assumption is that absorption in the subsurface layer is instantaneous, meaning that the function ignores how much distance the light will travel inside the material. Absorption is instead quantified by using the parameter absorption percentage 'a', which represents the strength of the light absorption in the overall subsurface layer. Combining both assumptions, the amount of absorbed light Ab would be proportional to the cosine squared of the incident angle θ_i. As a result, the absorption is greatest when the incident light is normal to the surface and smallest when the incident light is perpendicular to the surface normal. The absorption term is defined as:

$$Ab_1 = Ab(a, \theta_i) = a(\cos^2(\theta_i))[1 - f(\theta_i, n)] \tag{3.10}$$

$$Ab_2 = Ab(a, \theta_{s2}) = a(\cos^2(\theta_{s2}))[1 - f(\theta'_s, 1/n)] \tag{3.11}$$

Where a is the fractional absorption parameter, used to control how strongly light is absorbed. Equation 3.10 is used when the incident light transmits from the air to the material. On the other hand, Equation 3.11 is used when the incident light transmits from the material to the air (see Figure 3.3). Since these two equations are related to transmission, their units are similar to irradiance, which is the watt per square meter ($\mathrm{W/m^2}$). Inserting Equation 3.10 and 3.11 into 3.4 and 3.5, the subsurface scattering component now becomes:

$$\begin{aligned} L_G^{sb}(\theta_i, \theta_s, \phi_s, \sigma'/T', n) &= L_G^{sf}(\theta'_i, \theta'_s, \phi_s, \sigma'/T') \\ &\times [1 - f(\theta_i, n) - Ab(a, \theta_i)][1 - f(\theta'_s, 1/n) - Ab(a, \theta_{s2})]d\omega' \end{aligned} \tag{3.12}$$

$$\begin{aligned} L_E^{sb}(\theta_i, \theta_s, \phi_s, \sigma'/T', n) &= L_E^{sf}(\theta'_i, \theta'_s, \phi_s, \sigma'/T') \\ &\times [1 - f(\theta_i, n) - Ab(a, \theta_i)][1 - f(\theta'_s, 1/n) - Ab(a, \theta_{s2})]d\omega' \end{aligned} \tag{3.13}$$

where

$$\theta_{s2} = \sin^{-1}\left[\frac{\sin(\theta'_s))}{1/n}\right] \tag{3.14}$$

By conservation of energy, a change in the absorption will cause a change in the transmission. Using the newly defined absorption function, Figure 3.5 shows how the different values of a affect the behavior of both the transmission and the absorption as the incident angle varies (for a medium with $n = 1.7$).

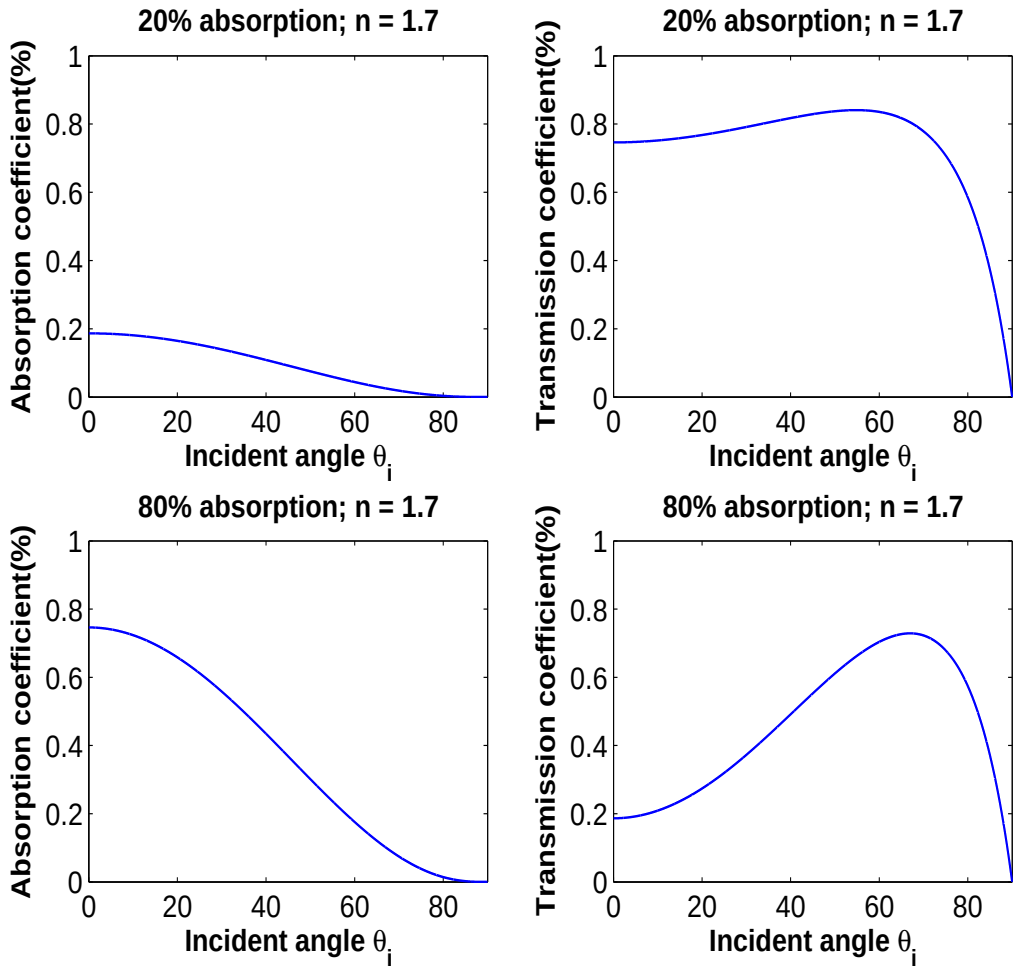

Figure 3.5: The Absorption and Transmission curve behavior.

3.2.2 The new model behavior

Light absorption is an electromagnetic radiation behavior that occurs in all creature and inorganic materials. Knowing the quantity of how much light is absorbed in a material can help give some idea about the molecules of components in a substrate. In skin optic or dermatology, this information can help detect some irregularities in the skin. For this study, the detection of the different level of absorption in the skin can be connected to the aging effect (e.g. skin dryness or skin disease due to aging [17, 51, 62, 72, 91, 96, 97]). If an analytical-based light scattering model can be used to accurately estimate the light absorption of the skin, then the process of extracting the cells in future studies can be ignored entirely. Hence, in this study, the new model is the author first step of making a method of obtaining the light absorption information of the inner skin in its original form

without the need of cell extracting tools.

The new model introduced here is an extension to the Ragheb and Hancock model with the inclusion of an absorption term. The new model allowing us to estimate the absorption percentage a, thus providing information concerning the light absorption characteristic of a material. When the value of the absorption percentage a is zero, the new model behaves similarly to that of R–H model. An in-depth behavior of the new model regarding its prediction for varying angular distribution when $a = 0$ can just be referred to the Ragheb and Hancock paper [81], which the authors have shown and explained in detail. This section, however, will focus on studying the different absorption values affect on the model prediction behavior.

As the Absorption percentage a increases, the subsurface scattering radiance at the incident angle near 0^o become more and more reduced. The decreasing subsurface scattering radiance in the curve behavior is the result from the absorption term subtracting the overall energy conservation, meaning that as both a and $cos^2(\theta_i) \approx 1$, the absorption value at these angles (when θ_i reaching 0^o) become much higher than the transmission value in the overall energy conservation, resulting in a reduced subsurface radiance.

In the overall scatter outgoing radiance, however, there is a peak that forms at these incident angles (near zero). The peak of the overall scatter outgoing radiance actually contributed by the surface scattering model. For the purpose of presentation, the prediction for the R–H and the new model scatter outgoing radiance curve plot for the Exponential and the Gaussian model variants are shown in Figure 3.6 for three different absorption percentage, a (e.g. $a = 0$, 0.25 or 0.40). In Figure 3.6, the left column is the Exponential variant with $\beta = 0.66$, $\sigma/T = 0.15$, $\sigma'/T' = 0.95$, and $n = 1.37$, while the right column is for the Gaussian variant with $\beta = 0.56$, $\sigma/T = 0.13$, $\sigma'/T' = 1.0$, and $n = 1.37$. The parameters values used for this plots were referred from [81], used for comparison and presentation purposes only. The top row of Figure 3.6 correspond to R–H model ($a = 0$), while the two bottom row correspond to new model ($a = 0.25$ for the middle row and $a = 0.4$ for the bottom row). The curves in each plot correspond to constant values of θ_i, while making $\phi_i = \pi$ and $\phi_s = 0$. Here a peak is form around $\theta_s = \theta_i$. While the peaks for the Exponent variant models are very close to the specular direction, this is not the case for the Gaussian variant models. Meanwhile, increasing the value 'a' causes the curves to decrease in their overall outgoing radiance, especially near the normal angle.

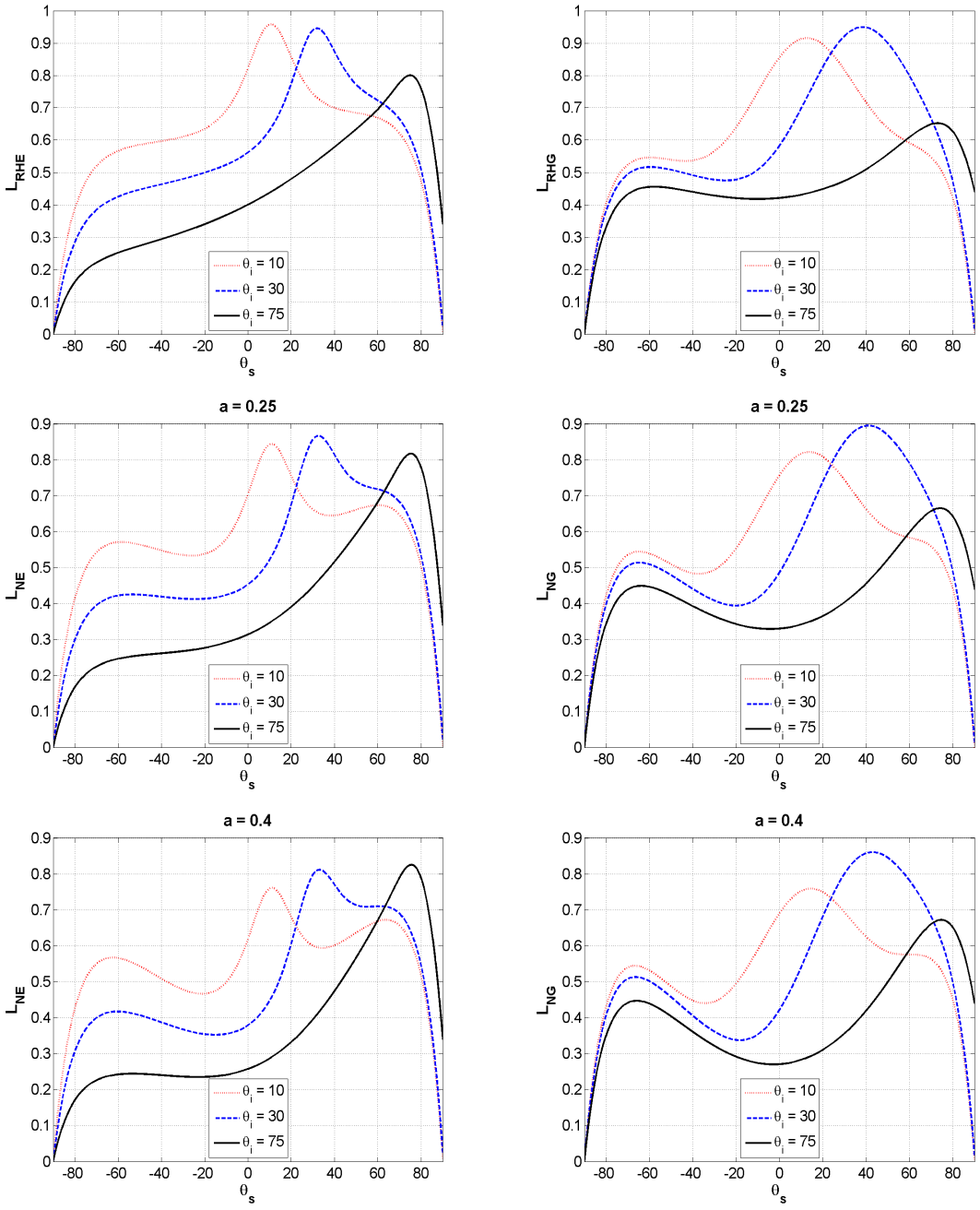

Figure 3.6: The scattered outgoing radiance prediction for the Ragheb–Hancock model (first row: $a = 0$) and the new model (second row: $a = 0.25$ and third row: $a = 0.40$), when the model variants against θ_s. The left column is for the Exponential with $\beta = 0.66$, $\sigma/T = 0.15$, $\sigma'/T' = 0.95$, and $n = 1.37$, while the right column is for the Gaussian where $\beta = 0.56$, $\sigma/T = 0.13$, $\sigma'/T' = 1.0$, and $n = 1.37$. Curves in each plot correspond to constant values θ_i. ($\phi_i = \pi$ and $\phi_s = 0$). The parameters values used for this plot were referred from [81]

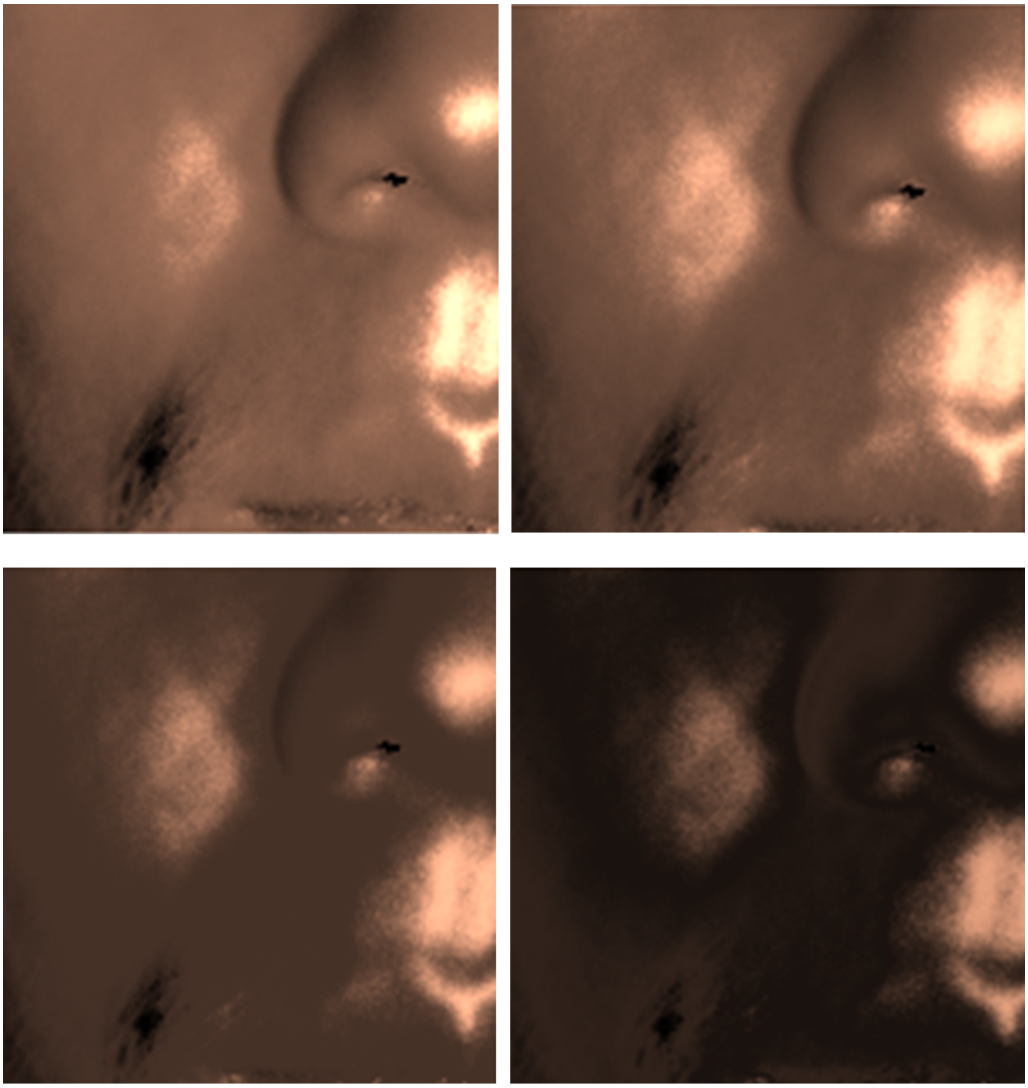

Figure 3.7: Rendering using the new model Gaussian with 0 (top left), 0.2 (top right), 0.5 (bottom left) and 0.9 (bottom right) absorptions ($\sigma/T = 0.15$; $\sigma'/T' = 1$; $\beta = 0.9$; $n = 1.37$).

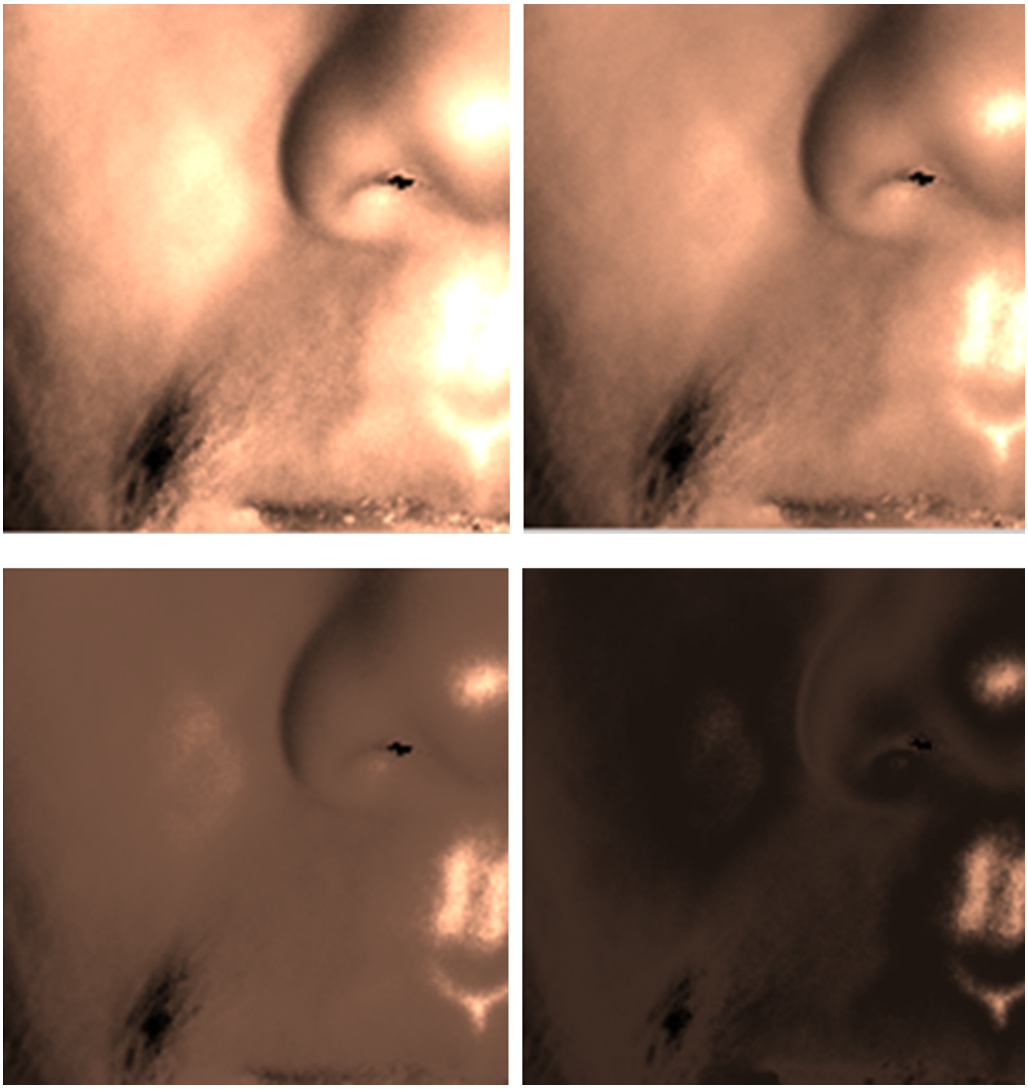

Figure 3.8: Rendering using the new model Exponential with 0 (top left), 0.2 (top right), 0.5 (bottom left) and 0.9 (bottom right) absorptions ($\sigma/T = 0.15$; $\sigma'/T' = 1$; $\beta = 0.9$; $n = 1.37$).

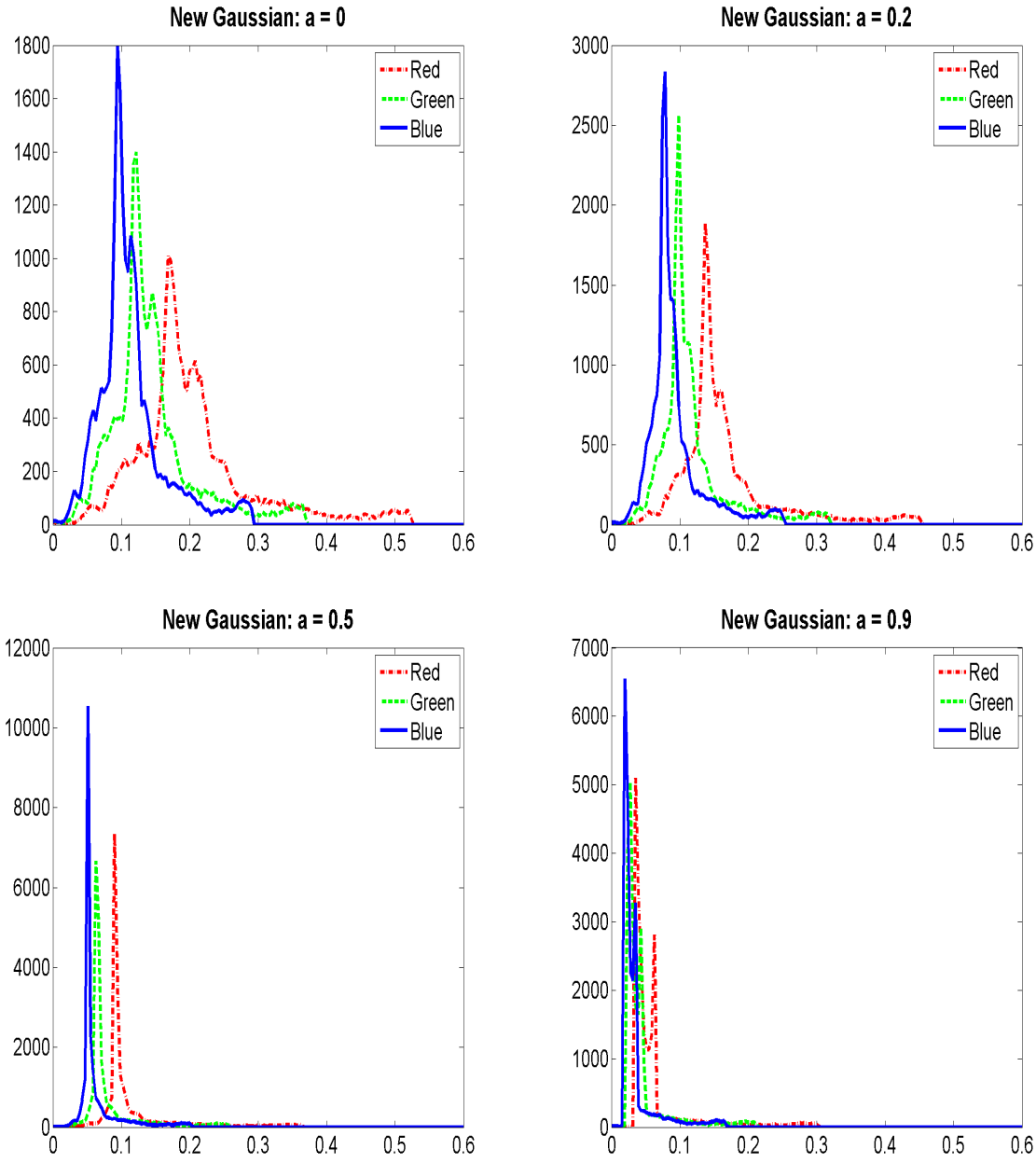

Figure 3.9: The histograms for the new model Gaussian rendering with 0 (top left), 0.2 (top right), 0.5 (bottom left) and 0.9 (bottom right) absorptions, a. ($\sigma/T = 0.15$; $\sigma'/T' = 1$; $\beta = 0.9$; $n = 1.37$). Here, the histograms show that as the absorption value increases, the intensities in the channels decreases (peak move to the left side of the histogram plot).

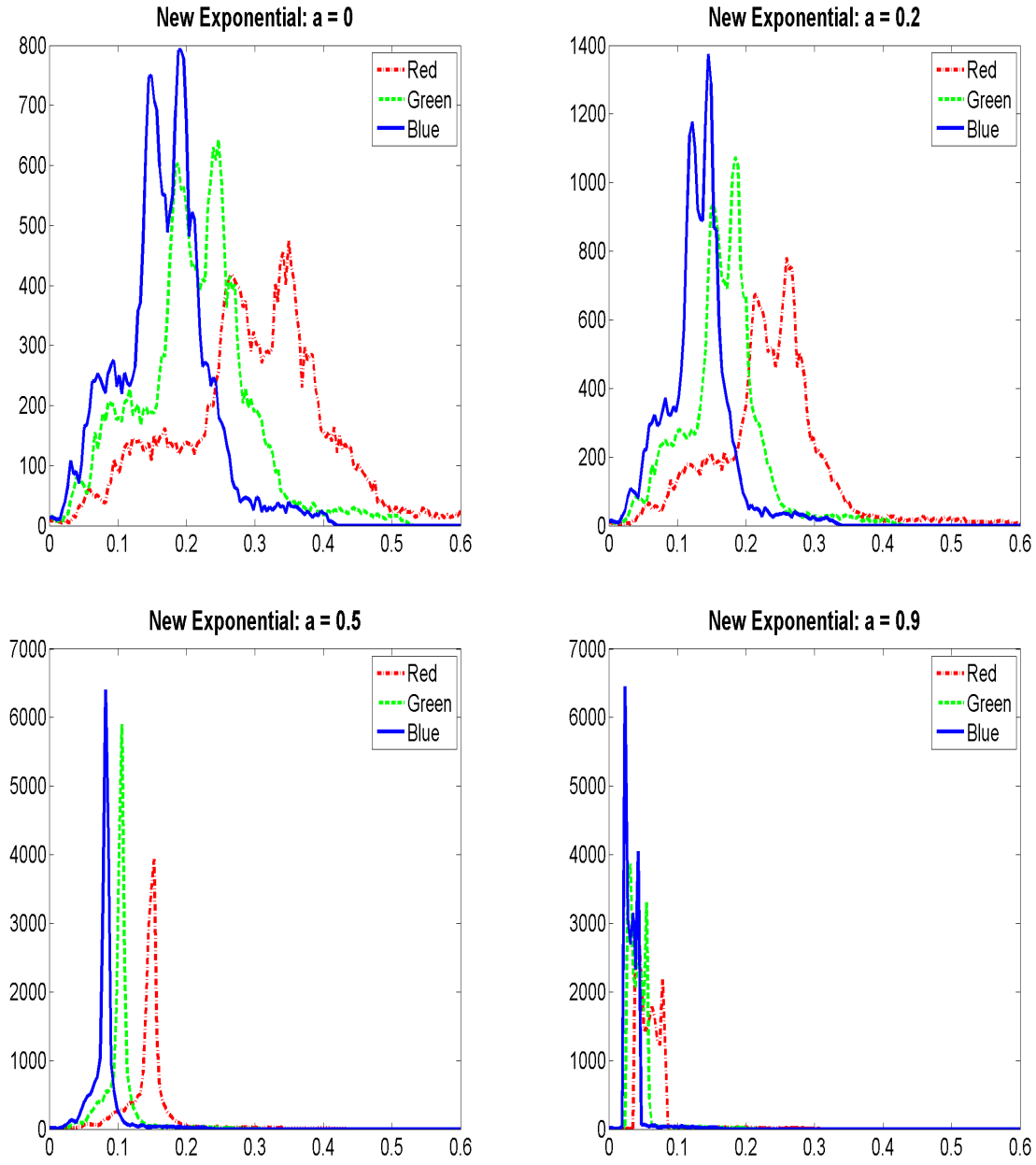

Figure 3.10: The histograms for the new model Exponential rendering with 0 (top left), 0.2 (top right), 0.5 (bottom left) and 0.9 (bottom right) absorptions, a. ($\sigma/T = 0.15$; $\sigma'/T' = 1$; $\beta = 0.9$; $n = 1.37$). Here, the histograms show that as the absorption value increases, the intensities in the channels decreases (peak move to the left side of the histogram plot).

To observe the functionality of the new model, I rendered some face images using the diffuse surface normal estimated using the Spherical gradient lighting technique [64]. To compute the RGB values for the skin, I assume that the channel Red = $1.35L_O$, Green = $0.95L_O$, Blue = $0.75L_O$. Figure 3.7 and 3.8 show the rendering using the new model for Gaussian and Exponential respectively, while Figure 3.9 and 3.10 are their histograms (respectively).

3.3 The quality of fit test for the new model

The new model is foremost a surface rendering light scattering model. It is proper to investigate its quality of fit accuracy when fitting on the different type of materials, not just skin. Hence, the author wants to observe how good the new model quality of fit is when uses on other materials and also to investigate its limitation. The new model's fitting accuracy will be tested using two different database: 1) the Columbia-Utrecht Reflectance and Texture (CUReT) database [12], and 2) the Ústav Teorie Informace a Automatizace (UTIA) database [18]. The CUReT was chosen to test how the new model manages the isotropic samples, while the UTIA was chosen to test the new model on anisotropic samples. The objective of these tests is to do a model fitting on the measurements (radiance data) by varying the model's parameters (using an exhaustive method) to search the minimum Root Mean Square error (Δ_{RMS}). The tests will be done on each color channel (RGB) to observe and analyze what factor does the model's parameters (especially the defined absorption parameter) have on the overall fitting.

3.3.1 The CUReT Database

The Columbia-Utrecht Reflectance and Texture (CUReT) database referred to throughout this experiment is the publicly available BRDF database from Dana et. al. [12] that contains reflectance measurements for over 61 different samples, each with over 205 different combinations of viewing and illumination directions observed (Figure 3.11 shows some of the CUReT samples). The database is a result of collaborated work undertaken by the researchers at Columbia University and Utrecht University. This joint effort was sponsored, in part, by REALISE of the European Commission, the National Science Foundation and by DARPA/ONR under the MURI Grant No. N00014-95-1-0601.

It was created in order to study the visual appearance of real-world surfaces and so

that they would be made publicly available to any researcher who wants to evaluate the performance of existing and/or future BRDF models and/or representations. The database measurement procedure requires several pieces of equipment, namely a personal computer with a 24-bit RGB frame grabber, a robot arm to orient the texture samples, a halogen bulb with a Fresnel lens which produces a parallel beam, a photometer, and, finally, a 3-CCD color video camera for capturing the BRDF samples in 10×10 cm stills [12]. An image is captured by the frame grabber for every combination of illumination and viewing direction within each sample. These images are consist of 640×480 pixels with 24 bits per pixel (8 bits per RGB channel). After being captured, they are radiometrically calibrated to get radiance and BRDF from pixel values. The database has also made a table which gives the illumination and viewing direction associated with the 205 measurements available for the general public.

Figure 3.11: 10 CUReT samples. Image taken from [12].

3.3.2 Model fitting on the CUReT samples

Here we excluded the BRDF measurements that occur in the specular direction, and which total 198 non-specular measurements. In total 13 different material samples were selected for the experiment. The test was performed on the color channels of the different samples (RGB), giving a total of 39 sample BRDFs. Before the fitting, the tabulated BRDF data $v(\theta_i, \phi_i, \theta_s, \phi_s)$ were converted into normalized outgoing radiance $L_o(\theta_i, \phi_i, \theta_s, \phi_s)$ using $L_o(\theta_i, \phi_i, \theta_s, \phi_s) = v(\theta_i, \phi_i, \theta_s, \phi_s) L_i \cos(\theta_i) d\omega$. We experimented with fitting four different models to the CUReT data, namely a) the proposed model with an Exponential correlation function, b) the proposed model with Gaussian correlation function, c) the approximate

Bidirectional scattering-surface reflectance distribution function (BSSRDF) model and d) the Oren–Nayar model. This is to observe and compare the models overall quality of fit. The Oren–Nayar model were based on [12] equation derivation, which includes inter-reflections. Note that only the diffuse component was used. Meanwhile, the Jensen's BSSRDF approximation total diffuse reflectance equation [44] is given by:

$$L_J = \frac{\alpha'}{2\pi}\left(1 + \exp^{-\frac{4}{3}\frac{1+Fr}{1-Fr}\sqrt{3(1-\alpha')}}\right)\exp^{-\sqrt{3(1-\alpha')}} \tag{3.15}$$

Where, Fr is the Fresnel formula and α' is the apparent albedo, given by $\alpha' = \sigma_s/\sigma_s + \sigma_a$. Here, σ_s and σ_a are both scattering and absorption coefficient.

The normalized predicted radiance of the models is fitted to the normalized measured radiance data from the CUReT database. This is done by varying the model parameters to find their smallest value of the root-mean-square error Δ_{RMS}. The RMS fitting error is given by:

$$\Delta_{RMS} = 100 \times \frac{1}{K}\Big\{\sum_{k=1}^{K}\Big[L_O^D\left(\theta_i^k, \phi_i^k, \theta_s^k, \phi_s^k\right) - L_O^P\left(\theta_i^k, \phi_i^k, \theta_s^k, \phi_s^k, \frac{\sigma}{T}, \frac{\sigma'}{T'}, n, \beta\right)\Big]^2\Big\}^{\frac{1}{2}} \tag{3.16}$$

where L_O^D is the normalized BRDF from the CUReT database, L_O^P is the normalized radiance from the model prediction and k runs over the index number of the BRDF measurements used (K).

There are four parameters in the proposed model that are varied in the exhaustive search for a best-fit. The values of σ/T and σ'/T' are made equal in this search. The ranges for the parameters used in the experiment are: $\sigma/T = \sigma'/T'$ which ranges from (0.12 to 4.1) with 50 equal intervals, β which ranges from (0.01 to 1) with 100 equal intervals, the index of refraction, with a range of (1.3 to 1.5) with 10 equal intervals, and a with a range of (0 to 1) with 101 equal intervals. The range for σ_a and σ_s for the BSSRDF model (or Jensen model) [44] are varied between (0.01 to 1) with 100 intervals. Meanwhile, for the Oren–Nayar model [12], the parameter values were chosen based on the tabulated data given, but using only the diffuse component. Some of the results are shown as plots of normalized measured data versus the normalized radiance predicted by the different models on each RGB channels (See Figures 3.12 and 3.13). Meanwhile, Table 3.2 shows the Δ_{RMS} fit results done on 13 samples for each color channel. The gray colored cells highlight the model fitting of samples with $\Delta_{RMS} < 0.5$. It can be seen from the table that the new exponential model gives the best overall fit for all 13 samples on all color

channels, followed by the new Gaussian model. Here, the samples were selected based on the different degree of surface conditions, such as how strongly chromatic and how rough the surface is. The author was unable to use all of the samples in the database due to the author's insufficient information on building a more efficient program for the experiment at the time. This cost the author a lot of time to test a sample (one to two days), forcing the author to select samples based on how rough (from less rough surface - Felt; to highly rough surface - Quarry tile) and how strongly chromatic the samples are (less chromatic - Felt; to highly chromatic - Velvet). The author noted that most of the samples used here are not layered materials (e.g. Velvet, Sponge and Quarry tile). Nevertheless, the test was done to observe the limitations of the new model when dealing with this kind of samples. In the experiment results (see Table 3.2), Velvet is the highest overall error obtained by the new model, while Sponge is the lowest overall error.

The new model is capable to give a good fit for rough surfaces (e.g. Quarry tile, Brown Bread, and Rug-B), with Sponge giving the best results. However, the new model is less accurate when fitting mediocre roughness and highly chromatic samples —samples that emit mostly single colour (e.g. emitted only red colour), like the Velvet sample. This is due to how simplistic the absorption term was defined in the new model, the new model may not accurately predict samples that are rough and highly chromatic materials. Nevertheless, for most rough colored samples, the new model still give the best quality of fit results when compare to other models. Meanwhile, when comparing the new model with the R–H model (see Table 3.3), there are several samples estimated by the new model to have $a = 0$. Noted that the new model will become similar to R–H model when $a = 0$, this causes the Δ_{RMS} for some samples from the new model to have similar Δ_{RMS} with that of R–H model (see Table 3.3). However, there are 6 chromatic samples that gave better results when using the new absorption model (samples estimated by the new model with $a \neq 0$); these samples were Rug-B (red), Velvet (red), Quarry tile (pale red), Brown bread, Orange peel and Moss (green). This shows that the proposed model accounts well for chromatic effects in colored samples when compare to R–H model.

3.3.3 CUReT result analysis and discussion

There are three observations highlights from this CUReT model fitting test: Firstly, is that when the absorption fraction a in the modified absorption model is zero, the model is equivalent to Ragheb–Hancock model. Secondly, the modified absorption model gave the

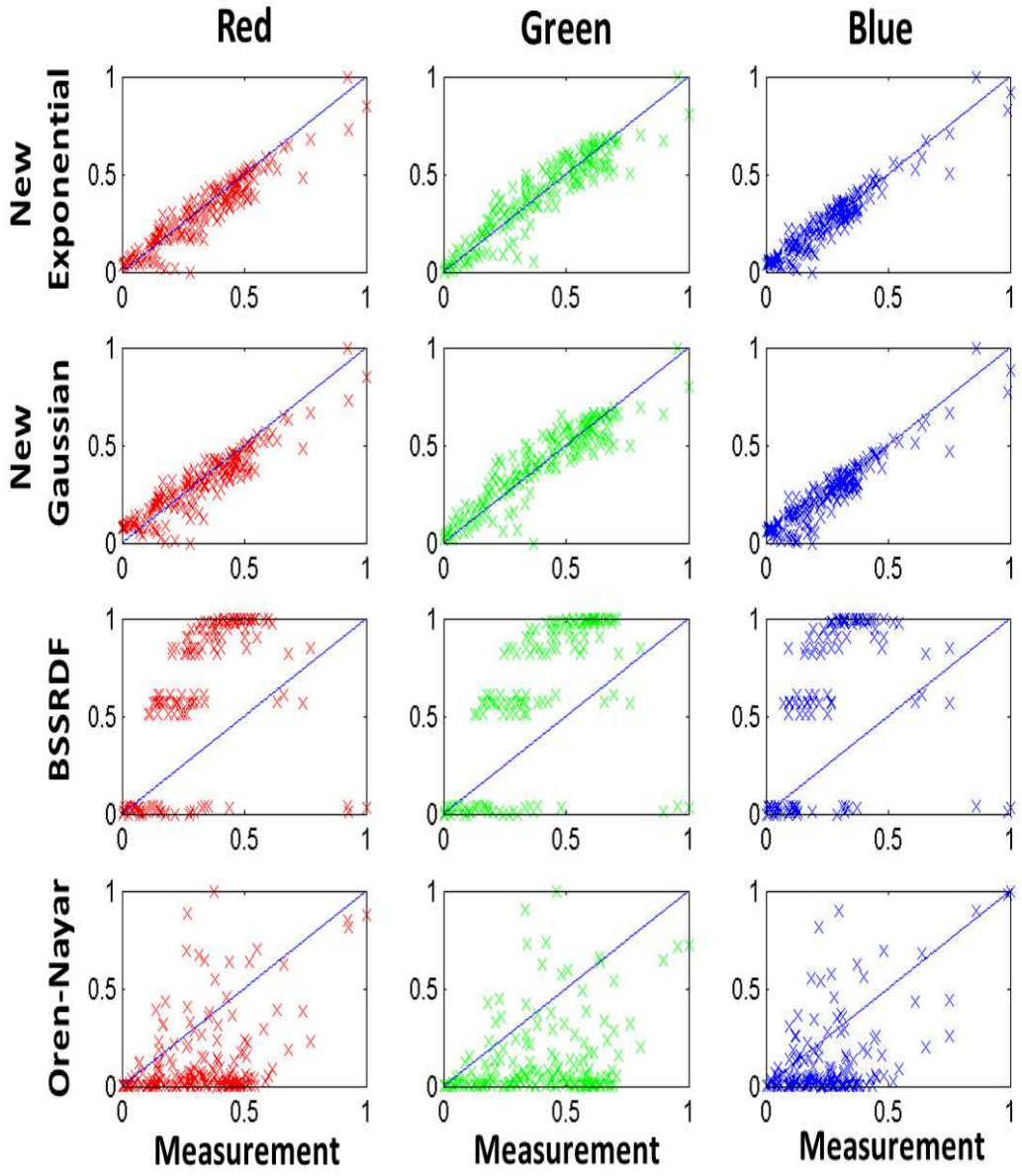

Figure 3.12: Plot for normalized measured data versus normalized model radiance prediction for the sample Soleirolia Plant (53). New Exponential (1st row); New Gaussian (2nd row); BSSRDF (3rd row); Oren–Nayar (4th row) for Red (left column), Green (middle column) and Blue (right column) channels.

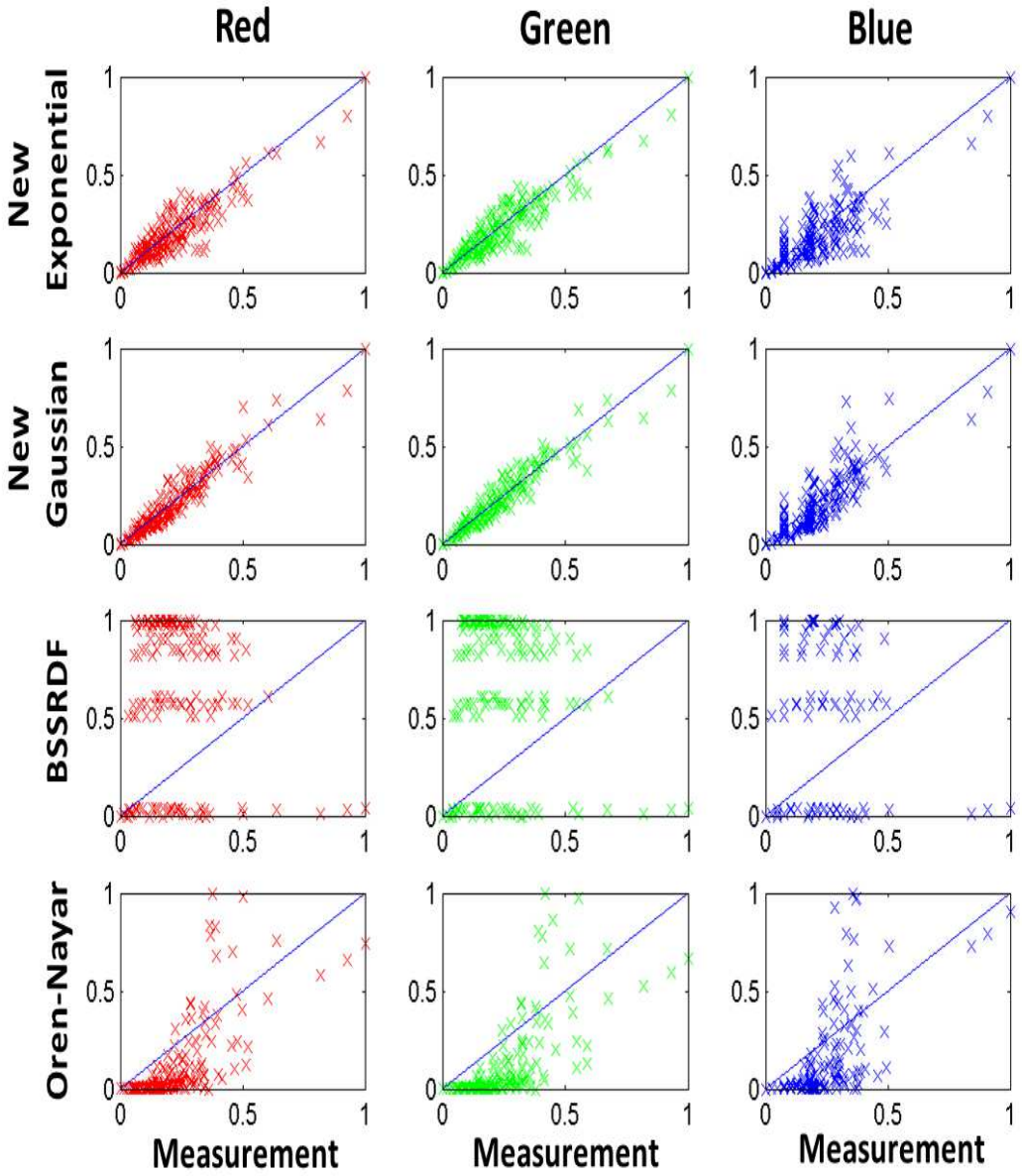

Figure 3.13: Plot for normalized measured data versus normalized model radiance prediction for the sample Moss (61). New Exponential (1st row); New Gaussian (2nd row); BSSRDF (3rd row); Oren–Nayar (4th row) for Red (left column), Green (middle column) and Blue (right column) channels.

Table 3.2: The Δ_{RMS} corresponding to the models studied for selected CUReT samples. The gray cells highlight $\Delta_{RMS} < 0.5$

Sample (no.)	Exp_R	$Gaus_R$	Jen_R	ON_R	Exp_G	$Gaus_G$	Jen_G	ON_G	Exp_B	$Gaus_B$	Jen_B	ON_B
Felt (1)	0.4614	0.5205	2.6657	3.0177	0.4282	0.4818	2.8145	2.5626	0.5413	0.5945	1.8640	3.7595
Terry Cloth (3)	0.5159	0.5440	1.5696	3.7849	0.5064	0.5319	1.5582	3.7940	0.5052	0.5250	1.5383	3.8126
Velvet (7)	1.3626	1.0220	3.2774	1.5568	0.8966	0.9469	5.0024	0.6819	0.9171	0.9501	4.9259	6.1236
Rug-A (18)	0.4203	0.4812	2.3808	2.7587	0.4006	0.4659	2.4446	2.8536	0.3693	0.4347	2.8100	2.4729
Rug-B (19)	0.6179	0.4420	3.1501	1.4729	0.3251	0.3188	4.5258	1.0338	0.3315	0.3312	4.5200	1.0381
Sponge (21)	0.3180	0.3819	2.0959	2.4739	0.2569	0.3127	2.8727	2.4632	0.2112	0.2662	3.7463	1.6272
Quarry Tile (25)	0.4368	0.4808	3.6416	1.2946	0.3786	0.3935	4.5629	1.1512	0.3716	0.3853	4.7954	6.3168
Brown Bread (48)	0.3736	0.4523	2.6015	2.3133	0.3585	0.4373	3.0615	2.3286	0.3047	0.3747	3.7275	1.7031
Corn Husk (51)	0.6466	0.6626	1.8945	3.1789	0.6546	0.6767	1.9531	3.5755	0.4938	0.5131	3.1144	2.2818
White Bread (52)	0.4276	0.5038	1.5637	3.8676	0.4166	0.5050	1.6230	3.8585	0.3774	0.4737	2.0420	3.3901
Soleirolia Plant (53)	0.4507	0.5015	3.3256	2.1832	0.5563	0.5985	2.6582	2.7362	0.3809	0.4348	3.7405	1.6787
Orange Peel (55)	0.7394	0.7915	2.8696	1.2485	0.3794	0.4500	4.6247	0.9470	0.3204	0.3662	5.2467	0.4896
Moss (61)	0.4102	0.3386	4.3900	1.2580	0.3767	0.3265	4.2371	1.3651	0.6432	0.5678	4.4290	1.3021

Table 3.3: The Δ_{RMS} corresponding to the new model and R–H model studied for the selected CUReT samples. The parameter 'a' here correspond to the new model estimation of absorption. The gray cells highlight samples with $a \neq 0$. Noted that for the new model, when $a = 0$, the new model become similar to R–H model.

	Exponential									Gaussian								
Sample (no.)	Red			Green			Blue			Red			Green			Blue		
	New	R-H	a	New	R-H	a	New	R-H	a	New	R-H	a	New	R-H	a	New	R-H	a
Felt (1)	0.4614	0.4614	0	0.4282	0.4282	0	0.5413	0.5413	0	0.5205	0.5205	0	0.4818	0.4818	0	0.5945	0.5945	0
Terry Cloth (3)	0.5159	0.5159	0	0.5064	0.5064	0	0.5052	0.5052	0	0.544	0.544	0	0.5319	0.5319	0	0.525	0.525	0
Velvet (7)	1.3626	1.3626	0	0.8966	0.9017	1	0.9171	0.9197	1	1.0222	1.022	0	0.9469	0.9494	1	0.9501	0.9507	1
Rug-A (18)	0.4203	0.4203	0	0.4006	0.4006	0	0.3693	0.3693	0	0.4812	0.4812	0	0.4659	0.4659	0	0.4347	0.4347	0
Rug-B (19)	0.6179	0.7677	0.484	0.3251	0.3343	1	0.3315	0.3392	1	0.442	0.4888	0.361	0.3188	0.3216	1	0.3312	0.3335	1
Sponge (21)	0.318	0.318	0	0.2569	0.2569	0	0.2112	0.2112	0	0.3819	0.3819	0	0.3127	0.3127	0	0.2662	0.2662	0
Quarry Tile (25)	0.4368	0.4559	0.292	0.3786	0.4307	0.815	0.3716	0.3807	1	0.4808	0.51	0.37	0.3935	0.4542	0.861	0.3853	0.3983	1
Brown Bread (48)	0.3736	0.3739	0.029	0.3585	0.3707	0.176	0.3047	0.3249	0.355	0.4523	0.4523	0.002	0.4373	0.4393	0.072	0.3747	0.3838	0.389
Corn Husk (51)	0.6466	0.6466	0	0.6546	0.6546	0	0.4938	0.4938	0	0.6626	0.6626	0	0.6767	0.6767	0	0.5131	0.5131	0
White Bread (52)	0.4276	0.4276	0	0.4166	0.4166	0	0.3774	0.3774	0	0.5038	0.5038	0	0.505	0.505	0	0.4737	0.4737	0
Soleirolia Plant (53)	0.4507	0.4507	0	0.5563	0.5563	0	0.3809	0.3809	0	0.5015	0.5015	0	0.5985	0.5985	0	0.4348	0.4348	0
Orange Peel (55)	0.7394	0.7394	0	0.3794	0.3798	0.259	0.3204	0.333	1	0.7915	0.7915	0	0.45	0.453	0.409	0.3662	0.3805	1
Moss (61)	0.4102	0.5135	1	0.3767	0.5326	1	0.6432	0.694	1	0.3386	0.3796	1	0.3265	0.3926	0.87	0.5678	0.5819	1

least model fitting error, and thirdly, the BSSRDF model was observed to overestimated the outgoing radiance prediction and the Oren–Nayar model was observed to underestimated it.

To measure the discrepancy existing between the best-fit error (observation data) and its expected error, the chi-squared per degree of freedom test was used to check whether the Ragheb–Hancock model and the absorption model differ significantly. The Chi-squared statistic is given by:

$$\chi^2 = \sum_{k=1}^{K} \frac{(Model_k - Data_k)^2}{Data_k} \tag{3.17}$$

Table 3.4: The Chi-Square test per Degree of Freedom for the selected CUReT samples.

Sample (No.)	New Model						Ragheb Model					
	Exponent			Gaussian			Exponent			Gaussian		
	R	G	B	R	G	B	R	G	B	R	G	B
Felt (1)	0.0327	0.0369	0.0378	0.0419	0.0493	0.0482	0.0327	0.0367	0.0376	0.0417	0.0491	0.0480
Terry Cloth (3)	0.0115	0.0112	0.0111	0.0128	0.0123	0.0118	0.0114	0.0112	0.0111	0.0127	0.0123	0.0118
Velvet (7)	0.0633	0.1328	0.2049	0.0442	0.1500	0.2161	0.0630	0.1332	0.2077	0.0440	0.1496	0.2183
Rug-A (18)	0.0293	0.0242	0.0193	0.0596	0.0546	0.0445	0.0291	0.0241	0.0192	0.0593	0.0543	0.0443
Rug-B (19)	0.0193	0.0131	0.0135	0.0101	0.0126	0.0133	0.0314	0.0140	0.0143	0.0146	0.0131	0.0136
Sponge (21)	0.0052	0.0040	0.0039	0.0160	0.0111	0.0187	0.0052	0.0040	0.0039	0.0159	0.0111	0.0186
Quarry Tile (25)	0.0238	0.0116	0.0206	0.0275	0.0149	0.0199	0.0256	0.0228	0.0229	0.0320	0.0268	0.0226
Brown Bread (48)	0.0205	0.0189	0.0120	0.0512	0.0438	0.0220	0.0208	0.0227	0.0162	0.0520	0.0454	0.0278
Corn Husk (51)	0.0298	0.0294	0.0240	0.0272	0.0288	0.0219	0.0297	0.0293	0.0239	0.0271	0.0286	0.0218
White Bread (52)	0.0438	0.0381	0.0731	0.0746	0.0623	0.1845	0.0436	0.0379	0.0728	0.0743	0.0620	0.1836
Soleirolia Plant (53)	0.0231	0.0183	0.0182	0.0588	0.0247	0.0285	0.0230	0.0182	0.0181	0.0585	0.0246	0.0283
Orange Peel (55)	0.0912	0.0218	0.0255	0.0962	0.0296	0.0424	0.0907	0.0220	0.0277	0.0957	0.0305	0.0457
Moss (61)	0.0122	0.0112	0.0356	0.0083	0.0083	0.0287	0.0231	0.0261	0.0461	0.0116	0.0136	0.0321

After obtaining the chi-squared statistic, it is then divided by v the number of degrees of freedom to give χ^2/v the chi-squared per degree of freedom, where $v = d - p$. Here, $d = 198$ which is the number of data samples and p is the number of model parameters. For the Ragheb–Hancock model, $p = 3$ while the proposed model has $p = 4$. A comparison of the Ragheb–Hancock model and the proposed absorption model is given in Table 3.4. It was found out that there is no significant difference between the chi-square test for the Ragheb–Hancock model and the proposed absorption model. However, a total of 6 chromatic samples gave better results using the proposed absorption model; these samples were Rug-B (red), Velvet (red), Quarry tile (pale red), Brown bread, Orange peel and Moss (green). This shows that the proposed model accounts well for chromatic effects in colored samples. Even though there is no significant different in the chi square test between the two models, the absorption parameter in the new model have certain influence in the overall model parameter estimation. Between the two variants, the new Exponential model has the lowest average Δ_{RMS} for all channels than the new Gaussian model. Meanwhile, Figure 3.14 shows the spheres absorption colours rendering for two CUReT samples using the new model estimated parameters.

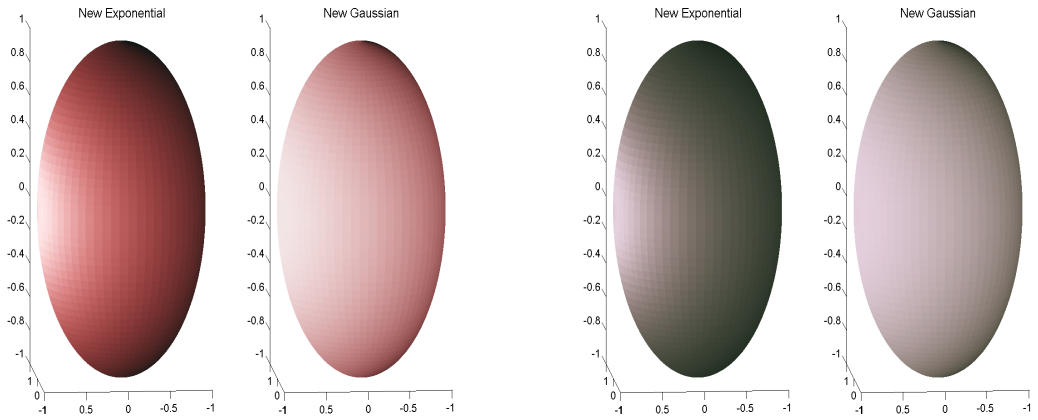

Figure 3.14: Rendering for two of the CUReT samples using the new model estimated parameters. The two left sphere is for the Brown Bread (48) sample, while the two right sphere is for the Quarry Tile (25) sample. The new Gaussian model rendering is much brighter than the Exponential. However, the new Gaussian Δ_{RMS} is much higher than Exponential (See Table 3.2).

3.3.4 The UTIA database

The Ústav Teorie Informace a Automatizace (or the Institute of Information Theory and Automation in English) UTIA database is a collection of samples that deal with full four-dimensional anisotropic BRDF [18]. The database contains 150 measurements relating to a wide range of materials with elevation directions 15^o and azimuthal directions 7.5^o apart (6 x 48 illumination directions and 6 x 48 view directions).

All of their data were captured using their own high precision robotic gonioreflectometric device [19]. The device consist of two independently controlled arms with one arm containing a custom-build LED light (12 000 lux) and another arm containing a 16Mpix RGB camera AVT Pike 1600C with their distance from the sample are 1.1 m and 2.1 m. The arm positioning accuracy is calculated as being 0.03^o (see Figure 3.15).

The authors in [18] recorded the samples in HDR using five combinations of lighting intensity and camera exposure relative to the measured material reflectivity. Radiometric and colorimetric calibration were performed prior to each measurement, having the uniform angular density of $81 \times 81 = 6561$ directions. All of data were recorded as float values and the 4D anisotropic BRDF were stored as 2D images divided into azimuthally dependent BRDF subspaces for fixed elevation angles (see Figure 3.16). Each of the BRDFs measurements for the 81×81 hemispherical uniform sampling, resulted in a variable count

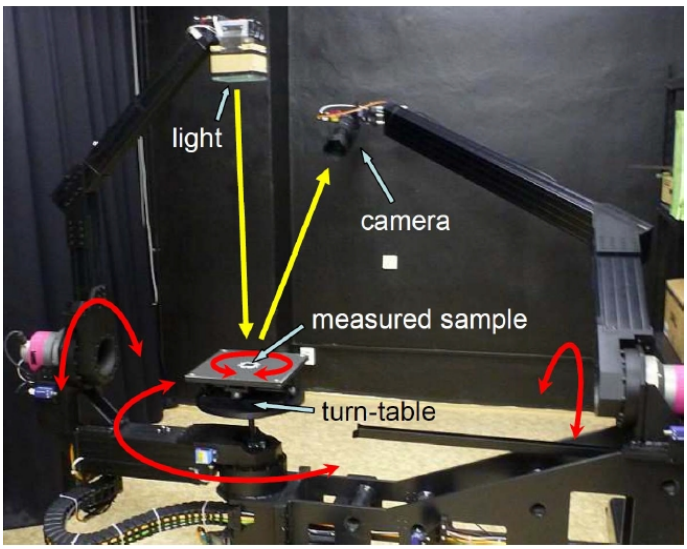

Figure 3.15: The gonioreflectometric device used to measure the UTIA database. Image taken from [19].

of samples at different elevation angles. The authors then converted these 6561 samples to angularly uniform directions, where they measured $6 \times 48 \times 6 \times 48 = 82944$ different directions using an interpolation based on the radial basis function (see Figure 3.17).

To obtain access to this database, I sent an email request to M. Haindl and explained that I wanted to use the database for my model experiment. He responded stating that he would gladly offer it to me and requested that I share my findings with him after I finished my research.

3.3.5 The quality of fit test on the UTIA samples

Where the CUReT database contained isotropic samples, the UTIA database has anisotropic ones [18]. Here, the UTIA samples were used to test how the new model fare with samples that retain its anisotropic characteristics. The quality of fit test is done at 6 different elevation angles for θ_i and θ_v from $[0^o, 75^o]$ with 15^o apart; and 47 different azimuthal angles for ϕ_v with 7.5^0 apart. The azimuthal angles were made to be $\phi_i = 0^o$ and $\phi_v = \mid \phi_{i\_database} - \phi_{v\_database} \mid$. Also, the data in the specular direction were not included. This makes a total of 1722 different directions used in the experiment. Five models were used in the fitting test: The new model (Exponential and Gaussian variants); the Ragheb–Hancock model (Exponential and Gaussian variants); and the BSS-RDF model. The model fitting setup and the parameters range for this test (using the

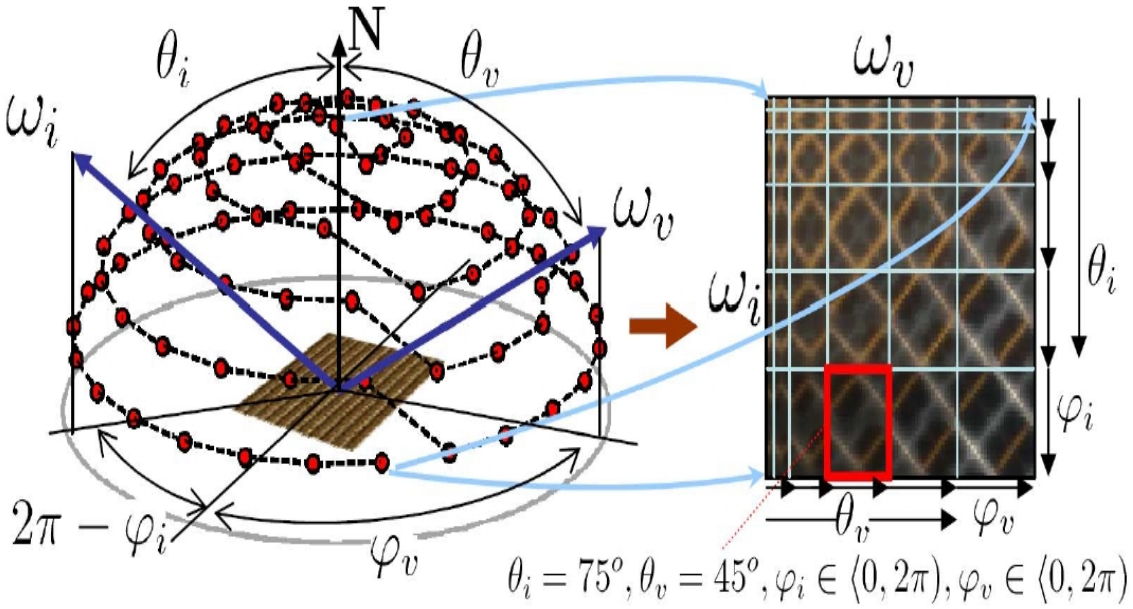

Figure 3.16: The UTIA parameterization of illumination and view directions. Image taken from [19].

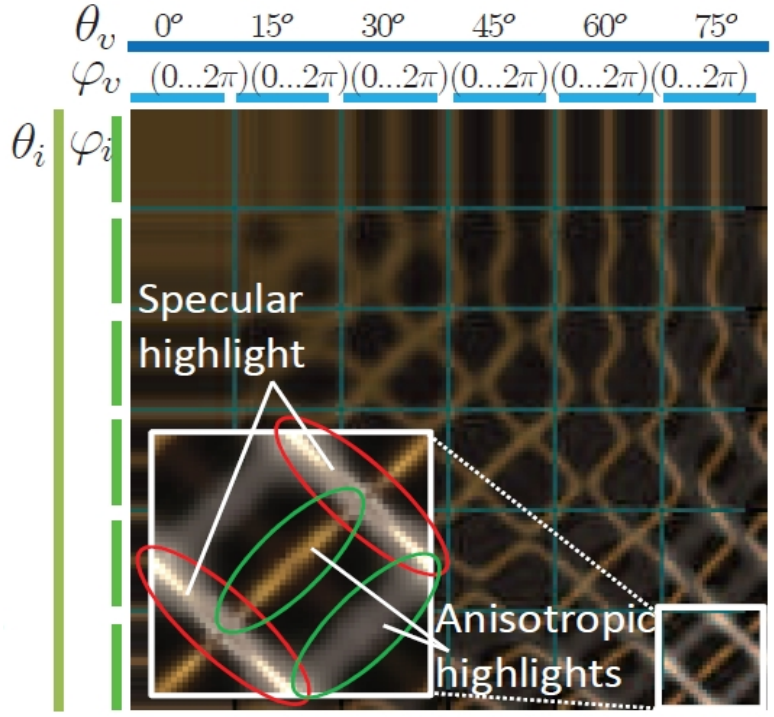

Figure 3.17: The BRDF of a sample (fabric112) with specular and anisotropic highlights in a BRDF subspace. Image taken from [18].

UTIA database) are the same as when doing with the CUReT database, except that a nonlinear least square fitting method (MATLAB function) was used and the refractive index n was changed into (1.2 to 2.0) with 41 intervals. The test was done on 99 different samples. They were: 59 fabrics, 6 carpets, 16 leathers, 10 woods, and 8 other materials such as papers, glitter, plastic, and wallpapers. Based on the database numbering, the selected samples are: m001-m054, m061, m062, m071, m072, m074, m075, m095-m097, m105-m127, m132-m144. Each of the selected samples were then respectively correspond to numbers in ascending order, example - samples m001-m054, m061 and m062 correspond to the number 1 to 56. Figure 3.18, 3.19 and 3.20 show the Δ_{RMS} fitting error for the 99 samples in stacked bar form for each Red, Green and Blue channel respectively.

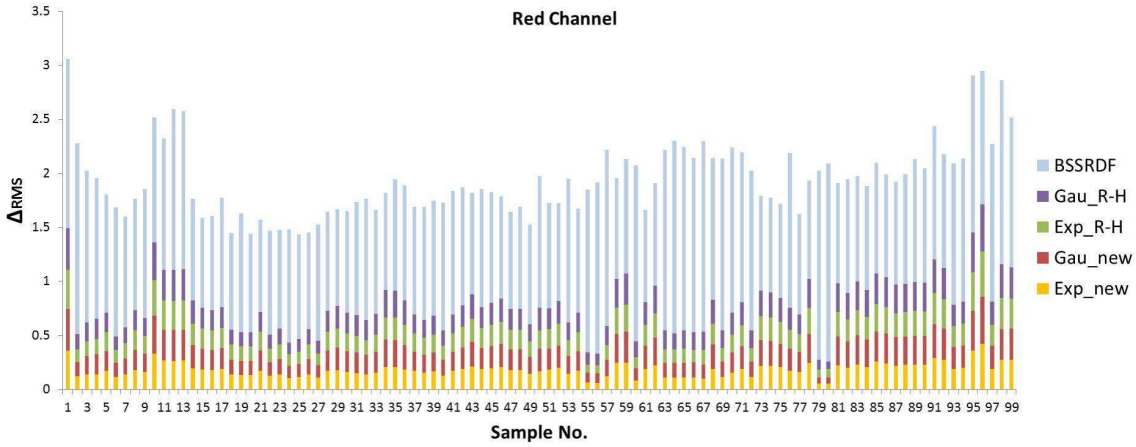

Figure 3.18: The stacked bar plot for the Δ_{RMS} corresponding to the models studied for 99 UTIA samples (Red channel). The bottom bar is the fitting error for the new Exponential, followed by the new Gaussian, the R–H Exponential, the R–H Gaussian, and finally the BSSRDF. The test was done on 6 different elevation angles for θ_i and θ_v; and 47 different azimuthal angles for ϕ_v, while $\phi_i = 0^o$.

3.3.6 UTIA result analysis and discussion

The proposed model obtained the average lowest Δ_RMS error than the Ragheb–Hancock model and the BSSRDF model. Moreover, there are multiple discoveries regarding the test, which are: 1) In the overall 99 samples tested, it was observed that the models obtained high error value when fitting against samples with strong anisotropic highlights. Most of these samples are from fabric materials that have strong anisotropic highlight(s) [18]. 2) All leathers samples having the lowest error overall. Since leather is similar to skin, this

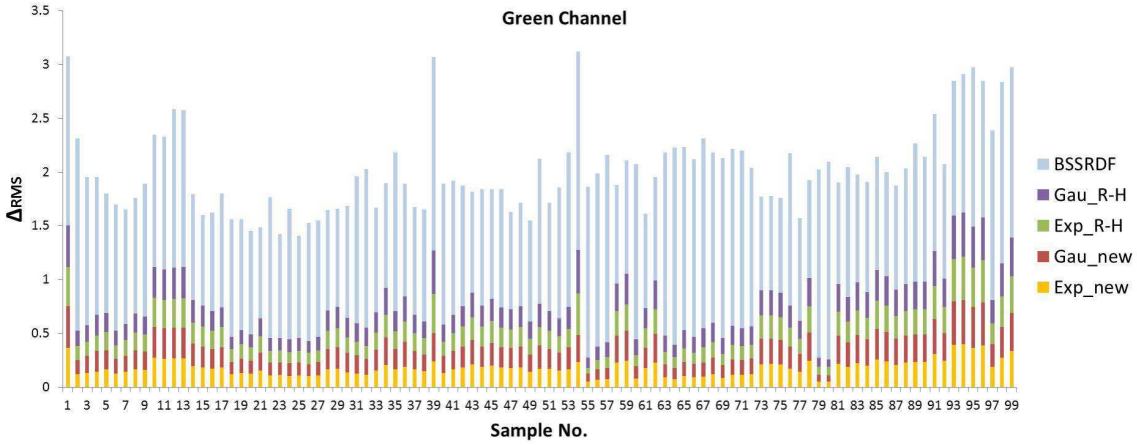

Figure 3.19: The stacked bar plot for the Δ_{RMS} corresponding to the models studied for 99 UTIA samples (Green channel). The bottom bar is the fitting error for the new Exponential, followed by the new Gaussian, the R–H Exponential, the R–H Gaussian, and finally the BSSRDF. The test was done on 6 different elevation angles for θ_i and θ_v; and 47 different azimuthal angles for ϕ_v, while $\phi_i = 0^o$.

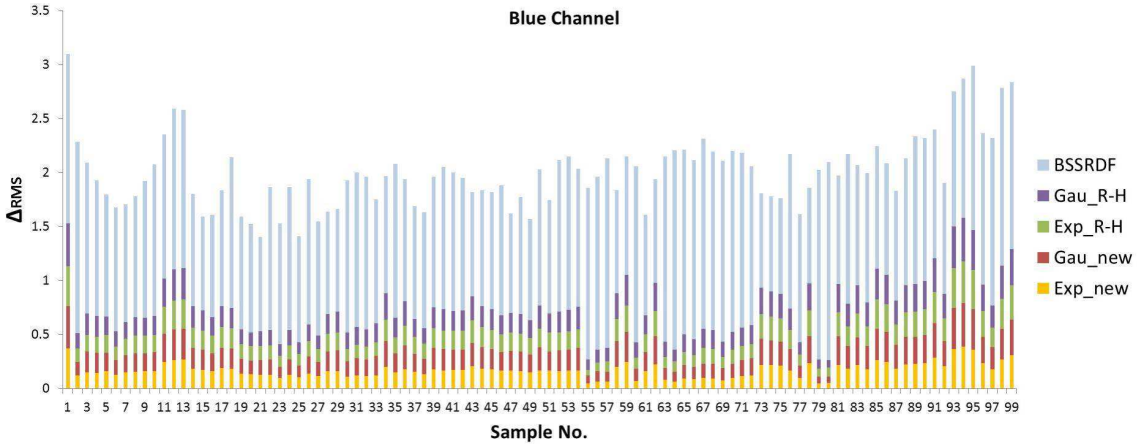

Figure 3.20: The stacked bar plot for the Δ_{RMS} corresponding to the models studied for 99 UTIA samples (Blue channel). The bottom bar is the fitting error for the new Exponential, followed by the new Gaussian, the R–H Exponential, the R–H Gaussian, and finally the BSSRDF. The test was done on 6 different elevation angles for θ_i and θ_v; and 47 different azimuthal angles for ϕ_v, while $\phi_i = 0^o$.

result suggest that the new model may be suitable for modeling skin samples captured in anisotropic condition. 3) The new model and R–H model have slight error difference between the two model variants (Exponential and Gaussian). Nevertheless, the new models have lower total average fitting error (New Exponential = 0.1789; New Gaussian = 0.1982)

than the R–H versions (R–H Exponential = 0.1830; R–H Gaussian = 0.2042). Meanwhile, the BSSRDF have the highest total average fitting error, which is BSSRDF = 1.2254 (see Figure 3.21).

Figure 3.22 shows an example comparison between the proposed (Exponential variant) model prediction and the data measurements for five samples when $\theta_i = \theta_v = 60^o$ with varying incident azimuth and viewing azimuth. It can be seen from the figure that the model fail to predict the anisotropic highlights as seen from the Carpet2, Fabric135, and Fabric136 samples. Figure 3.23 shows the rendering of some UTIA samples using the new absorption model. The spheres show absorption colours. i.e. the surface colour implied by the estimated absorption values in each channel. The top sphere is the sample where the new model fits best, while the bottom one is the sample where the new model fit the least (Samples from the top: Leather16, Fabric096, Fabric135, Fabric111). The difference in rendering between the Exponential and Gaussian is that samples rendered using the new Exponential seems slightly brighter and take fewer iterations to fit with the sample's colour than the new Gaussian for most best-fit samples.

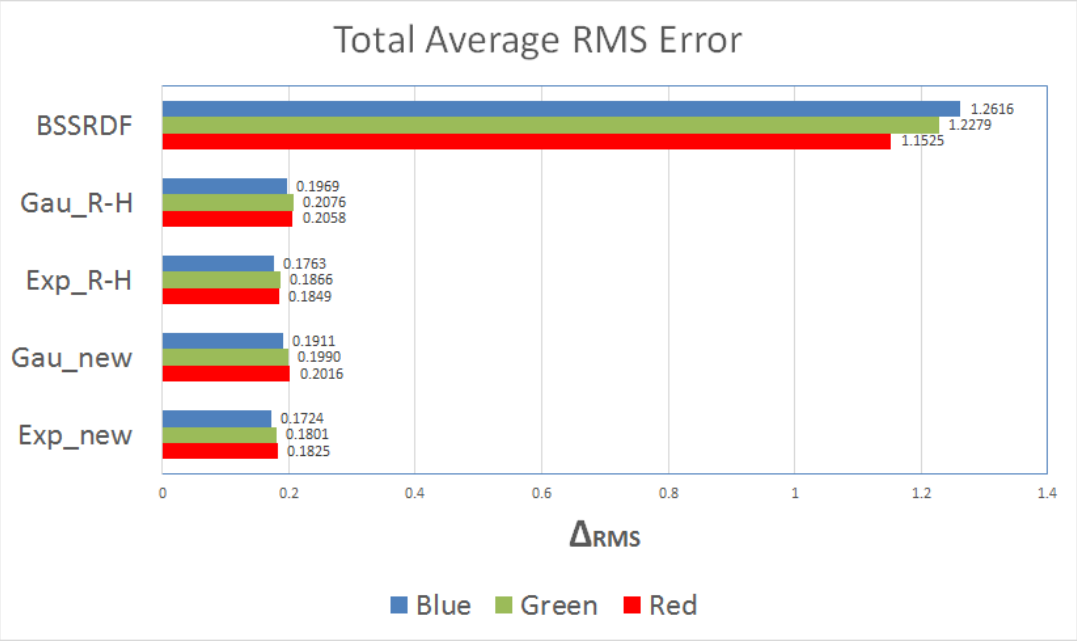

Figure 3.21: The total average Δ_{RMS} error for all UTIA samples used in the experiment.

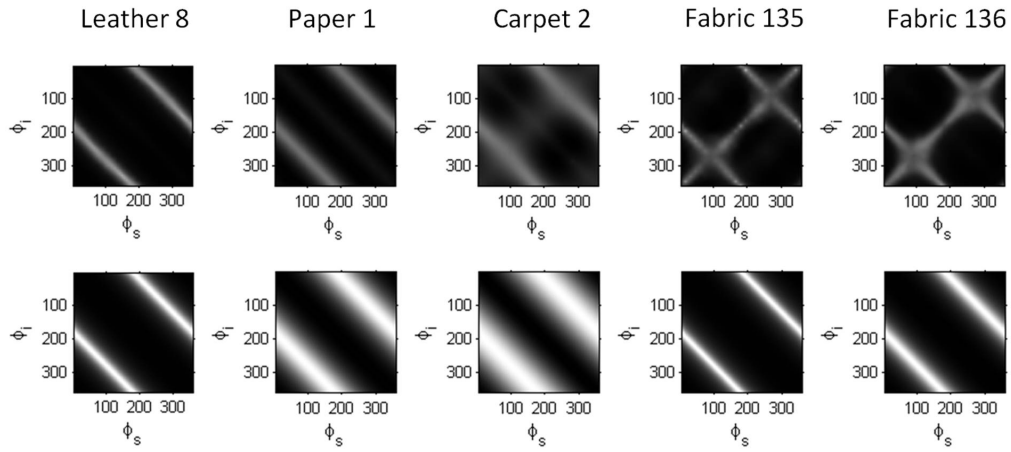

Figure 3.22: The normalized radiance for the measurement (top row) and the modified Exponential model prediction (bottom row) for five samples with various incident azimuth and viewing azimuth ($\theta_i = \theta_v = 60^o$). Note: The axial slice is the highlight near specular angles and the diagonal slice is the anisotropic highlight. The specular component was not included.

3.4 Summary

In this paper, we introduced a new light scattering model for layered rough surfaces with absorption. With regard to the the CUReT database, we have demonstrated that the method is superior to a number of alternative light scattering models, including the Ragheb–Hancock model, which is essentially an absorption-free version of the new method. That is to say the new method handles wavelength dependent chromatic absorption effects, which are beyond the scope of the Ragheb–Hancock model. Although the new model has been tested on a variety of samples in Section 3.3, the author does not claim that all materials for which the experiment obtain a good fit of the model to the data follow the assumptions regarding dual layer (surface and subsurface) and light absorption. The author understands that it is impossible to satisfy the described assumptions for some materials. Nevertheless, the new model builds and improves upon the Ragheb–Hancock model, not only for the purposes of analyzing subsurface roughness, but also with regard to analysis of the absorption characteristics of materials. This offer a significant advantage when studying biological materials, such as the human skin. Furthermore, the new model can handle samples that are not highly anisotropic, which shown in the experiment using the UTIA database. The lowest error obtained by the new model was when the model considered the leather type materials which resemble skin. This means that we can assume

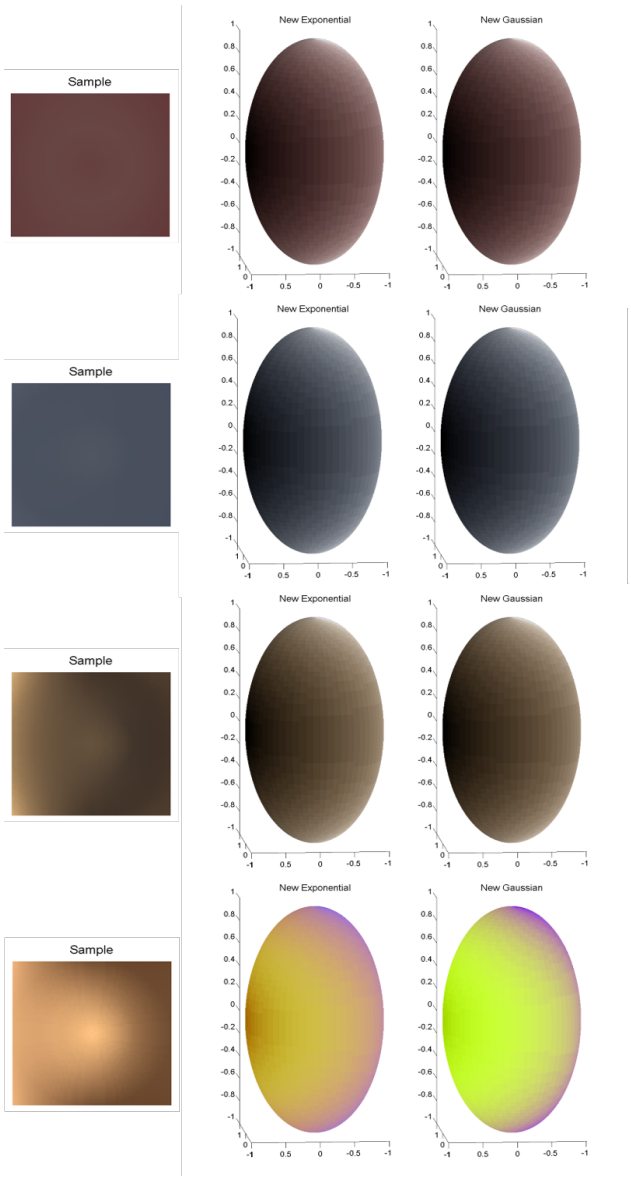

Figure 3.23: Rendering using some of the UTIA samples, The top figure is the sample where the new model fits best, while the bottom one is the sample where the new model fit the least (Samples from the top: Leather16, Fabric096, Fabric135, Fabric111).

that the new model is suitable for the experiment which will be undertaken in this thesis, namely the parameter-age test in Chapter 5. In addition, the new model allows us to estimate the absorption percentage 'a', thus providing information concerning the light absorption characteristic of a material, and, ultimately, enabling us to analyze the light absorption properties of the skin in the parameter-age test later on.

Chapter 4

Parameter analysis and selection

In order to investigate the model parameter relationship with aging, appropriate parameters from the model need to be selected first. It is essential to select the appropriate parameters that are able to be practically related to the measurements such as the surface skin roughness or the refractive index [20, 22, 38, 39, 47, 51, 62, 91, 112]. However, due to equipment and resource limitation at the time, the author was unable to get the real measurements of the materials such as the surface roughness where roughness measuring instrument are needed. Hence, an alternative method is used. It was known that polarization is directly related to how a material scatters light. The material properties such as the surface roughness, the subsurface roughness, and the light absorption can directly affect how polarization will behave [5, 6, 30, 37, 48, 52].

To validate the new model parameter relation with the material's known measurement, the author decided to use the degree of polarization (DOP), which is one of the material's property, to be compared with the model parameters. The author noted that the DOP is an independent measurement –different from the new model parameters, but it is the material property that the author able to measure using the current equipment available at the time. In this chapter, the relationship between the two is compared and analyzed by first completing a correlation test between the object measurement (degree of polarization - DOP) and the model parameters to see whether the estimations are in agreement with each other (e.g. by reference or by the practical characteristics of the object). Furthermore, the test will be conducted using materials with varying degree of properties (e.g. very rough surface; highly chromatic). The parameters that have a significant correlation with the material's polarization will be selected for the later parameter-age test, which is in Chapter 5.

The discussions relating to the correlation test constitute the first half of this chapter. The second half will outline the experiment setup for the image capturing process and the introduction of a new image alignment technique. There are several limitations to consider when capturing non-static subjects, so the second part of the chapter will thoroughly explain how our alignment technique addresses these issues.

Sections 4.1 to 4.6 describe the parameter selection experiment, including setup, test results, and the finalization of parameter selection. The Zhang and Hancock comprehensive polarization model [109] is used in conjunction with the proposed scattering model to investigate which model parameters should be used for the later parameter-age experiment (will be mentioned in chapter 5). Afterwards, sections 4.4 to 4.5.5 describe the light stage setup designed to capture the subject's face for the parameter-age experiment and, also, present the new alignment technique that accounts for errors resulting from small movements between image sequences captured in environments with disparate illumination. Alignment accuracy tests and discussion regarding future improvements to the technique will also be included.

4.1 Relating skin properties to parameters

The new scattering model has four parameters that define how the light scattering should behave when reflecting from a surface. These parameters can easily be related to the characteristics of human skin. Table 4.1 shows the predictions of the parameters behavior based from several sources. Additionally, the test will be conducted on all RGB channels, so it is possible that the results for each color channel will have different parameter strength. Noted that, when using the parameter as a feature for estimating age, it is better to use the parameter in a channel that is strongly affected by aging (i.e. using surface roughness parameter estimated using the red channel for skin, since it is the colour light most scatter and less absorb by skin).

To prove that the parameters of the new model can be related to the properties of the object, we completed correlation tests between the object's light scattering parameters and the object's degree of polarization (DOP). The reason that the material's polarization was chosen for this test is because the polarization of the reflected light depends on the symmetry of the arrangement of the incident probing light (i.e. surface of the material) with respect to the absorbing transitions dipole moments (i.e. light absorption) in the material [5, 6, 30, 37, 48, 52]. If there is a change in either of these parameters, they might

Table 4.1: The behavior prediction for the New model parameters when apply on different aging skin

Parameter	**Young skin**	**Old Skin (parameter's behavior prediction)**	**Reference**
Surface slope (σ/T)	Smooth micro-structure surface, good lipid production, low skin contrast.	Rough micro-structure surface, bad lipid production, high skin contrast (σ/T value increases).	[20, 22, 36, 38, 39, 41–43, 50, 53, 104, 112]
Refractive index (n)	Normal Lipid production, healthy skin with average water content.	Less Lipid production, dry skin with less water content (n value increases).	[39, 41–43, 53, 112]
Balance Parameter (β)	Plump skin, thicker skin layers, probably dominate by the subsurface component of the model.	Dry skin, thinner skin layers, probably dominate by the surface component of the model (β value decreases).	[36, 41–43, 47, 51, 53, 62, 91, 112]
Absorption (a)	Healthy skin, good melanin production, probably have lower absorption on the red band but higher on other bands.	Dry skin, bad melanin production, probably have variance absorption values on all the bands (depend on the colour band and also skin type).	[14, 15, 20, 22, 39, 41–43, 98, 112]

also be a change in the polarization degree. In this test, the DOP is calculated using Zhang and Hancock's comprehensive polarization reflectance model [109].

4.2 Comprehensive polarization reflectance model

Polarization is the process of transforming a random fluctuate electrical field into a well defined one. In the field of computer vision, Fresnel Theory is generally used to predict how polarized light interacts with a surface. The theory has other applications, such as reflectance component separation, surface analysis and surface normal recovery [4, 64, 109, 110].

Using both Fresnel theory and Malus law, Zhang and Hancock [109] developed a comprehensive polarization reflectance model that combines both the underlying physics of specular and diffuse polarization. They used the model to estimate shape from image intensity by defining their model to relate the degree of polarization (DOP) ρ to the zenith angle θ. In this section, the comprehensive polarization model will be used for estimating a sample's polarization property.

The equation for the DOP curve is referred from Zhang and Hancock [109]. The values that can be determined from the calculation are: the amplitude reflection coefficient for

light polarized perpendicular to the plane of incidence, $r_\perp$, which is given by:

$$r_\perp(n_i, n_t, \theta_i) = \frac{n_i \cos\theta_i - n_t \cos\theta_t}{n_i \cos\theta_i + n_t \cos\theta_t} \tag{4.1}$$

and the amplitude reflection coefficient for light polarized parallel to the plane of incidence, $r_\parallel$:

$$r_\parallel(n_i, n_t, \theta_i) = \frac{n_t \cos\theta_i - n_i \cos\theta_t}{n_t \cos\theta_i + n_i \cos\theta_t} \tag{4.2}$$

The θ_i and θ_t are the angles of incident and transmission, while n_i and n_t are the refractive indexes of air and material respectively. Here, the refractive index of air is assumed equal to 1. Using the Snell's law, the angle θ_t can be replaced with:

$$\theta_t = \sin^{-1}(\frac{\sin\theta_i}{n_t}) \tag{4.3}$$

Generally, it is not the amplitude of the wave that is measured by the camera, but the intensity, which is proportionate to the square of the amplitude. Knowing this, the intensity coefficient measured can be related to the reflected power and to the incident power, which is $R_\perp = r_\perp^2$ and $R_\parallel = r_\parallel^2$. Now, the standard equation for the degree of polarization (DOP) ρ is:

$$\rho = \frac{I_{max} - I_{min}}{I_{max} + I_{min}} \tag{4.4}$$

Here, I_{min} and I_{max} denote the minimum and maximum intensity values in the polarised images. In the experiment, $I_{min} = I_{cross\text{-}polarized}$ and $I_{max} = I_{co\text{-}polarized}$. The $I_{cross\text{-}polarized}$ is an image of an object captured when the light source (camera flash) polarizer filter oriented in 0^o angle and the camera polarizer filter oriented in 90^o, while the $I_{co\text{-}polarized}$ is when both the light source and the camera polarizer filter are oriented in 0^o angle. Another to note that $I_{cross\text{-}polarized} = I_{diffuse}$ and $I_{co\text{-}polarized} = I_{diffuse} + I_{specular}$, where $I_{diffuse}$ and $I_{specular}$ are the diffuse and specular reflectance components of the image respectively. Each object was illuminated in the camera viewing direction.

To obtain the polarization curve, the I_{min} and I_{max} in equation 4.4 need to be replaced with the Fresnel coefficients as to relate the ρ to the zenith angle θ. The new polarization model (referring from [109]) then becomes:

$$\rho = \frac{L_s \dfrac{R_\parallel(n,\theta)}{R_\perp(n,\theta) + R_\parallel(n,\theta)} + L_d \dfrac{R_\parallel(1/n,\theta) - R_\perp(1/n,\theta)}{R_\perp(1/n,\theta) + R_\parallel(1/n,\theta) - 2}}{L_d + L_s \dfrac{R_\parallel(n,\theta)}{R_\perp(n,\theta) + R_\parallel(n,\theta)}} \tag{4.5}$$

In [109], they acquired the zenith angle of the reflected light using numerical inversion of the Lambert and Torrance Sparrow models. The zenith angle is required for the calculation

of the material's ρ. For this, I used the Ma et al. [64] normal maps acquisition method. The incident and viewing angles are calculated by converting the material's estimated normal map vectors into angles using [80] conversion. Both the light source and the camera were positioned to be same. These angles are later used in the model data fitting for estimating the material's scattering parameters and also the ρ. Here, the test will be done using different materials with different properties (e.g. surface roughness and chromatic level). However, the author could not capture the human skin for this experiment. The reason is that since the setup need both the $I_{cross\text{-}polarized}$ and $I_{co\text{-}polarized}$ capture images, the author has to manually change the polarizer filter due to the limitation of the equipment. Since the skin is a non-static object, it took the author some time to change the polarizer filter and this cause the subject (volunteer) to move from its original position by a lot. As a substitute for skin, the author uses plant materials such as leaves with different conditions (e.g. green healthy leaves and old dry leaves) instead.

4.3 The correlation test between the model parameters and the material's DOP

There are sixteen samples captured for this experiment, they are: Blue Rubber Ball, Orange Plastic Ball, White Polystyrene Ball, Wood Cube, Brown Clay Teapot, Brown Cloth, Big Leaf 1, Big Leaf 2, Big Leaf Dry 1, Big Leaf Dry 2, Banana, Green Apple, Small Leaf, Small Leaf Dry, Small Leaf Hydrated and Yellow Grapefruit. Most of them are color samples with medium to rough surface and some of the leaves (the big leaves) are multilayered. In the next following subsections, we will detail the setup, results, and analysis of the test.

4.3.1 Comprehensive polarization model fitting procedure and the refractive index estimation

To obtained the material's DOP curve for the correlation test, Zhang–Hancock model [109] is used to fit to the DOP data of the material, which is first calculated using the $I_{co\text{-}polarized}$ and $I_{cross\text{-}polarized}$ (see Equation 4.4). Figure 4.1 show the DOP images of some of the samples, calculated using the green channel of the images. In Zhang–Hancock model, there are three parameters need to be considered: the two radiance L_s and L_d, and the refractive index n (see Equation 4.5). Since the total radiance is a sum of specular and

diffuse radiance $L_s + L_d = 1$, I presumed that the specular radiance $L_s = 1 - L_d$. This would decrease the unknown parameters into only two, namely the diffuse radiance L_d and the refractive index n. The fitting process is completed using the Matlab's nonlinear least square function with 25 maximum evaluation, while using the trust-region-reflective algorithm as the optimization option. The test was done on each RGB channels; using 1100 random data points with selected angles between $0^o - 75^o$. Selected data with similar angles were averaged before the normalization process. Using and exhaustive method, the search for the best-fit is done by minimizing the root-mean-squared error $\Delta_{RMS\rho}$ by varying the parameters of L_d and n. The ranges for the parameters used in the experiment are: L_d which ranges from (0 to 1) and n which range from (1 to 2.5). Here, the estimated n will later be used in the scattering model fitting test. The RMS fitting error for the ρ is given by:

$$\Delta_{RMS\rho} = 100 \times \frac{1}{K}\Big\{\sum_{k=1}^{K}[\rho_m(\theta^k) - \rho_p(\theta^k, L_d, n)]^2\Big\}^{\frac{1}{2}} \tag{4.6}$$

where ρ_m is the normalized data, ρ_p is the normalized DOP from the model prediction and k runs over the index number of the measurements used (K).

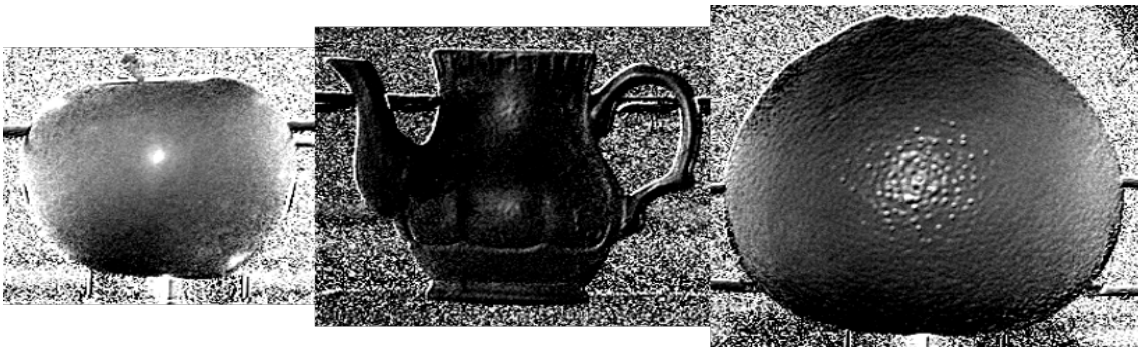

Figure 4.1: The ρ images for three samples. Start from the left: Apple; Clay Pot; and Grapefruit. Calculated using the green channel of the images.

There were several limitations when conducting the experiment. The first is that the data samples $> 75^o$ angles were not included in the test due to the high measurement error that exists on most of the collected samples. The second is that some samples have large variance measurements due to these samples having irregular shapes (e.g. the leaves and the cloth). It does not affect the accuracy of the fit of the model, but it does affect the estimation of n. Additionally, due to a high error measurement for the wood sample, resulting from human error, it was not included in the correlation test.

4.3.2 The refractive index discussion

Comparing the estimated refractive index n with the reference data, it was observed that some samples were estimated over or under the reference range values (see Table 4.2). If the lowest point of the curve decreases or increases in value, so does the estimation of n. The estimation of n using the Zhang–Hancock model can result in some discrepancies between the reference value and the estimated refractive index when dealing with rough surfaces, translucence and/or color coated materials. Most of the samples used for this experiment featured one or more of these characteristics. However, the purpose of using the Zhang–Hancock model was to determined the ρ curve of the sample.

4.3.3 The new light scattering model parameter estimation

The estimated n from the DOP model was used in the new scattering model fitting test. In circumstances where the n is not in the range of the reference, the proposed model is not particularly sensitive to the choice of the refractive index, so using the estimated values is acceptable. Additionally, for this test, the roughness parameters for the upper and lower boundaries of the scattering model are assumed identical $\sigma/T = \sigma'/T'$. Table 4.3 and 4.4 show the new model Δ_{RMS} and their estimated parameters for 15 samples (wood was excluded due to high data variance), when performed on red, green and blue channels, for both the Exponential and Gaussian variant. You will note that, based on these tables, the new Exponential model variant has a smaller average error ($\Delta_{RMS} = 0.173$) than the Gaussian one ($\Delta_{RMS} = 0.195$). Additionally, in both tables, most leaves and fruits samples obtained $\Delta_{RMS} < 0.2$, indicating that the models can estimate parameters for biological type samples quite accurately.

4.3.4 The correlation results and analysis

To prove that the parameters are able to be related to the practical measurements, the correlation test is made between the estimated parameters and the material's polarization ρ. The tests were completed at five specific angle ranges: $0^o - 15^o$, $16^o - 30^o$, $31^o - 45^o$, $46^o - 60^o$ and $61^o - 75^o$. The ρ averaged values for each of these ranges were then correlated with the estimated parameters (σ/T, β and a). The refractive index n, however, was not included in this test. Table 4.5 shows the p-values in color-coded format (e.g. p-value that is < 0.05 is the most significant), while tables 4.6 and 4.7 illustrate the correlation coefficient results for both model variants.

Table 4.2: The Refractive Index n estimation using the Comprehensive Polarization Model.

Samples	n_{ref}	n_r	n_g	n_b
Blue Rubber Ball	1.50-1.59 [67]	1.39	1.27	1.28
Orange Plastic Ball	1.49-1.50 [78]	1.05	1.08	1.30
White Polystyrene	1.55-1.59 [1]	1.47	1.38	1.34
Wood Cube	1.47-1.48 [78]	2.14	2.30	2.42
Brown Clay Teapot	1.47-1.68 [69]	1.14	1.11	1.32
Brown Cloth	1.51-1.71 [77]	1.15	1.17	1.45
Big Leaf 1	1.41-1.60 [7, 27, 107]	1.51	1.35	1.81
Big Leaf 2	1.41-1.60 [7, 27, 107]	1.12	1.02	1.29
Big Leaf Dry 1	1.41-1.60 [7, 27, 107]	1.16	1.23	1.55
Big Leaf Dry 2	1.41-1.60 [7, 27, 107]	1.15	1.16	1.35
Banana	1.41-1.60 [7, 27, 107]	1.25	1.38	1.61
Green Apple	1.41-1.60 [7, 27, 107]	1.50	1.46	1.83
Small Leaf	1.41-1.60 [7, 27, 107]	2.15	1.97	2.33
Small Leaf Dry	1.41-1.60 [7, 27, 107]	1.20	1.21	1.55
Small Leaf Hydrate	1.41-1.60 [7, 27, 107]	1.23	1.03	1.49
Yellow Grapefruit	1.41-1.60 [7, 27, 107]	1.25	1.30	1.63

Table 4.3: Estimated Parameters for the new Exponential model variant (Here the surface slope $\sigma/T = \sigma'/T'$). The rows highlighted in gray are samples that obtained $\Delta_{RMS} < 0.15$ for all color channels.

Samples	Red				Green				Blue			
	Δ_{RMS}	σ/T	β	a	Δ_{RMS}	σ/T	β	a	Δ_{RMS}	σ/T	β	a
Blue Rubber Ball	0.208	0.440	0.505	0.743	0.206	0.566	0.396	0.935	0.238	1.218	0.266	0.718
Orange Plastic Ball	0.233	1.804	0.378	0.767	0.125	0.600	0.902	0.836	0.081	0.340	0.290	0.972
White Polyester	0.176	0.471	0.384	0.718	0.172	0.486	0.323	0.783	0.161	0.493	0.287	0.821
Brown Clay Teapot	0.178	0.623	0.302	0.894	0.168	0.383	0.317	0.893	0.174	0.456	0.480	0.596
Brown Cloth	0.314	0.674	0.502	0.678	0.293	0.648	0.352	0.832	0.250	0.652	0.289	0.849
Big Leaf 1	0.152	0.470	0.380	0.782	0.286	0.430	0.495	0.789	0.180	0.507	0.251	0.901
Big Leaf 2	0.128	0.718	0.430	0.771	0.222	1.750	0.127	0.075	0.119	0.694	0.315	0.812
Big Leaf Dry 1	0.223	0.800	0.452	0.655	0.238	0.549	0.447	0.809	0.084	0.480	0.300	0.850
Big Leaf Dry 2	0.311	1.606	0.127	0.858	0.319	1.533	0.154	0.866	0.235	0.959	0.292	0.934
Banana	0.174	1.156	0.310	0.768	0.156	0.900	0.406	0.740	0.093	0.691	0.318	0.890
Green Apple	0.118	0.402	0.276	0.731	0.115	0.520	0.188	0.937	0.125	0.396	0.243	0.307
Small Leaf	0.193	0.773	0.352	0.862	0.181	0.892	0.301	0.929	0.190	0.794	0.339	0.832
Small Leaf Dry	0.164	0.983	0.361	0.664	0.146	0.672	0.396	0.758	0.150	0.634	0.292	0.712
Small Leaf Hydrate	0.057	0.712	0.432	0.617	0.091	0.834	0.477	0.471	0.109	0.764	0.286	0.452
Yellow Grapefruit	0.077	0.556	0.313	0.841	0.070	0.486	0.304	0.846	0.077	0.425	0.282	0.398

Table 4.4: Estimated Parameters for the new Gaussian model variant (Here the surface slope $\sigma/T = \sigma'/T'$). The rows highlighted in gray are samples that obtained $\Delta_{RMS} < 0.15$ for all color channels.

Samples	Red				Green				Blue			
	Δ_{RMS}	σ/T	β	a	Δ_{RMS}	σ/T	β	a	Δ_{RMS}	σ/T	β	a
Blue Rubber Ball	0.239	0.632	1.000	0.002	0.233	0.848	0.962	0.010	0.219	0.998	0.979	0.001
Orange Plastic Ball	0.218	1.466	0.757	0.005	0.097	1.773	0.857	0.047	0.062	1.497	0.802	0.896
White Polyester	0.273	0.379	0.935	0.144	0.275	0.450	0.883	0.015	0.274	0.469	0.865	0.014
Brown Clay Teapot	0.250	0.626	0.986	0.003	0.273	0.564	1.000	0.000	0.238	0.341	0.978	0.105
Brown Cloth	0.355	0.654	0.964	0.003	0.343	0.648	0.971	0.004	0.287	0.595	0.996	0.009
Big Leaf 1	0.164	0.369	0.338	0.626	0.298	0.782	1.000	0.020	0.213	0.370	0.528	0.490
Big Leaf 2	0.137	0.746	0.999	0.090	0.268	0.998	1.000	0.000	0.133	0.506	0.980	0.110
Big Leaf Dry 1	0.216	0.973	0.999	0.000	0.254	0.690	1.000	0.073	0.088	0.386	0.236	0.992
Big Leaf Dry 2	0.304	0.987	0.991	0.002	0.311	0.988	0.993	0.002	0.238	1.222	0.994	0.000
Banana	0.163	1.176	1.000	0.000	0.154	1.181	1.000	0.044	0.116	0.374	0.641	0.505
Green Apple	0.121	0.256	0.208	0.995	0.126	0.323	0.251	0.980	0.141	0.356	0.175	0.993
Small Leaf	0.200	0.386	0.792	0.411	0.184	0.364	0.543	0.626	0.193	0.346	0.725	0.439
Small Leaf Dry	0.161	0.786	0.983	0.011	0.152	0.705	0.998	0.001	0.163	0.312	0.562	0.581
Small Leaf Hydrate	0.084	0.598	0.368	0.321	0.128	0.621	0.960	0.004	0.111	0.312	0.510	0.476
Yellow Grapefruit	0.119	0.561	0.971	0.008	0.110	0.413	0.949	0.023	0.104	0.444	0.157	0.997

Table 4.5: The chosen significant level p and its strength (color coded) for two tail test.

Significant level p	$p < 0.05$	$0.05 < p < 0.1$	$0.1 < p < 0.2$
Correlation Strength	Highest significance	High significance	Medium significance

Table 4.6: Correlation between the DOP ρ and the estimated parameters for the new Exponential model variant at five specific angle range.

Parameters	$0^o - 15^o$	$16^o - 30^o$	$31^o - 45^o$	$46^o - 60^o$	$61^o - 75^o$
σ/T	-0.276	-0.267	-0.242	-0.238	-0.327
β	-0.273	-0.255	-0.214	-0.203	-0.252
a	0.068	0.071	0.075	0.075	0.091

Table 4.7: Correlation between the DOP ρ and the estimated parameters for the new Gaussian model variant at five specific angle range.

Parameters	$0^o - 15^o$	$16^o - 30^o$	$31^o - 45^o$	$46^o - 60^o$	$61^o - 75^o$
σ/T	-0.552	-0.545	-0.523	-0.523	-0.583
β	-0.469	-0.483	-0.500	-0.504	-0.543
a	0.558	0.567	0.575	0.576	0.620

In practice, surface roughness and absorption can cause depolarization to a polarized incident light. Knowing this, I would hypothesize that the model's roughness parameter σ/T should have a negative relationship with the sample's ρ value, since increasing roughness would likely depolarize polarized light even more. Meanwhile, the model's absorption, a, should have a positive relationship with the sample's ρ value, because high absorption levels would produce low diffuse radiance. Looking at tables 4.6 and 4.7, the σ/T and a demonstrate negative and positive correlation with the ρ values respectively, which supports my hypothesis. Meanwhile, regarding the correlation between β and ρ, the results obtained suggested a negative correlation, which means that as the model's lower boundary component becomes more dominant (e.g. $\beta > 0.5$), the ρ value will become lower. This result follows the diffuse polarization process state from [106], which asserts that incident light that penetrates a surface material will result in internal scattering and, later, refract back into the air, ultimately becoming partially polarized (hence lower ρ).

Looking at the correlation coefficients for both table 4.6 and table 4.7, the Gaussian variant has been shown to have more significant correlation coefficients than the Exponent variant. However, the total average root-mean-squared error Δ_{RMS} for the Gaussian

variant is higher than the Exponent variant (Exponent variant: $\Delta_{RMS} = 0.173$, Gaussian variant: $\Delta_{RMS} = 0.195$). Moreover, the histogram for the Gaussian model estimated parameters that were spread unevenly. Most parameters estimated by the Gaussian model are at the end of the estimation range; for example, most samples' a were either estimated to be ≈ 0 or ≈ 1, in which, become outliers that affect the overall correlation between the Gaussian model parameters and the ρ. The histograms for the parameters and the ρ for all samples are shown in Figure 4.2 and 4.3.

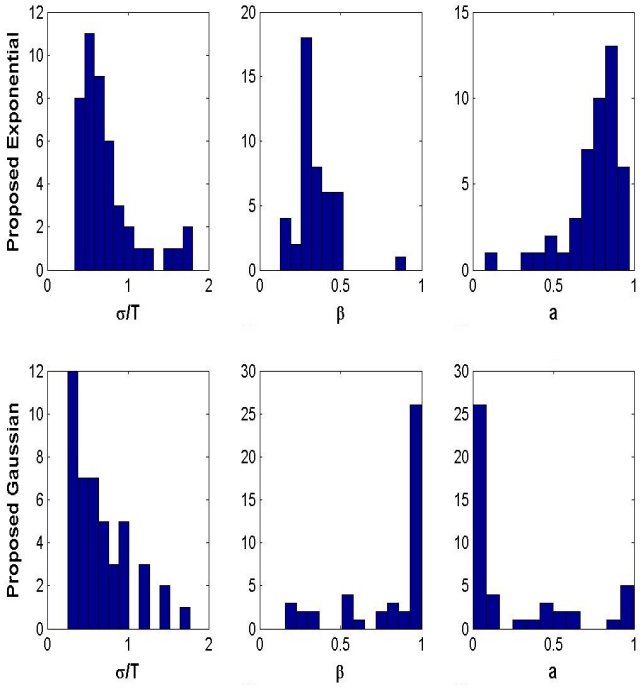

Figure 4.2: Histogram for the estimated parameters for the two new models.

Meanwhile, across the zenith angle, when the light incident is $\theta_i = 0^o$, the level of polarization should be different for the specular and diffuse components. In the experiment, the specular component should be the dominant radiance contributor near the surface normal where the radiance should be the highest, but the dominance may shift to the diffuse component as the viewing angle moves away from the right angle (e.g. surface normal). Here, the polarization of the specular component is maintained while the diffuse component becomes depolarized. Furthermore, the level of polarization ρ should be different across the angles due to the difference between the specular and diffuse components.

Tables 4.6 and 4.7 show that there are different correlation strengths across the angle. As examples, Figure 4.4-**??** show the curve for the proposed scattering model and their

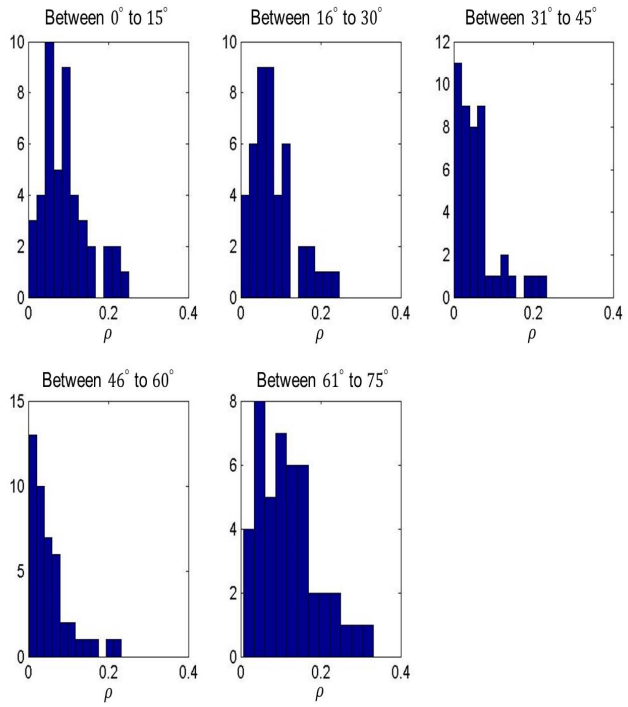

Figure 4.3: Histogram for the ρ at specific angle range (Right side).

DOP for three different samples with increasing roughness (e.g. Apple, Grapefruit and Cloth).

Note that increasing the proposed model roughness parameter σ/T would increase the curve diffuse outgoing radiance since the correlation results between σ/T and ρ are negative (see Tables 4.6 and 4.7). An increase in diffuse outgoing radiance should result in a decrease in ρ. Interestingly, evidence of this behavior did emerge from the measurement. For example, a smooth surface apple with low σ/T (small scattering of light) was shown to have higher ρ (see Figure 4.4 or 4.6 for the model curve fitting for the Exponential or Gaussian variant respectively), while a less smooth surface, like grapefruit, having σ/T than the apple (wide scattering of light) was shown to have lower ρ (see Figure 4.5 or 4.5 for the model curve fitting for the Exponential or Gaussian variant respectively). This suggests that the behavior of the model's σ/T parameter is in agreement with the surface roughness effects on the material's DOP [5, 6, 30, 37, 48, 52].

On the other hand, even though a and ρ have a positive correlation for both model variants, the correlation coefficients for the exponential variant are not significant ($p > 0.2$). Meanwhile, the Gaussian variant was shown to have a strong significant ($p < 0.05$), but the estimated parameter data histograms illustrated a mostly uneven spread and was

concentrated in specific value ranges (see Figure 4.2).

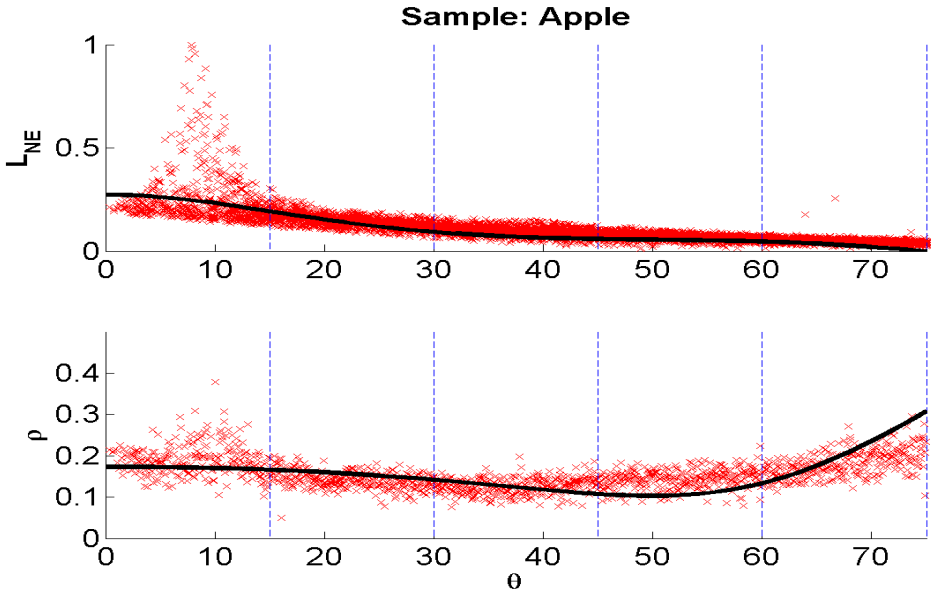

Figure 4.4: The new model curve (top) and the DOP curve (bottom) fitted on the captured data. This is for the Exponent variant done on the Red channel (Sample: Apple). $\sigma/T = 0.40$, $\beta = 0.28$, $a = 0.73$. Noted that the spike in the radiance data (top) is the specular highlight that was unable to be completely removed (measurement error).

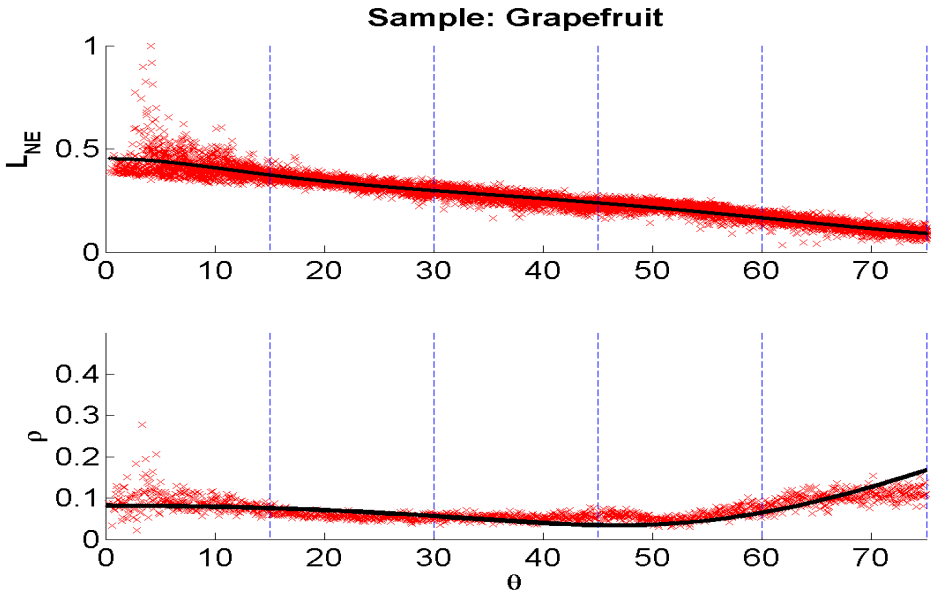

Figure 4.5: The new model curve (top) and the DOP curve (bottom) fitted on the captured data. This is for the Exponent variant done on the Red channel (Sample: Grapefruit). $\sigma/T = 0.56$, $\beta = 0.31$, $a = 0.84$.

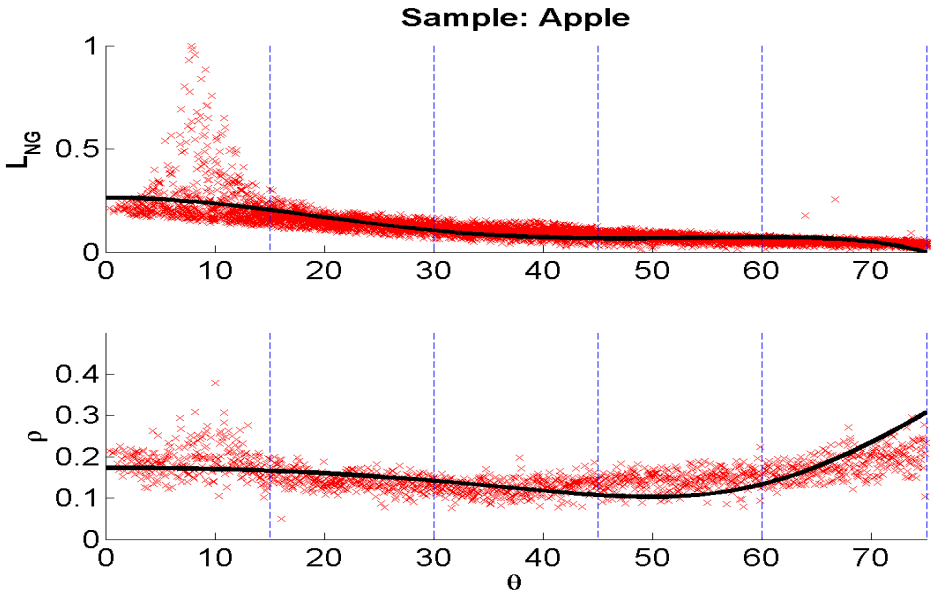

Figure 4.6: The new model curve (top) and the DOP curve (bottom) fitted on the captured data. This is for the Gaussian variant done on the Red channel (Sample: Apple). $\sigma/T = 0.26$, $\beta = 0.21$, $a = 0.99$.

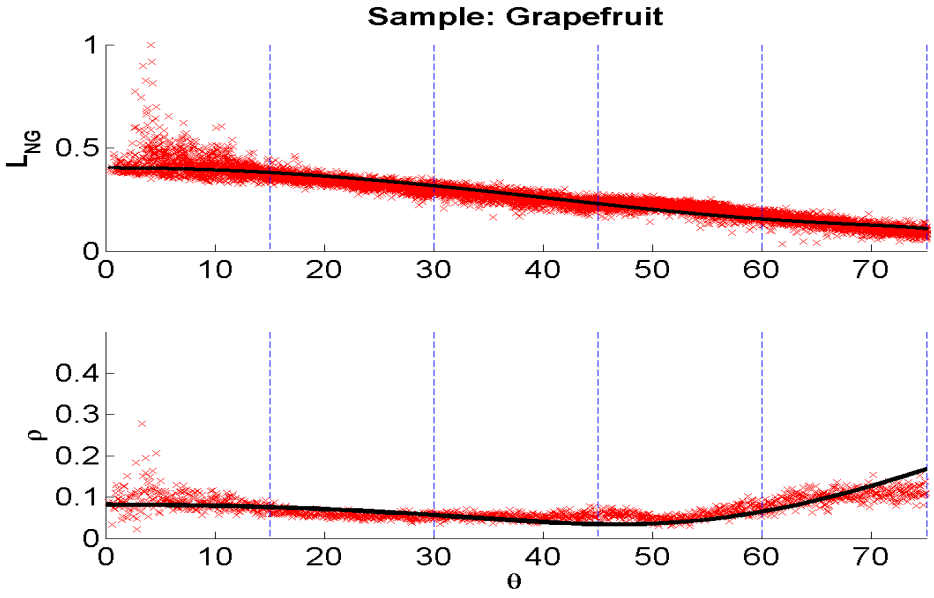

Figure 4.7: The new model curve (top) and the DOP curve (bottom) fitted on the captured data. This is for the Gaussian variant done on the Red channel (Sample: Grapefruit). $\sigma/T = 0.56$, $\beta = 0.97$, $a = 0.01$.

4.3.5 The absorption parameter analysis

There are various modes of interaction between electromagnetic radiation and matter. Each material has a particular absorption and reflection spectrum as a result of this. Furthermore, the absorption properties of a material will greatly vary over the frequency range. To study the behavior of the proposed model's absorption, I conducted an additional analysis between the plant sample estimated parameters and their physical condition, focusing only on the Exponential model variant.

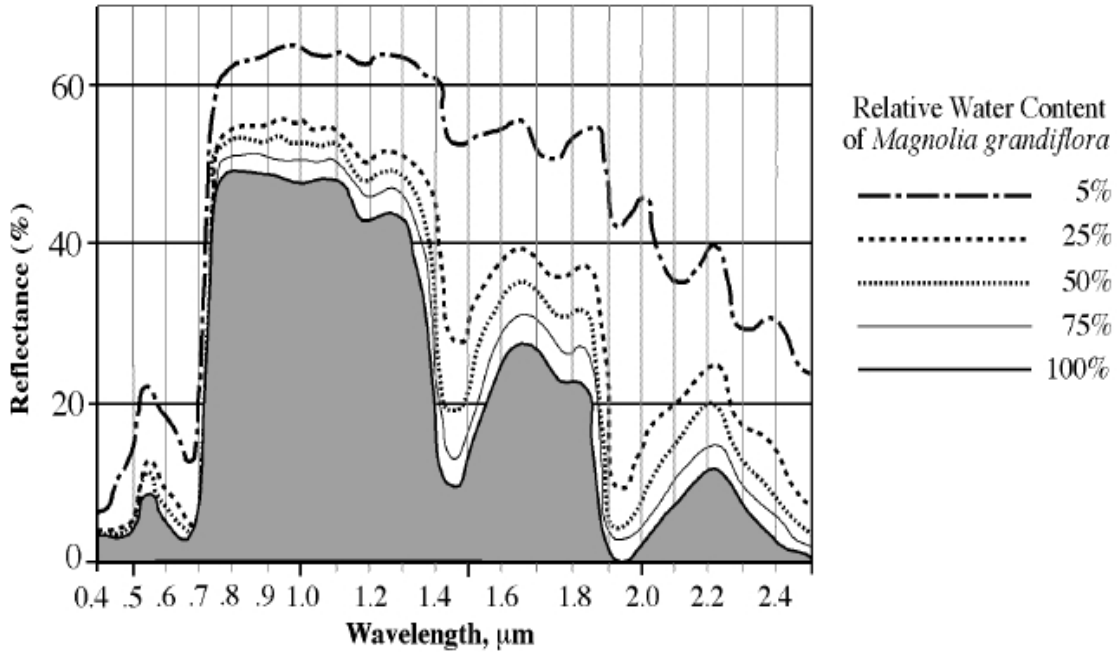

Figure 4.8: Changes in Leaf Reflectance as it Dries for Magnolia Leaf (Magnolia grandiflora). Image taken from [45]

There is an empirically established relationship between the plant optical and biochemical properties, such as the leaf response to aging or environmental stresses [32, 45, 59, 92]. Even though different species have varying concentrations of light absorbing compounds (chlorophylls, carotenoids, water, cellulose, lignin, starch, proteins, etc.), most dry plant leaves absorb less light in all visible spectrums ($400nm - 700nm$) [32, 45, 59, 92] (see Figure 4.8 as an example). In this study, I observed the estimated absorption difference between a young leaf and a dry one (for the same species).

One interesting feature that emerges from the observation (see Table 4.8) is that, for leaves of the same species, the dryer leaf has lower absorption than the young healthy one (for the Exponent variant). This was observed on the red, green and blue spectral bands.

These results support the empirically established relationship between plant reflectance and dryness detailed in [32,45,59,92]. This suggests that the a in the new model has some degree of relation (especially the Exponential variant model) to the absorption properties of organic material. However, the absorption behavior is quite different for the Big Leaf 2 and Big Leaf 2-Dry, due to their multi-layer properties.

Table 4.8: Estimated parameters for specific group of plant leaves (Exponent).

	Absorption		
Group 1	**Blue**	**Green**	**Red**
Big Leaf 1	0.901	0.789	0.782
Big Leaf 1 (Dry)	0.850	0.809	0.655
Group 2	**Blue**	**Green**	**Red**
Small Leaf	0.832	0.929	0.862
Small Leaf (Dry)	0.712	0.758	0.664
Small Leaf (Hydrate)	0.452	0.471	0.617

4.3.6 The chosen parameters for the parameter-age test

The results of this experiment regarding correlation have suggested that the new parameters of the scattering model can be related to the sample measurements and physical characteristics. The chosen parameters are the roughness parameter σ/T, the balance parameter β, and the absorption parameter a. The refractive index n was not chosen because the estimated n of the samples tend to deviate from the reference values. Other BRDF models that have similar parameter characteristics are also used for comparisons, such as the Oren-Nayar [12] model that has a roughness parameter m and the BSSRDF model [44], which includes the scattering coefficient σ_s and absorption coefficient σ_a.

4.4 The light stage setup

To obtain the necessary angle measurements from the subject's face, the diffuse normal map is captured using the Ma et al. [64] spherical gradient illumination technique and a geodesic dome light stage with LED light sources. The Ma et al. photometry method is a technique that can approximate surface normal maps by estimating it from the object's

diffuse reflectance using only a small number of gradient illumination patterns. Due to the low number of patterns, the method is suitable for real-time normal capture using time-multiplexed illumination.

In the setup, two light sources were used, namely a) ultra-bright white LEDs and b) a flash lamp. The image capture process was performed inside a geodesic dome light stage with diameter 1.58 m, with 40 filtered LEDs located at each geodesic vertex [16]. Linear polarization filters were positioned in front of each of the LEDs and also in front of the lens of the Nikon D200 camera. The light stage is controlled using an mbed NXP LPC1768 microcontroller development board. This controls the brightness of the LEDs and the camera shutter. The camera was placed at the periphery of the light stage and was manually focused. A single camera flash lamp (Nikon Speed-light SB-600) was positioned slightly above the camera, having a flash output level of 1/64 and a zoom head position value configured to 24 mm. The size of the captured image is 471×421. Figure 4.9 shows an image of the geodesic light stage used for this experiment and its diagram.

Surface reflection consists of diffuse and specular reflectance components. To separate these components, the cross-polarization method [16, 64] was used to obtain the diffuse component of the subjects. Using linearly polarized incident light (LED), the diffuse reflection was captured by placing a linear polarizer in front of the camera oriented perpendicular to the plane of incidence.

The spherical gradient photometric stereo method [64] amounts to the capturing of a sequence of images under spherical illumination conditions. When all light sources are set to a constant brightness, shading is canceled out and the surface albedo is able to be measured directly. We refer to this as the constant image, C. To capture geometry, six illumination conditions are captured wherein the brightness of each light source is linearly related to its direction from the center of the dome. The X, Y and Z images use gradient patterns wherein the illumination brightness depends on the x, y and z component of the light direction. To improve the signal to noise ratio, we also captured the complement images $\widehat{X}$, $\widehat{Y}$ and $\widehat{Z}$, wherein the gradients were inverted. Hence, with no motion, we would expect that $C = X + \widehat{X}$. In practice, we expect some small, possibly nonrigid motion to occur between frames.

To test the accuracy of Ma's spherical gradient illumination technique, several syntheses images were made from a ground truth surface normal map. For this test, the author selected the already estimated surface normal of a doll made out of fabric as a ground

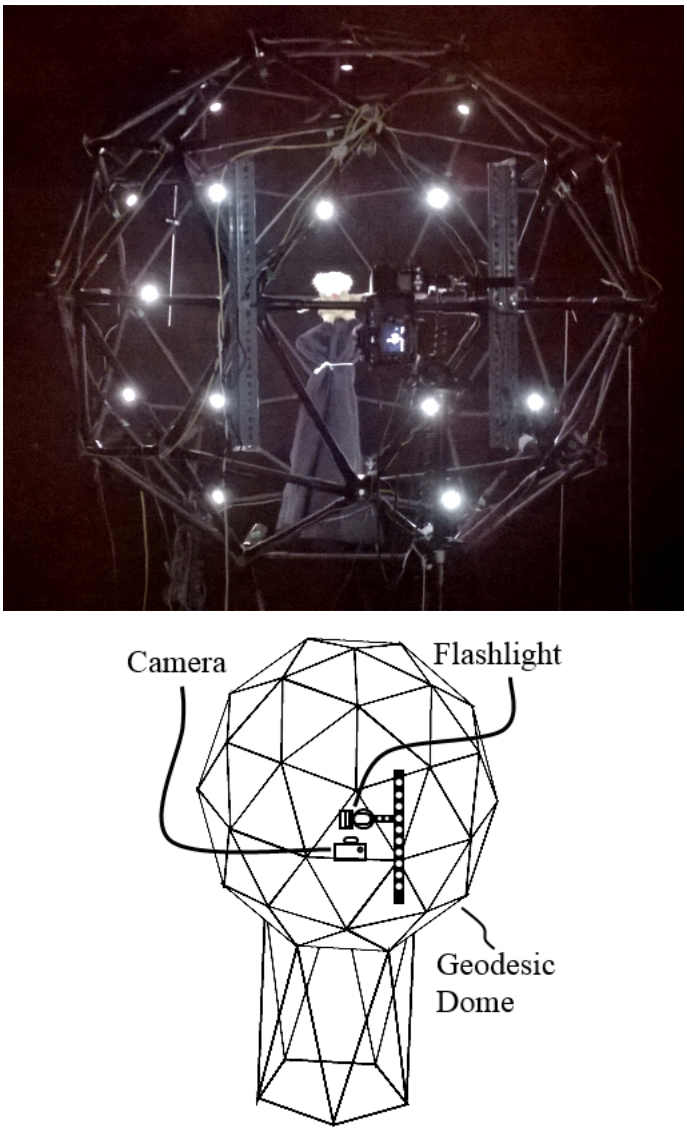

Figure 4.9: The geodesic dome light stage used in the experiment.

truth image. To create a synthesis image for the surface normal map estimation using the Mas technique, the author rendered light scattering image on the ground truth surface normal with different scale of albedo for different gradient illumination directions (X_a, $\widehat{X_a}$, Y_a, $\widehat{Y_a}$, Z_a, and $\widehat{Z_a}$). The first synthesis sample (henceforth, will be called synthesis X) is the six gradient illumination direction images with the albedo in two different X-gradient directions (X_a and $\widehat{X_a}$) are multiplied by a scale of two, while albedo for Y-gradient and Z-gradient is scale to one, so that the first group of images would be ($2X_a$, $2\widehat{X_a}$, Y_a, $\widehat{Y_a}$, Z_a, and $\widehat{Z_a}$). The surface normal map for the synthesis X samples (gradient images) will then be estimated using the Mas photometry technique and later compared with the ground truth. The author also made two more synthesis samples, which are the synthesis

Y (Y_a and $\widehat{Y_a}$ are multiply by two, while other gradients are scale to one) and synthesis Z (Z_a and $\widehat{Z_a}$ are multiplied by two, while other gradients are scale to one). To calculate the accuracy, the author selects a profile within the surface normal map and compare the geometry depth difference (z-direction) between the ground truth and the synthesis samples using the root-mean-square equation. The closer the synthesis surface normal map estimation is to the ground truth geometry depth, the lower the RMS will be. The RMS error for synthesis X, Y and Z are 19.5829, 3.6335 and 10.2996 respectively. The total average RMS is 11.1720 and the total RMS standard deviation is 8.0104. Figure 4.10 (top) shows the surface normal maps for the ground truth and the synthesis images. The yellow line indicates the location of the profile surface. Meanwhile, Figure 4.10 (bottom) shows the plot of the slice through the surface structure of Figure 4.10 (top). From the results, it is indicated that if the intensity of the gradient illumination is different for all gradient directions, it will have an impact in the surface normal map estimation accuracy when using the Mas photometry technique. It is advisable to use all light sources (i.e. the LEDs) that produce the same intensity. Nevertheless, the surface geometry for the synthesis images estimated surface normal maps is quite close to the ground truth.

In addition to the seven spherical gradient images, we also captured an additional image(s), a point flash image, that uses the camera flash as a light source. The purpose of the flash image is to be used as an image reference, which is required for the model prediction. For the experiment in Chapter 4.2, we captured two additional different flash reflectance images (co- and cross-polarized source flash). Meanwhile, Chapter 5 required the capture of just one additional cross-polarized source flash image of each subject used in the experiment. These flash images are used to estimate the degree of polarization (Chapter 4.2) and/or the light scattering model parameters (Chapter 5.1). In this section, the flash image is used to solve the problem for aligning images captured using different types of light source.

4.5 Image acquisition problem and the new image alignment method

There are two alignment problems that need to be addressed in order for our experiments to capture a non-static object. The first is that of aligning small inter-frame motions captured in the spherical gradient photometric stereo. The second is aligning inter-frame

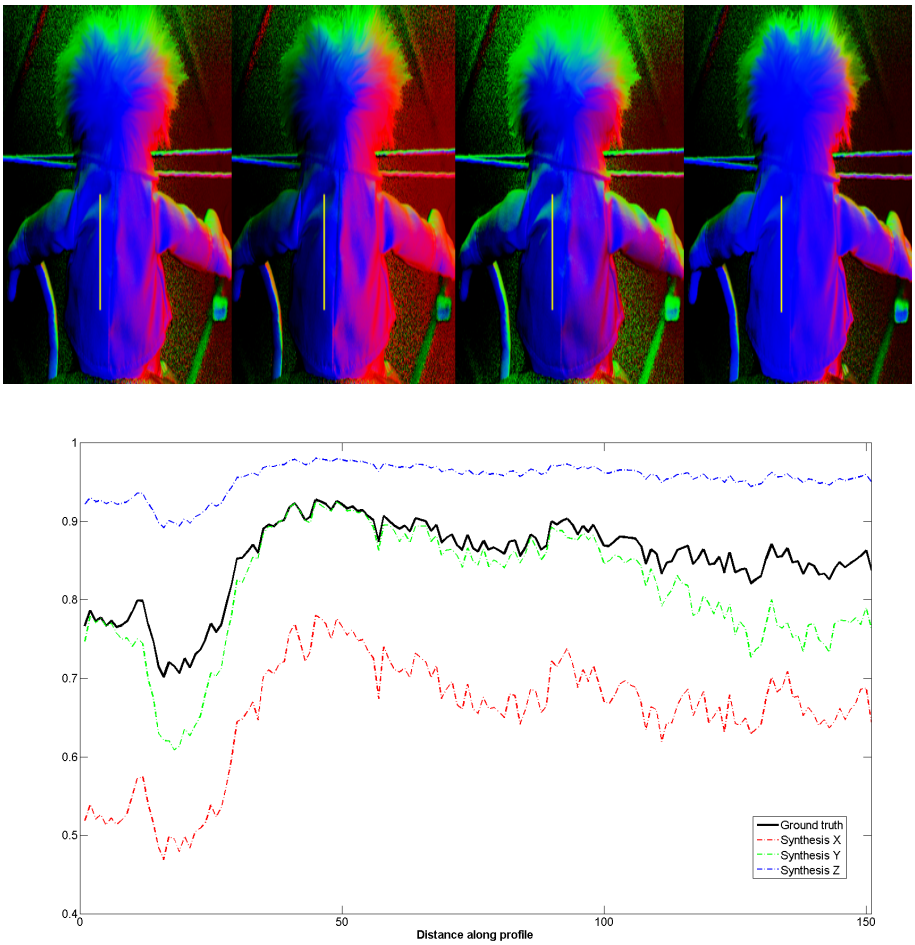

Figure 4.10: The top figure shows the surface normal maps, start from the left: the ground truth, the synthesis X, the synthesis Y and the synthesis Z. The yellow line indicates the location of the profile surface. The bottom figure shows the plot of the slice through the surface structure of the doll.

motions for photometric images captured in changing lighting conditions. The objective here is to create an alignment method that addresses these two illumination problems associated with imaging a human face that will undoubtedly make small motions throughout the process. The situation arises when a human face is being captured using different cameras and lights, and there is a gap of several seconds between the acquisition of the different images. Under these conditions the subjects face may move by several millimeters between images where the frames are captured using the spherical gradient illumination photometric stereo technique described in [64].

To tackle this obstacle, we present a reflectance-aware optical flow technique to solve some of the alignment problems for images captured in disparate illumination environ-

ments. The technique combines optical flow estimation with illumination-independent image transformation, image color transformation, and specular-invariant projection. In this section, we test the accuracy of our photometric alignment method with two problems in mind, namely (1) images captured in different lighting gradient using a single light source; and; (2) images captured using different types of light source. Here, the alignment experiment will use the seven spherical gradient images of subjects and an additional eighth image using a point source flash. The first challenge is to densely align the spherical gradient images. However, this is made easier by the fact that the properties of the illuminants are fixed. Our second challenge is to align the spherical gradient set with the flash image. This is more difficult both because the shading is unlike any of the other images and, also, because the spectral power distribution of the flash and LEDs are different, which means the image has a different color to the rest of the images. Figure 4.11 shows the entire image sequence for one sample set, while Figure 4.12 shows the overall experiment flow for testing the new alignment method.

Figure 4.11: The eight images captured in a sequence. Starting from the leftmost, the X, Y, Z, $\widehat{X}$, $\widehat{Y}$, $\widehat{Z}$ and C are the LED spherical gradient images. The rightmost image is the flash image.

4.5.1 Illumination-Independent Image

Different illumination gradients influence the image brightness constancy, which, in turn, can directly affect the optical flow calculation. Nevertheless, the spherical illumination pattern affects the intensity, but not color. Based on this observation, we mimic the approach of Seck et al. [89] by using a color-space transformation technique to extract intensity-free information from the frames, producing an illumination-independent image, I_{colour}:

$$I_{colour} = \frac{1}{2}\left(I_{hue} + \frac{I}{\sqrt{I_R^2 + I_G^2 + I_B^2}}\right) \tag{4.7}$$

where I is the captured image, and I_{hue} is the hue component of the Hue-Saturation-Value (HSV) space; I_R , I_G and I_B are respectively the red, green and blue image channels.

Optical flow methods [60] are sufficient for correcting any small motion misalignment. To align the images, Seck et al. [89] modified the Wilson et al. [105] iterative optical flow approach which can be used to solve the issues associated with both the gradient and its complement images. Assuming that there is no motion, the sum of a gradient image and its complement are equal to the constant image. For example, let the x-gradient images be:

$$C(x, y) = X(x_1 + \Delta x_1, y_1 + \Delta y_1) + \widehat{X}(x_2 + \Delta x_2, y_2 + \Delta y_2) \tag{4.8}$$

Wilson et al. [105] initially computed the flow from X to $C - \widehat{X}$ followed by the flow from $\widehat{X}$ to $C - w(X)$, where w is the warp computed at the previous step. However, by using the equation 4.7, we were able to use the flow between C_{colour} and $\widehat{X}_{colour}$ to align

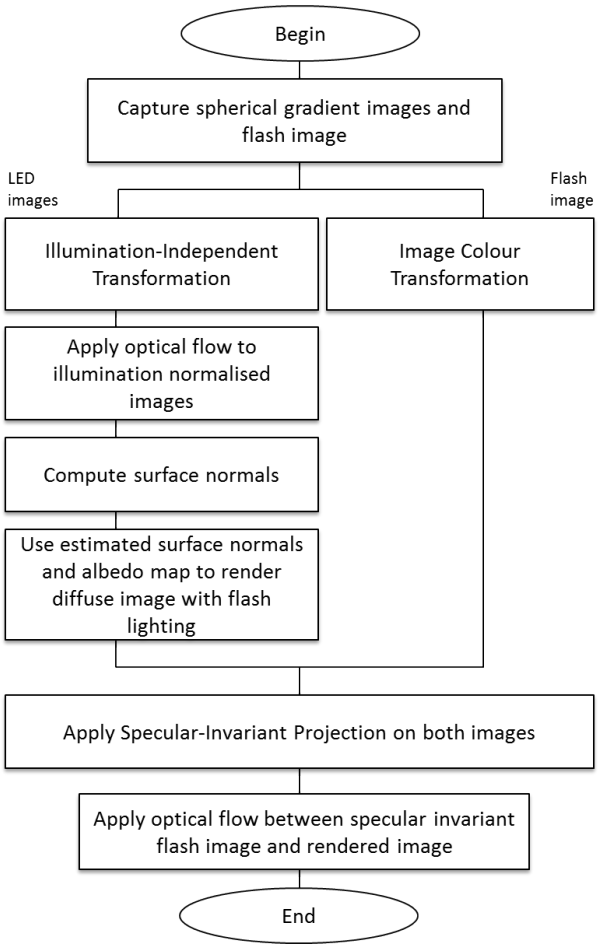

Figure 4.12: The process flow of the new alignment method.

C and $\widehat{X}$ before computing $C - \widehat{X}$. Figure 4.13 shows two gradient images and their illumination-independent transformation.

Figure 4.13: Two images in different spherical gradient lighting patterns (top) and their corresponding illumination-independent images (bottom). The left column is the X Gradient image and the right column is its complement image.

From the aligned spherical gradient images, we can compute per-pixel surface normal estimates and the diffuse albedo [105]. We then use these to render a diffuse image with a point light source in the same direction as the flash. This provides a target image to which we can align the flash image.

4.5.2 Image Color Transformation

Before aligning the flash image to the rendered image, we begin by compensating for the color transformation caused by the different light sources. We assume that the two color

spaces can be related by an affine transformation:

$$I_{LED}(x,y) = \overline{T} I_{Flash}(x,y) + \overrightarrow{c} \tag{4.9}$$

where $I_{LED}(x,y)$ and $I_{Flash}(x,y)$ are LED and flash RGB reference images respectively, having the size of 3×1. Meanwhile, $\overline{T}$ is a 3×3 transformation matrix, and $\overrightarrow{c}$ is a 3×1 vector of offsets. To obtain $\overline{T}$ and $\overrightarrow{c}$, we first acquire reference images of a color checker chart illuminated by each light source. We averaged each of the 24 color squares from the flash and LED chart images and used them to form a 72×12 matrix $\overline{F}$ and 72×1 vector $\overrightarrow{L}$, respectively. The matrix form for $\overline{F}$ is:

$$\overline{A}_i = \begin{bmatrix} r_i & g_i & b_i \\ 0 & 0 & 0 \\ 0 & 0 & 0 \end{bmatrix} \overline{B}_i = \begin{bmatrix} 0 & 0 & 0 \\ r_i & g_i & b_i \\ 0 & 0 & 0 \end{bmatrix}$$

$$\overline{C}_i = \begin{bmatrix} 0 & 0 & 0 \\ 0 & 0 & 0 \\ r_i & g_i & b_i \end{bmatrix} \overline{F} = \begin{bmatrix} \overline{A}_1 & \overline{B}_1 & \overline{C}_1 & \overline{Id} \\ & \vdots & \vdots & \\ \overline{A}_{72} & \overline{B}_{72} & \overline{C}_{72} & \overline{Id} \end{bmatrix} \tag{4.10}$$

where $\overline{Id}$ is an 3×3 identity matrix and (r_i, g_i, b_i) is the color of the ith color checker square in the flash image. $\overrightarrow{L}$ is given by:

$$\overrightarrow{L} = \begin{bmatrix} R_1 & G_1 & B_1 & R_2 & \dots & B_{72} \end{bmatrix} \tag{4.11}$$

where (R_i, G_i, B_i) is the color of the ith color checker square in the LED image.

We express the affine relationship as

$$\overline{F}\,\overrightarrow{v} = \overrightarrow{L} \tag{4.12}$$

and solve in a least squares sense for the 12×1 vector $\overrightarrow{v}$ containing $\overline{T}$ and $\overrightarrow{c}$:

$$\overrightarrow{v} = \begin{bmatrix} \overline{T}_{11} & \overline{T}_{12} & \overline{T}_{13} & \overline{T}_{21} & \dots & \overline{T}_{33} & \overrightarrow{c}_1 & \overrightarrow{c}_2 & \overrightarrow{c}_3 \end{bmatrix}. \tag{4.13}$$

4.5.3 Projection into Specular Invariant Space

After color correction, we expect that the flash image and the rendered image will differ only as a result of the specular reflections that are included in the flash image, while they are not in the rendered image. For this reason, we project into a specular invariant space as proposed by Zickler et al. [111], producing a dichromatic specular invariant image. This is done by linearly transforming the RGB coordinate system by rotating one of its axes

(in this case, blue **B**) to align in the direction of the source vector **s**. This transformation defines a new color space referred to as the SUV color space [111]. It is defined according to $\mathbf{e}_{SUV} = \mathbf{B}\mathbf{e}_{RGB}$ using any $\mathbf{B} \in SO(3)$ that must satisfy $\mathbf{Bs} = (0, 0, 1)$. With the neutral interface assumption, the observation of a surface point can now become:

$$\mathbf{e}_{SUV} = \bar{\mathbf{d}}\phi_d + \bar{\mathbf{s}}\phi_s \tag{4.14}$$

with,

$$\bar{\mathbf{d}} = \mathbf{Bd} \quad and \quad \bar{\mathbf{s}} = \mathbf{Bs} = (0, 0, 1). \tag{4.15}$$

The S channel can be uniquely defined for a given s, while U and V channels can be arbitrarily chosen from the family of orthonormal bases for the plane orthogonal to s. The S channel encodes the entire specular component while the U and V diffuse channels are independent of ϕ_s and, therefore, become specular invariant [111]. As a consequence of linear transformation, when $\mathbf{r}_i^T$ denotes the ith row of **B**, the values of the two diffuse channels then satisfy:

$$e_U = \mathbf{r}_1^T \mathbf{d}\phi_d \quad and \quad e_V = \mathbf{r}_2^T \mathbf{d}\phi_d. \tag{4.16}$$

The dichromatic specular invariant projection image can now be produced using the equation 4.16 to get a two-channel color vector $\mathbf{j} = (e_U, e_V)$.

4.5.4 The image alignment test

In this experiment, we conducted two alignment tests to address two separate illumination problems. The first problem we considered was that frames captured in different spherical gradient illumination needed to be aligned, while the second one is that frames captured using two different light sources needed to be aligned. For the first test, we conducted alignment error calculations between two gradient images (e.g. Figure 4.14). The pixel alignment error is calculated based on the difference of pixel brightness, where the equation is given by:

$$E_P = \frac{\left| X_P - \widehat{X}_P \right|}{\widehat{X}_P} \times 100 \begin{cases} \text{if } E_P \geq 15\% \text{ then } Count_P = 1 \\ \text{if } E_P < 15\% \text{ then } Count_P = 0 \end{cases} \tag{4.17}$$

where here, P is the pixel location at row i and column j. We assume an acceptable pixel alignment error to be below the threshold of 15%. The overall alignment error between the two frames is given by:

$$E_{Align} = \frac{\sum_{n=1}^{\infty} Count_n}{n} \tag{4.18}$$

To observe the accuracy of the method, we aligned the transformed complement gradient images by rotating it at a certain degree or by increasing its brightness at a certain scale. The results are shown in Table 4.9 and Table 4.10. Note that for the brightness test, we used the complement image rotated at 8^o clockwise.

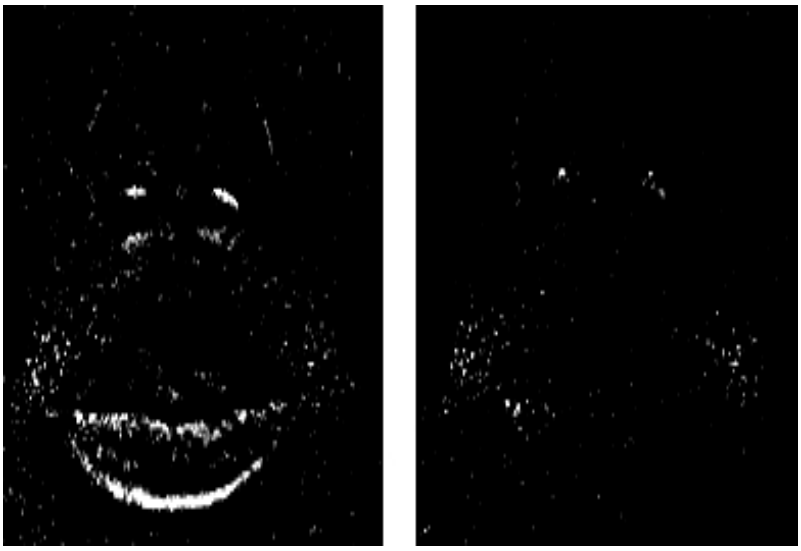

Figure 4.14: Alignment error difference for two different frames (Constant and X-Gradient) at the nose and mouth; before (left) and after (right) alignment. The nose and mouth outline is visible for the left image compares to the right one.

Table 4.9: Alignment error for different rotation r of the complement image (clockwise)

		Rotation Degree 'r'										
Sample		0^o	4^o	8^o	12^o	16^o	20^o	24^o	28^o	32^o	36^o	40^o
$X_1 - \widehat{X}_{r1}$	μ	0.0704	0.0684	0.0700	0.0715	0.0744	0.0803	0.1000	0.1300	0.1532	0.1541	0.1593
	σ	0.2558	0.2524	0.2552	0.2576	0.2625	0.2718	0.3000	0.3363	0.3602	0.3611	0.3660
$Y_1 - \widehat{Y}_{r1}$	μ	0.0806	0.0807	0.0808	0.0809	0.0845	0.0849	0.1184	0.1368	0.1849	0.2107	0.2011
	σ	0.2722	0.2724	0.2725	0.2727	0.2781	0.2787	0.3231	0.3437	0.3882	0.4077	0.4008
$Z_1 - \widehat{Z}_{r1}$	μ	0.0739	0.0712	0.0715	0.0750	0.0741	0.0915	0.0998	0.1249	0.1583	0.1634	0.1513
	σ	0.2616	0.2571	0.2576	0.2634	0.2619	0.2883	0.2997	0.3306	0.3650	0.3697	0.3583
$X_2 - \widehat{X}_{r2}$	μ	0.0256	0.0241	0.0236	0.0242	0.0372	0.0416	0.0460	0.0512	0.0526	0.0716	0.0670
	σ	0.1579	0.1535	0.1518	0.1538	0.1894	0.1996	0.2096	0.2204	0.2232	0.2579	0.2500
$Y_2 - \widehat{Y}_{r2}$	μ	0.0287	0.0276	0.0275	0.0291	0.0340	0.0416	0.0456	0.0631	0.0710	0.0842	0.0884
	σ	0.1670	0.1638	0.1636	0.1680	0.1812	0.1996	0.2087	0.2431	0.2568	0.2777	0.2838
$Z_2 - \widehat{Z}_{r2}$	μ	0.0356	0.0329	0.0327	0.0354	0.0362	0.0389	0.0567	0.0628	0.0769	0.0768	0.0889
	σ	0.1854	0.1784	0.1779	0.1847	0.1867	0.1933	0.2313	0.2427	0.2665	0.2663	0.2846

In practice, the alignment of the LED images provides good results with just one

Table 4.10: Alignment error for different brightness scale b of the complement image rotated at 8^o clockwise

		Brightness scale						
Sample		1.05	1.10	1.15	1.20	1.25	1.30	1.35
$X_1 - \widehat{X}_{b1}$	μ	0.0705	0.0707	0.0711	0.0855	0.1128	0.1188	0.1191
	σ	0.2560	0.2563	0.2570	0.2796	0.3163	0.3236	0.3239
$Y_1 - \widehat{Y}_{b1}$	μ	0.0806	0.0809	0.0810	0.0819	0.0825	0.0837	0.0862
	σ	0.2723	0.2727	0.2729	0.2742	0.2752	0.2770	0.2807
$Z_1 - \widehat{Z}_{b1}$	μ	0.0807	0.0762	0.0797	0.0906	0.0867	0.0855	0.0821
	σ	0.2723	0.2652	0.2708	0.2870	0.2814	0.2797	0.2745
$X_2 - \widehat{X}_{b2}$	μ	0.0239	0.0240	0.0268	0.0243	0.0306	0.0407	0.0481
	σ	0.1528	0.1532	0.1616	0.1539	0.1722	0.1976	0.2139
$Y_2 - \widehat{Y}_{b2}$	μ	0.0274	0.0275	0.0276	0.0275	0.0276	0.0277	0.0275
	σ	0.1634	0.1635	0.1640	0.1636	0.1637	0.1640	0.1635
$Z_2 - \widehat{Z}_{b2}$	μ	0.0340	0.0351	0.0433	0.0455	0.0436	0.0426	0.0486
	σ	0.1811	0.1841	0.2034	0.2083	0.2043	0.2020	0.2150

iteration after initialization. Tables 4.9 and 4.10 show that as the rotation or brightness increases, so does the mean error and its standard deviation. Visible misalignment at a certain region of the face start to occur as the rotation degree reach $\geq 12^o$ or the brightness scale > 1.2. So, good alignment should not exceed this threshold when using this alignment method if the first problem outlined above is to be managed.

Regarding the second problem of aligning the spherical gradient set with the flash image, the projection to the specular invariant space is applied to both the color-corrected flash image and the rendered image. Hence, we finally obtain a pair of specular invariant, two channel images which (neglecting noise) differ only by a global scaling. We compute an approximate global scale using the unaligned images and finally apply optical flow to compute the dense alignment. In practice, attenuation of the flash light means that the boundary of the face is much darker than predicted by our rendering. Moreover, due to the different intensity distributions between the rendered and the flash dichromatic images, the intensity distribution was still large enough to cause the optical flow to miscalculate

even after scaling was applied to these images. These are the main sources of error in our alignment for the flash image.

4.5.5 Discussion on the image alignment test

Due to limitations resulting from the available equipment, it was difficult to calibrate both the LEDs and the camera flash to produce the closest attenuation effect. The illumination-independent transformation failed when applied to the flash image because of the attenuation difference. Moreover, the transformation cannot be applied to the dichromatic images since all three channels are required to calculate the image's HSV. Figure 4.15 shows the illumination-independent images obtained for the LED and the flash images (after color transformation); the differences between the two are quite apparent.

Figure 4.15: Two illumination-independent images. The left is the LED image (constant gradient) and the right is the transformed color flash image.

In the second alignment test, we did not achieve good result for two reasons. Firstly, the shadow forming on the sides of the face of the flash image contributed to the alignment error. Using a rendered image mimicked the flash image aesthetically, but did not improve the performance. Secondly, even after applying the specular invariant projection technique and the scaling on both the flash image and the rendered images (Figure 4.16), their pixel intensity histogram distributions remained quite different. This resulted in inaccurate movement flow estimation due to the attenuation problem. As an alternative for aligning flash image for the experiment detailed in Chapter 5.1, the extrapolation technique was used instead.

Figure 4.16: The dichromatic images. The left is the flash image version while the right is the rendered version.

4.6 Summary

The correlation test between the material's DOP and the new model parameters suggest that the new scattering model's parameters can be related to the sample's practical characteristics. The chosen parameters that will be used in the next experiment (Chapter 5.1) are the roughness σ/T, the balance parameter β and the absorption a. Moreover, the results from Table 4.3 and 4.4, have shown that the model parameter estimation of leaves and fruits samples obtained $\Delta_{RMS} < 0.2$, indicating that the new models can be used to estimate parameters for biological type samples quite accurately. This is important when trying to estimate the skin parameters for different aging skin for the purpose of statistical analysis.

For the image capturing process, we introduced a reflectance aware optical flow method for aligning photometric images with different lighting environment. It was observed to provide good alignment results for frames captured in different gradient illumination, but failed to align the frames captured with changing light source. Nevertheless, the method is novel and can be improved. Some of the future improvements or alternatives to be considered for the second illumination problem are: 1) Capturing the subject's diffuse component for the flash image using the polarizer. By doing this, the specular invariant projection process can be skipped. However, the polarizer for the camera flash needs to be adjusted manually and the light attenuation problem between the flash and LED image still

remains. 2) Using a controllable light source so that the light can be calibrated to give the appropriate brightness. Still, this results in the creation of a control lighting environment which negates the purpose of the proposed method. 3) Focus on designing an algorithm to handle the attenuation problem between the two images or replace the proposed flash image alignment with an extrapolation technique. Additionally, as an alternative to the linear polarized spherical illumination method, the proposed alignment technique might also work if the circular polarized method advanced by Ghosh et al. [29] was chosen instead. In summary, refinements of the proposed method may assist in image alignment and photometry where they are being used in an uncontrollable lighting environment.

Chapter 5

The relation between the model parameters and the subject age

This chapter will outline the study undertaken for this thesis, which is studying the relationship between the parameters of a light scattering model and skin from subjects of various ages (henceforward, referred to as the parameter-age test). The main objective of this study is to analyze whether the parameters of statistic-based Bidirectional Reflectance Distribution Function (BRDF) models can be used to distinguish between skin of differing ages. This is done by fitting the models under study (i.e. the new model and other selected BRDF models) to the subject's radiance measurements, by varying the model parameters to minimize the root-mean-squared error and, later, correlating the parameters with the subjects ages. The sections contained in this chapter provide details regarding how the data was collected and organized, the methodology of the experiment, the test results, an analysis of the parameter-age relationship, and a discussion of the findings.

5.1 The data collection and organization

The subjects in this experiment were volunteers, all of whom had freely provided their consent. The candidates were categorized based on their skin types using the Fitzpatrick labeling method, which is a skin classification base on the amount melanin pigment in the skin [23]. This is determined by constitutional colour (white, brown or black skin) and the result of exposure to ultraviolet radiation (tanning). The scale start from the pale or white skin classify as number 1 and increases in number as the skin gets darker (the darkest skin is classify as number 6). Pale or white skin burns easily and tans slowly and poorly, while

darker skin burns less and tans more easily. Table 5.1 shows the candidate pool grouped based on their gender and skin type. Two measurements were taken from each subject; the normal map and a single diffuse reflectance image, which acts as a reference image for the model fitting. The normal map was acquired using the Ma et al. spherical gradient illumination method [64], while the diffuse reflectance image was captured using a single flash camera fitted with a cross-polarizer filter. The image was captured in the .tiff format with the size being 3900×2616, however, for the purpose of processing the image, it was resized to 1/4 (or 975×654) of its original size using the bicubic interpolation method. The scaled down image reduces the time required for the image alignment process. The author has noted that reducing the image size will degrade the image quality to some extent due to the down-sampling process, which will affect the appearance quality of the aging features that are on the facial image. See Chapter 4.4 for more detail regarding the image acquisition setup.

Table 5.1: The candidates used for the parameter-age test

Group by gender					
Age Group	19-29	30-39	40-49	50 >	Total
All Male	9	7	1	6	23
All Female	14	6	4	1	25
				Overall Total	48
Group by skin type (using the Fitzpatrick labeling method [23])					
Skin Type	Male	Male with Cream	Female	Female with Make up / Cream	Total
2	4	0	2	3	9
3	9	1	3	5	18
4	6	0	6	6	18
5	2	1	0	0	3
				Overall Total	48

It is also noted that most of the candidates are people who work indoors, so the data collected is limited in this respect. Nevertheless, different skin properties can and do still occur for each individual due to other effects, such as genetics (internal force) or skin injury (external force) [25,84,87]. Additionally, there are a higher proportion of candidates below the age of 29 within the sample used in this experiment. This is because most of these volunteers are acquainted with the author of this thesis. Table 5.1 illustrate that the volunteer quantity decreases as the age group increases. That said, there are a number of

male volunteers above the age 50 who have been included within the sample. The reason is that most of these volunteers who kindly agreed to help were staff who work in the same department as the author. Figure 5.1 shows some of the volunteers captured using the camera flash fitted with a linear polarization filter.

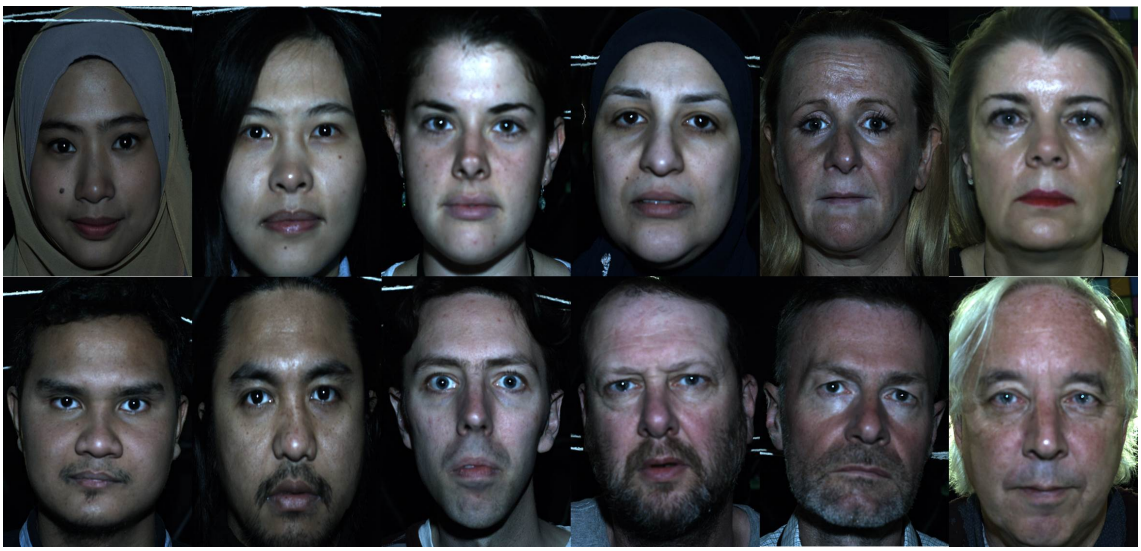

Figure 5.1: Several images of volunteer used in this experiment.

There were some volunteers who were wearing makeup (or facial cream) when the image of them was captured. It should be noted that the cosmetics do likely affect the light scatter on the skin. More than half of the women in the dataset were wearing cosmetics when the image of them was captured. In the experiment, these volunteers are included in the test to observe how would the cosmetics affect the estimation value of the model parameter(s). The dataset also includes volunteers from a variety of ethnic backgrounds, namely: Malaysian = 22; English = 11; Chinese = 5; Turkish = 2; Indian = 1; Welsh = 1; Maldovian = 1; Arabic = 1; White Asian = 1; Irish = 1; Russian = 1; and American = 1. It should be noted that different ethnic backgrounds usually result in different facial structures and skin and that the process of chronological aging is likely to differ between those from different ethnic backgrounds [8, 58, 65, 68, 85, 90, 94, 100]. This turn, this will affect the light scatter on their facial skin. The author was not able to get an evenly distributed race in the dataset, due to the author respecting the candidates' right to privacy.

One of the limitations resulting from this dataset is that it collected different subjects with different age, not subjects capture in progressing age. The affirmation correlation of

the results of the experiment regarding the relationship between the model parameter and the subject age would be much stronger if similar subjects were captured across a coherent and progressive age range. This would help to confirm that the model parameter does change as a result of aging. However, to obtain data from a single subject in consecutive years is time consuming and costly to both the subject and the researcher. Moreover, the volunteer's skin condition must also be taken into consideration. A subject who works outdoors in the sun would have age more across one or two years than a subject who work indoors, due to external forces, such as photoaging, which is a skin damage caused by prolonged sun exposure. Furthermore, the changes resulting from external forces can be slow for subjects who work indoors and it may take five years for some changes or additional aging features to appear on their faces (It should be noted that this is true only for the sample within the adult to senior stage). As such, the experiment will proceed based on the data collected from the current sample.

5.2 The experiment methodology and results

After the images of the front of the subject face had been captured, they were cropped into four different sections, namely the forehead, the left cheek, the right cheek, and the nose. The reason for this is that different facial sections have different facial structures and skin properties, which will, in turn, produce differing radiance intensities. In this experiment, the radiance from each area was averaged across the angles. Here, only the data at $0^o - 70^o$ angles were used because the data at angles $> 70^o$ produce high radiance variances that can contribute to model fitting error.

This parameter-age test is done using all of the candidates collected. To estimate the parameter(s), the selected models are fit to the captured radiance data. This was done by varying the model parameters in an effort to minimize the root-mean-square error Δ_{RMS} (see Equation 3.16). For the new model variants (Exponential and Gaussian), the initial estimation range for the new model RMS slope σ/T are between (0.01 to 2.00), while the absorption a - range between (0 to 1). Meanwhile, for the Ragheb–Hancock (R–H) models, σ/T is between (0.01 to 4.00). The balance parameter β for both the new and R–H models are made within the range of (0.01 to 1.00). It should be noted that in this test, for both new and R–H models, the RMS slope for the surface and the subsurface are identical $\sigma/T = \sigma'/T'$. As for the Oren–Nayar model, the roughness parameter m is measured in degrees, so the range of estimation is between (0^o to 180^o); while the albedo

ρ_{ON} is within (0 to 1). The BSSRDF model scattering σ_s and absorption σ_a coefficients were also estimated to be between (0 to 1). Meanwhile, each model has a coefficient k_{model}, the range for them being between (0 to 1). It should be noted that the relevant equations have already been described in chapter 3.

The estimations are completed using 1000 selected sample points, using Matlab's least squared function with maximum function evaluation set to 55. After the initial fitting process, the samples are fitted to the model again, but with smaller and more specific estimation ranges for the parameters. This is done in an effort to decrease large variation within the initial estimation. The process is completed several times until it reaches the least total Δ_{RMS} and the least possible variation. After the final estimation, the relationship between the parameters and the subject age can be analyzed. The analysis consisted of the calculation of the correlation coefficient for the selected parameters, with any values that have $p < 0.05$ being highlighted.

To demonstrate the accuracy of the models, Figure 5.2 shows the Δ_{RMS} histogram of all the data, including all of the color channels and all of the face sections for all six different models. Meanwhile, Figure 5.3 illustrates the fitting plot for one subject on six different models. The subjects used in this experiment possessed a wide variety of facial features as a result of varying gender, skin type, cosmetic use and facial structure. Figures 5.4 to 5.9 show the plots for the subject age against the estimated parameters for each of the six models, on each RGB channel. The experiment used all 48 subjects; including all facial sections. The points in the plots are the estimated model parameters. The dotted line is the regression line. Meanwhile, Tables 5.2 - 5.4 show the two-tailed correlation coefficient results between each model parameters and the subject age.

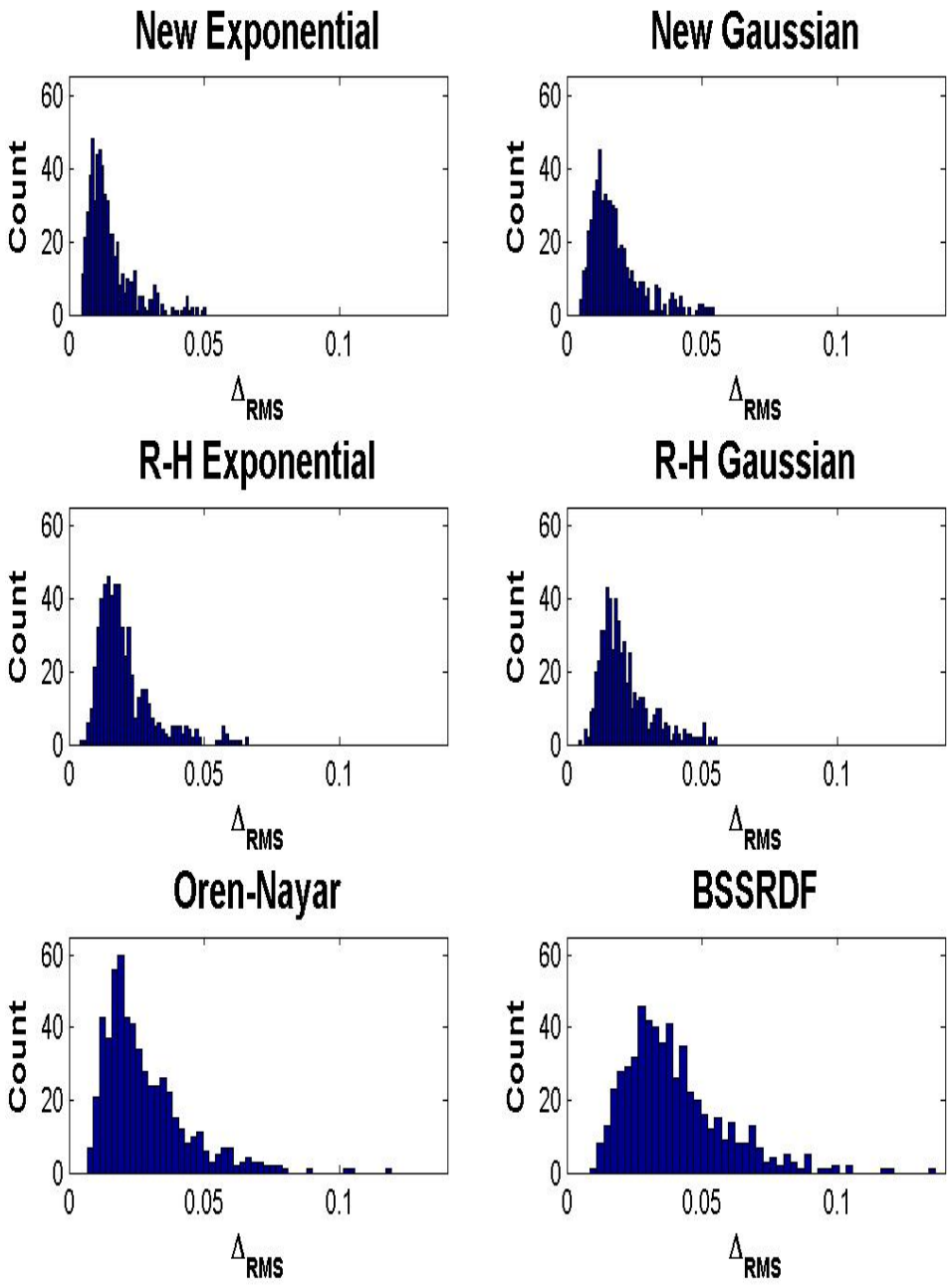

Figure 5.2: The root-mean-square error RMS_{Δ} histogram for the models using all 48 samples (including all facial region).

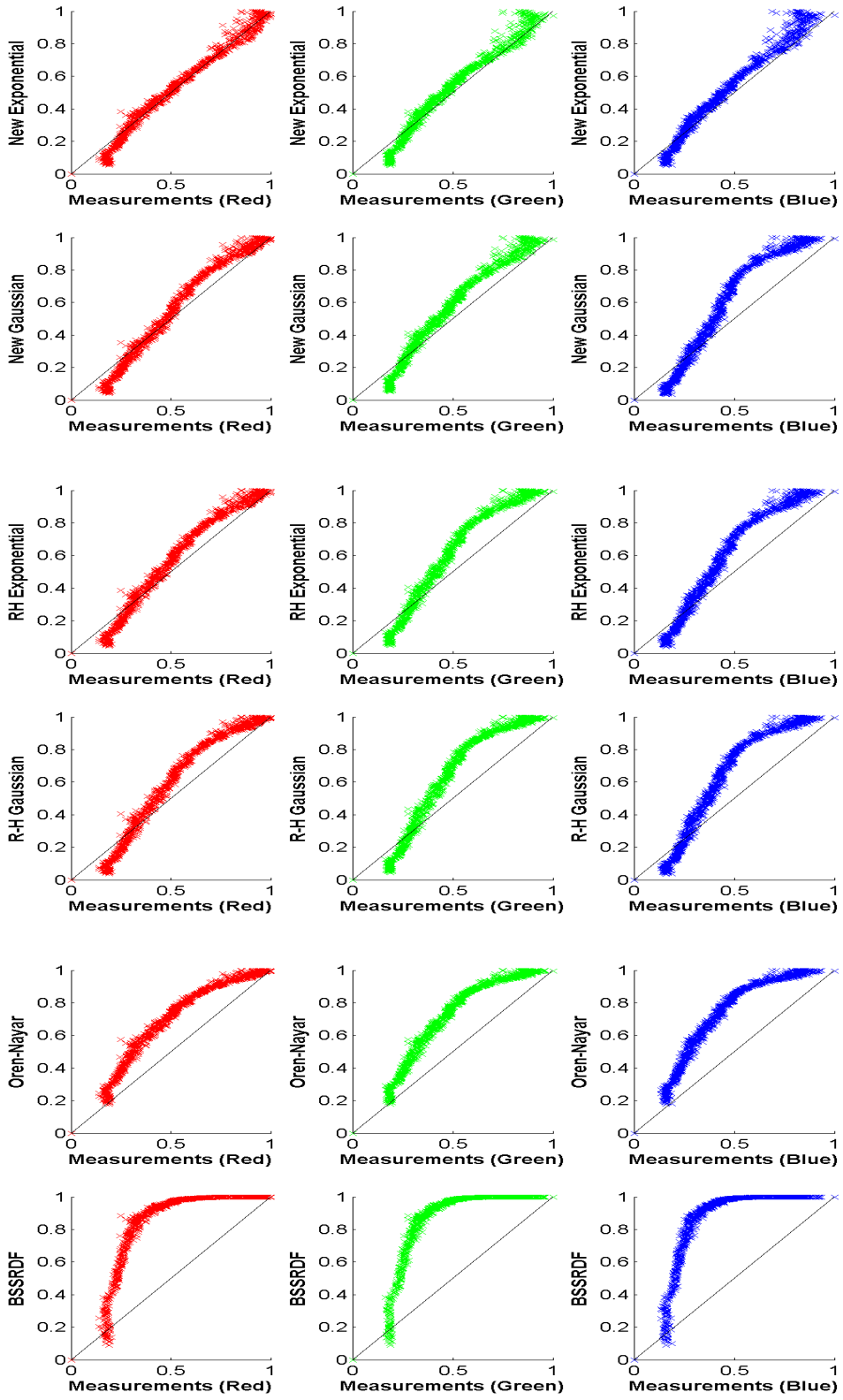

Figure 5.3: Normalized data measurements against the normalized radiance prediction (Subject: Male, Age: 35, Skin Type: 2, Cosmetic: None).

Table 5.2: Correlation coefficients between the parameter and the subject age for the New model using all samples. (White cell $p < 0.05$; Grey cell: $p > 0.2$)

Model	Parameter	R	G	B
New Exponential	σ/T	0.2146	0.2309	0.1555
	β	0.0044	-0.0785	-0.0724
	a	0.1924	0.2781	0.1758
New Gaussian	σ/T	0.2405	0.2434	0.1662
	β	0.2637	0.3083	0.2231
	a	0.0651	-0.0494	0.0379

Table 5.3: Correlation coefficients between the parameter and the subject age for the R–H model using all samples. (White cell $p < 0.05$; Grey cell: $0.1 < p < 0.2$)

Model	Parameter	R	G	B
R–H Exponential	σ/T	0.3948	0.3518	0.3010
	β	0.2575	0.2365	0.2695
R–H Gaussian	σ/T	0.3156	0.3104	0.2489
	β	0.1405	0.1558	0.1201

Table 5.4: Correlation coefficients between the parameter and the subject age for the Oren–Nayar and BSSRDF models using all samples. (White cell $p < 0.05$; Grey cell: $0.1 < p < 0.2$)

Model	Parameter	R	G	B
Oren–Nayar	m	0.2578	0.2977	0.1936
BSSRDF	σ_s	0.1718	0.1633	0.1320
	σ_a	-0.1718	-0.1634	-0.1320

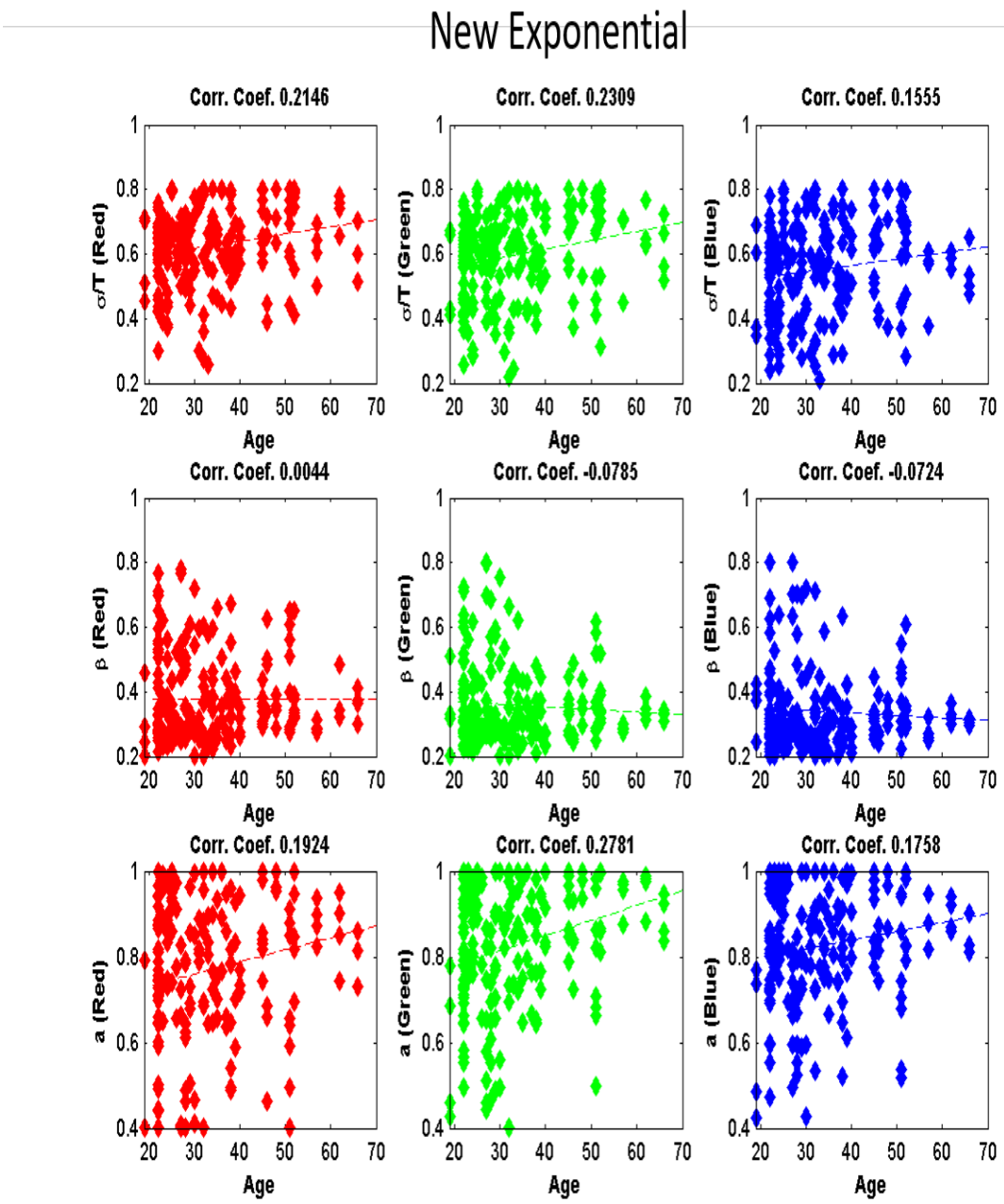

Figure 5.4: The estimated parameter plots for the new Exponential model done using all 48 subjects; including all facial sections. The top of each plot shows its correlation coefficient.

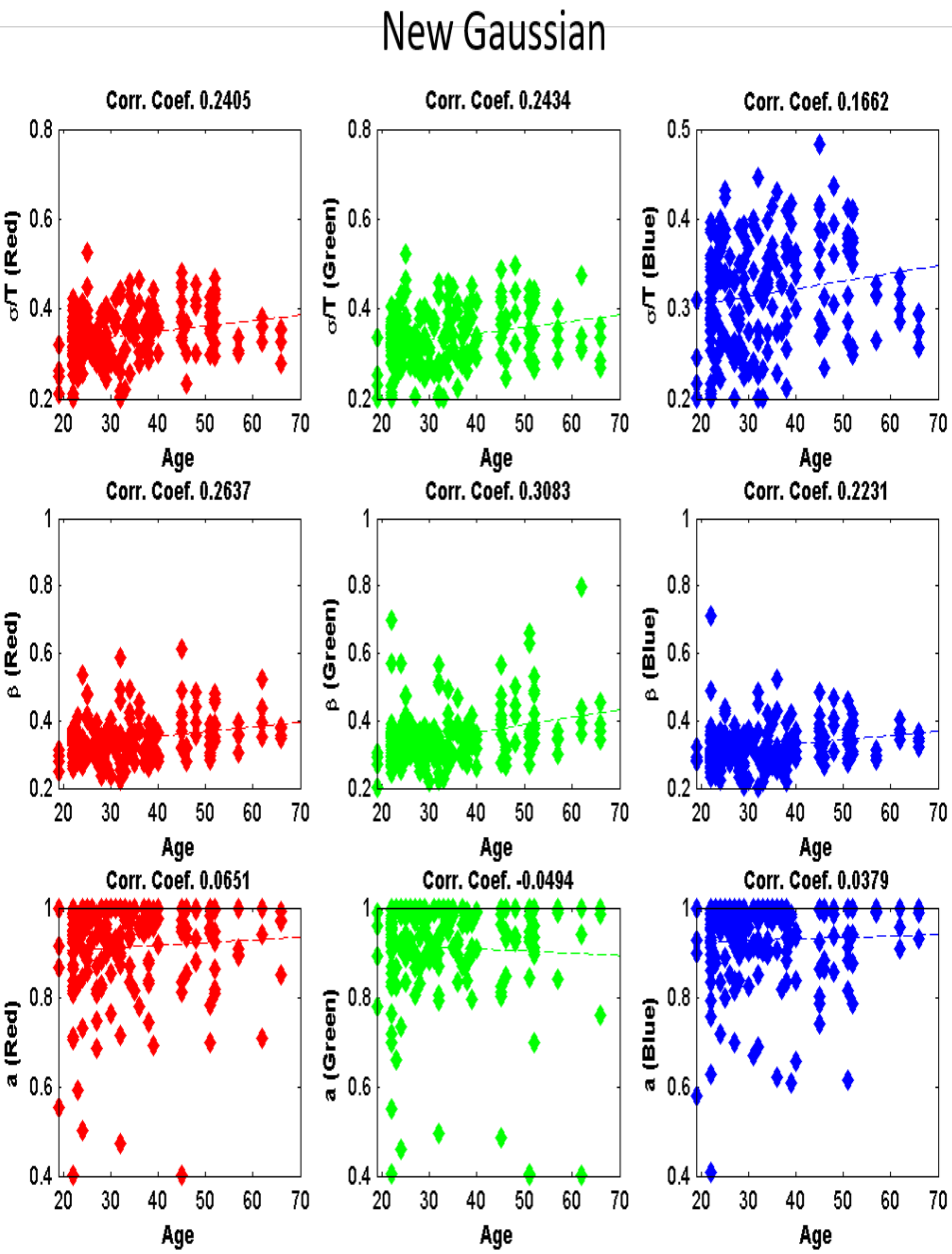

Figure 5.5: The estimated parameter plots for the new Gaussian model done using all 48 subjects; including all facial sections. The top of each plot shows its correlation coefficient.

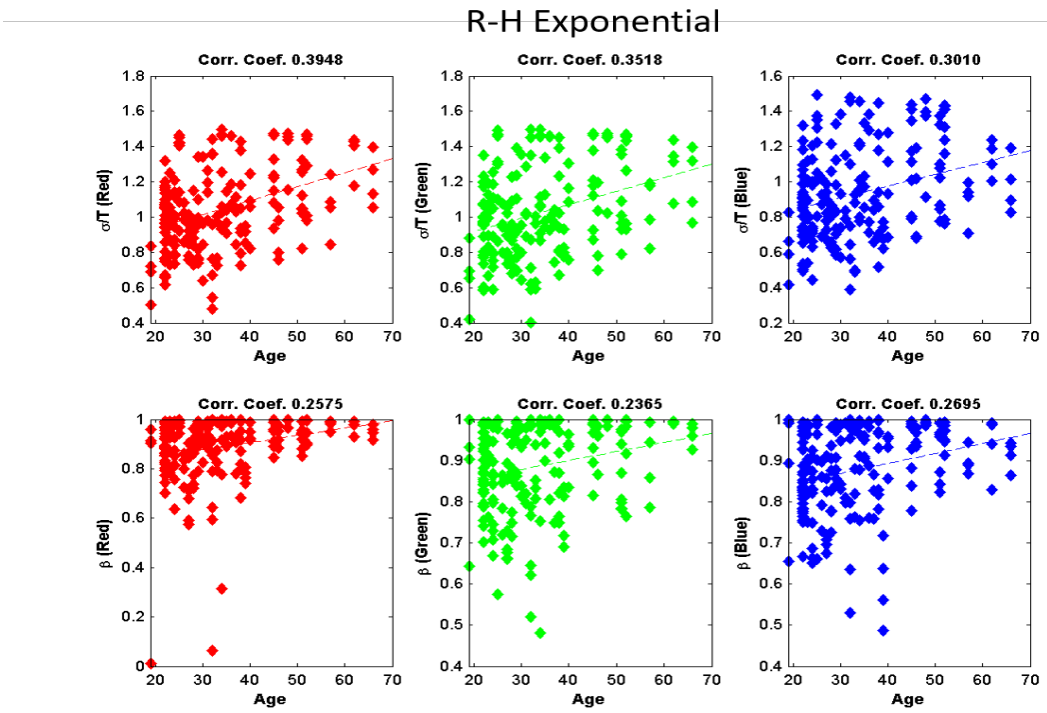

Figure 5.6: The estimated parameter plots for the R–H Exponential model done using all 48 subjects; including all facial sections. The top of each plot shows its correlation coefficient.

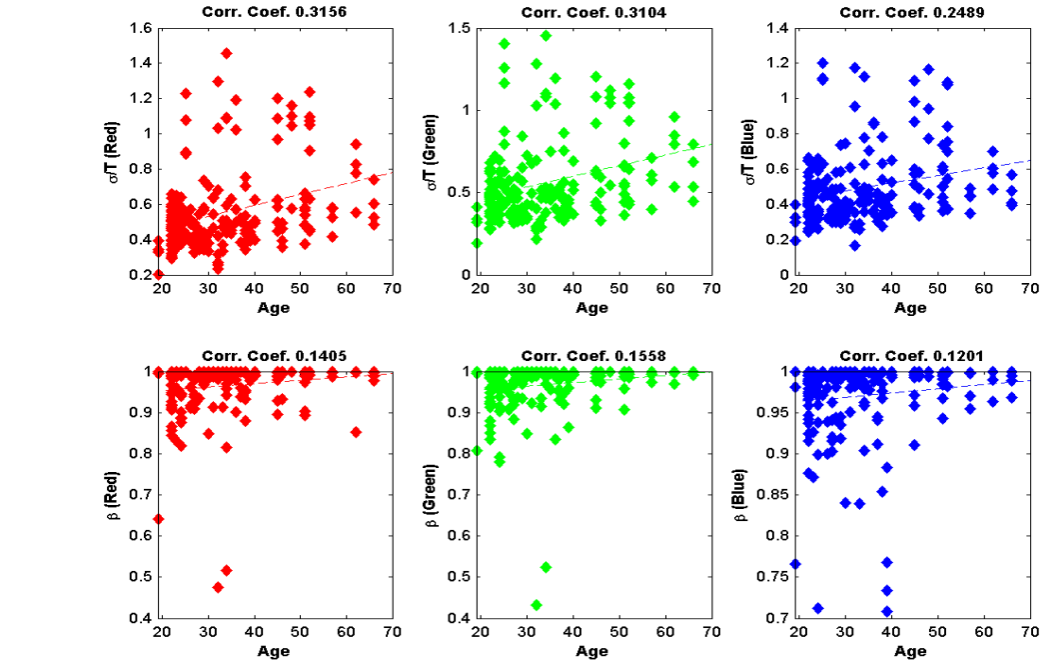

Figure 5.7: The estimated parameter plots for the R–H Gaussian model done using all 48 subjects; including all facial sections. The top of each plot shows its correlation coefficient.

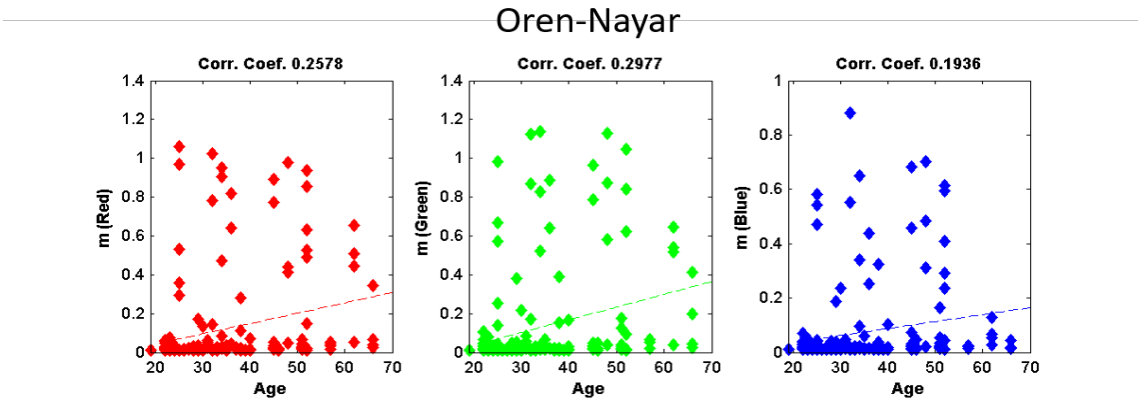

Figure 5.8: The estimated parameter plot for the Oren–Nayar model done using all 48 subjects; including all facial sections. The top of each plot shows its correlation coefficient.

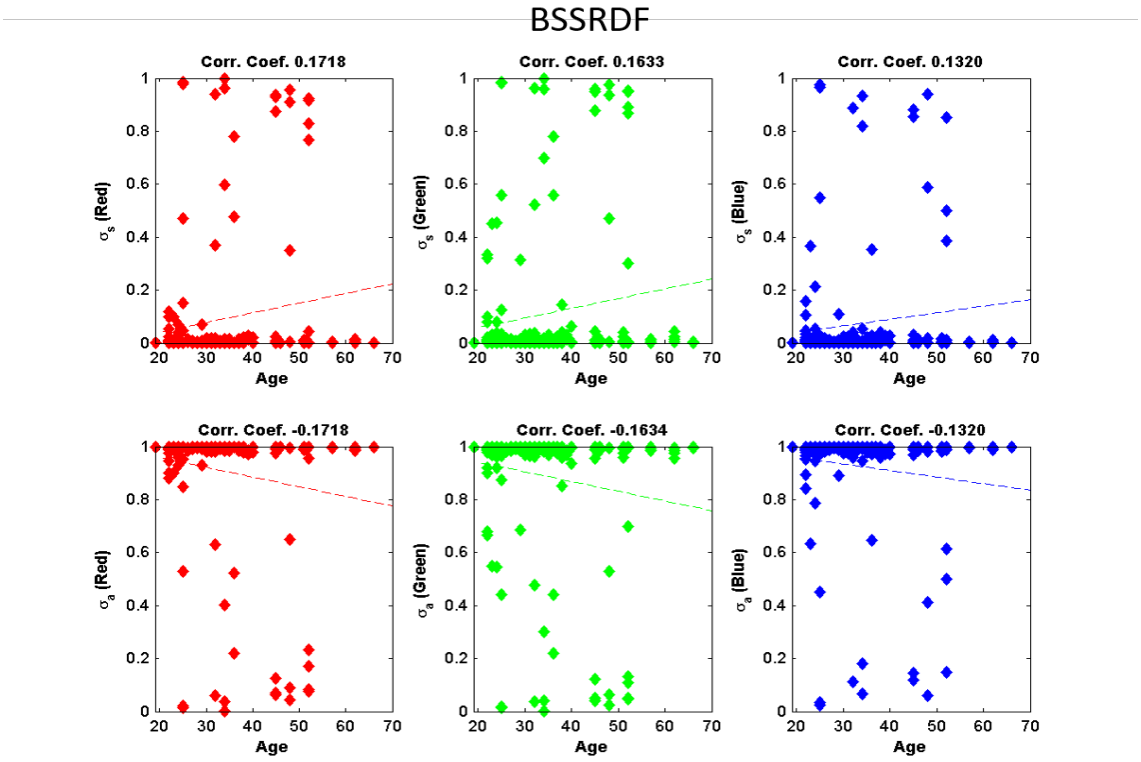

Figure 5.9: The estimated parameter plots for the BSSRDF done using all 48 subjects; including all facial sections. The top of each plot shows its correlation coefficient.

5.3 Analysis on the model relation with the skin property

When using the inverse rendering method to estimate the model parameters by fitting the model under study to the radiance data, the balance parameter β for the new model (and R–H model) behaves differently than what was initially predicted (see Table 4.1). This is due to most of the young subjects having small diffuse radiance size near the surface normal angle, which results in the model estimating that they will have a low β value (e.g. low β means that both the R–H model and the new model will exhibit small outgoing radiance curve –please refer to Chapter 3). For the new model, the estimation of absorption a is easily affected by the wavelength, the subject's skin type, and, also, the model's correlation function (Exponential or Gaussian). Only the roughness parameter behaves in accordance with the prediction (Table 4.1) and the literature; that aging will cause an increase in the model roughness parameter values.

5.4 Discussion on the parameter-age test

In the search for the best-fit parameters, the new model Exponential has the lowest Δ_{RMS}, followed by the new model Gaussian. The BSSRDF exhibited the overall highest error, followed by the Oren–Nayar model (see Figure 5.2). The BSSRDF and the Oren–Nayar models were both designed to model large diffuse radiance, so, in this test, they failed to properly fit to sample radiances that are less diffuse. For example, when the roughness parameters are set to the lowest value (e.g. ≈ 0) for each of the models, the outgoing radiance for the BSSRDF and the Oren–Nayar models was observed to be much wider than both the new and the R–H models. Meanwhile, the σ/T and β estimated values for the new models are lower than the R–H model counterpart (Figure 5.4-5.7). This is due to the parameter a increasing the flexibility of the new model.

An interesting pattern emerged from the correlation results when all samples were considered (Table 5.2-5.4). The roughness parameters for the new, R–H, Oren–Nayar and BSSRDF models (e.g. σ/T, m, and σ_s) suggest that a significant positive correlation with age exists ($p < 0.05$). This is true for both male and female subjects, including the subjects that wear makeup or facial cream. These results support the literature regarding skin roughness (see Table 4.1). However, for the new model, β and a parameters show no strong pattern or relation with age. This is because these parameters are more affected by the skin type and condition. The new model Exponential parameters have more variation

for the a parameter than the Gaussian version. However, the Gaussian version has higher error count than the Exponential one. The regression line is fitted on the estimated parameter to observe the relation between the age and the parameters. The chi-square for fit calculated were ≈ 1.008 for all the plots (see Figure 5.4 to 5.9). Meanwhile, the Oren-Nayar and BSSRDF model parameters have outliers that affect the regression line placement (see Figure 5.8 and 5.9).

5.5 The roughness parameter-age test for a specific category

Multiple studies have suggested that factors like gender, ethnicity and cosmetic use do result in differences in appearances as people age chronologically [20–22, 58, 66, 85, 90, 94, 100]. As a result of this, I have undertaken some additional parameter-age tests based on specific factors. The purpose of these tests is to observe whether there is any significant result when only the subjects with specific category are used. It should be noted that, for these tests, I only considered the correlation between the roughness parameter and the age of the subject. These categories are: 1) Gender (Male or Female); 2) Face section (Forehead, Left Cheek, Right Cheek, Both Cheek, Nose or All sections); 3) Fitzpatrick Skin Type (2, 3, 4, 5 or all); and 4) Cosmetics (With, Without or include both with and without). The methodology for these parameter-age tests are the same as above, except that the subject in the dataset that fit with one of the chosen categories were selected for the experiment. For example, if the chosen category was to use only the male subjects, then only the male subjects were used for the parameter-age test, regardless of their skin type, face section and whether they wore cosmetics or not. I only highlighted and discussed results from the categories that have the most significant correlation that appears on most of the models. These highlighted categories are the gender (male and female) and face sections (forehead and both left and right cheek). Other results may be mentioned in circumstance where they warrant attention.

Table 5.5 and 5.6 show the roughness parameters and age correlation results within the model for males and females in each gender category. Comparing the two tables (all male versus all female), the results show that most of the light scattering models obtained a positive significant correlation only when the female subjects were used. This result seems to imply that the age of the female candidates is able to be distinguished more easily than that of the males and that the results from the female candidates can be more easily compared when the model roughness parameter is used for the age estimation. However,

half of the female candidates wore cosmetics, and, as outline above, cosmetics tend to affect the light scattering, which will likely effect their overall skin light scattering. The purpose of make up or facial cream is to make skin scatter light evenly [20, 22, 39, 112]. However, interestingly enough, since most female in the samples across the age groups wore make up, the results still show that the older female have rougher skin than the younger ones. This indicate that the more older they are, the more make up (or cream) they apply on their face, hence, the more light scatters due to the multiple layers of make up they have. Meanwhile, Table 5.7 and 5.8 show the correlation results between the model roughness parameters and age for the Forehead section and both cheek sections in the face section category. Given that most of the models with strong positive correlations occur within these sections, it may be implied that these sections are the best sections for estimating age using the roughness parameter. Meanwhile, the correlation between the skin type and age, and the correlation between the cosmetics categories (With, Without or include both with and without) and age was observed by the author to have mostly weak correlation results; very few models shown to have significant correlation results. This is because when the dataset samples are divide based on these categories, the distribution of the subjects across the various ages becomes uneven, which may, in turn, affect the correlation process.

5.6 Age classification using the model parameters

To test how the parameter fare when using as an aging feature, an age estimation experiment was conducted using all the subjects, which include all gender, skin type, and face sections, giving a total of 192 samples overall. For classification method, the author decided to use the support vector machine (SVM) [99], which is supervised machine learning algorithm that can analyze data to be used for classification. The author uses SVM due to the author familiarity with the method. In SVM, a hyperplane is created to best separate the points in the input variable space by their class, either class 0 or class 1. The numeric input variables in your data form an n-dimensional space. For example, if there are two input variables, this would form a two-dimensional space. A hyperplane is a line that splits this input variable space. It can be visualized in 2-dimensions as a line and lets assume that all of the input points can be completely separated by this line. By using the samples age as its variable, the author can classify the data into two different age.

Table 5.5: Correlation coefficients between the roughness parameter and the subject age for all models using just the Male candidates. (White cell $p < 0.05$; Grey cell: $0.1 < p < 0.2$)

Model	Roughness Parameter	R	G	B
New Exponential	σ/T	0.2204	0.2345	0.1756
New Gaussian	σ/T	-0.0096	0.05847	-0.0585
R-H Exponential	σ/T	0.3516	0.2852	0.2374
R-H Gaussian	σ/T	0.1944	0.2016	0.1476
Oren-Nayar	m	0.1730	0.2426	0.1107
BSSRDF	σ_s	0.0217	0.0155	0.0023

Table 5.6: Correlation coefficients between the roughness parameter and the subject age for all models using just the Female candidates. (White cell $p < 0.05$; Grey cell: $0.1 < p < 0.2$)

Model	Roughness Parameter	R	G	B
New Exponential	σ/T	0.1087	0.1492	0.0730
New Gaussian	σ/T	0.3767	0.32354	0.2743
R-H Exponential	σ/T	0.3347	0.3188	0.2731
R-H Gaussian	σ/T	0.3682	0.3481	0.2832
Oren-Nayar	m	0.3124	0.3013	0.2702
BSSRDF	σ_s	0.3779	0.3514	0.3167

Table 5.7: Correlation coefficients between the roughness parameter and the subject age for all models using just the Forehead section of all candidates. (White cell $p < 0.05$; Grey cell: $0.1 < p < 0.2$)

Model	Roughness Parameter	R	G	B
New Exponential	σ/T	0.3178	0.4057	0.3649
New Gaussian	σ/T	0.3967	0.5033	0.4154
R-H Exponential	σ/T	0.5502	0.5651	0.5658
R-H Gaussian	σ/T	0.4698	0.5430	0.5379
Oren-Nayar	m	0.3688	0.4847	0.3702
BSSRDF	σ_s	0.1700	0.2276	0.1431

Table 5.8: Correlation coefficients between the roughness parameter and the subject age for all models using both left and right Cheek sections of all candidates. (White cell $p < 0.05$; Grey cell: $0.1 < p < 0.2$)

Model	Roughness Parameter	R	G	B
New Exponential	σ/T	0.2554	0.2291	0.0631
New Gaussian	σ/T	0.2627	0.2239	0.1195
R-H Exponential	σ/T	0.4313	0.3650	0.2887
R-H Gaussian	σ/T	0.3510	0.3304	0.2335
Oren-Nayar	m	0.3256	0.3528	0.2287
BSSRDF	σ_s	0.2385	0.2016	0.1732

The MATLAB has a build in SVM function that the author used for this age classification experiment. The experiment is done by first selecting a parameter as the aging feature (i.e. roughness), then hold-out 10% (or 19 samples) of the 192 samples to be used as testing samples, while the rest as training samples. The tests are done for each model parameters. In this experiment, the samples are group into their specific age groups: 1) Subjects below age 30 as age group 20, 2) Subjects age between 30-39 as age group 30, 3) Subjects age between 40-49 as age group 40, and 4) Subjects above age 49 as age group 50. The experiment is done on different colour channels to observe if there any difference in accuracy between channels. Here, the age classification is done by classifying the test subjects between two different age groups; example, classify subject between age group 20 versus 30; 20 versus 40; 20 versus 50; 30 versus 40; 30 versus 50; and 40 versus 50. The average accuracy is calculated based on the correct classification of the subject with its true age.

Table 5.9 show the age classification accuracy results for each of the different model parameters used as the aging feature. From the results, it can be seen that the parameters estimated using the new Exponential model are the parameters that can give good age classification when used as an aging feature. However, in this age classification experiment, there is a problem classifying the subjects that are above age group 20 into their corrected age group (not shown here). This may be due to the uneven distribution of subjects between age groups, where, subjects in age group 20 having more than the other age groups. To solve this problem, adding more subjects with age above 30 years old may

improve the SVM training process of this experiment. Another alternative is by solving the uneven data distribution problem using weighted examples. Nevertheless, this cannot be done due to time limitation.

Table 5.9: The age estimation accuracy for all samples (gender, skin types, and face sections) using the model roughness parameters as the aging feature. This table for the New models (both Exponential and Gaussian variants).

Parameter (Roughness)	New Exponential ($\frac{\sigma}{T}$)			New Gaussian ($\frac{\sigma}{T}$)		
	R	G	B	R	G	B
Accuracy (%)	70.13	69.24	69.24	69.67	69.67	68.48
Total Average Accuracy (%)	69.54			69.28		

Table 5.10: The age estimation accuracy for all samples (gender, skin types, and face sections) using the model roughness parameters as the aging feature. This table for the R–H model (both Exponential and Gaussian variants).

Parameter (Roughness)	R-H Exponential ($\frac{\sigma}{T}$)			R-H Gaussian ($\frac{\sigma}{T}$)		
	R	G	B	R	G	B
Accuracy (%)	66.9	67.24	69.08	67.59	68.63	68.48
Total Average Accuracy (%)	67.74			68.24		

Table 5.11: The age estimation accuracy for all samples (gender, skin types, and face sections) using the model roughness parameters as the aging feature. This table is for the Oren–Nayar model and the BSSRDF model.

Parameter (Roughness)	Oren-Nayar (m)			BSSRDF (σ_s)		
	R	G	B	R	G	B
Accuracy (%)	68.04	68.63	65.81	67.89	67.29	66.25
Total Average Accuracy (%)	67.5			67.14		

Table 5.12: The age estimation accuracy for all samples (gender, skin types, and face sections) using the model balance parameters as the aging feature. This table for the New models (both Exponential and Gaussian variants).

Parameter (Balance parameter)	New Exponential (β)			New Gaussian (β)		
	R	G	B	R	G	B
Accuracy (%)	69.74	71.33	69.24	67.20	67.94	67.16
Total Average Accuracy (%)	69.94			67.43		

Table 5.13: The age estimation accuracy for all samples (gender, skin types, and face sections) using the model balance parameters as the aging feature. This table for the R–H model (both Exponential and Gaussian variants).

Parameter (Balance parameter)	R-H Exponential (β)			R-H Gaussian (β)		
	R	G	B	R	G	B
Accuracy (%)	67.16	67.16	69.84	67.16	69.24	68.65
Total Average Accuracy (%)	68.05			68.35		

Table 5.14: The age estimation accuracy for all samples (gender, skin types, and face sections) using the model absorption parameters as the aging feature. This table for the New models (both Exponential and Gaussian variants).

Parameter (Absorption)	New Exponential (a)			New Gaussian (a)		
	R	G	B	R	G	B
Accuracy (%)	69.24	69.24	69.24	69.24	67.71	67.16
Total Average Accuracy (%)	69.24			68.03		

Table 5.15: The age estimation accuracy for all samples (gender, skin types, and face sections) using the model absorption parameters as the aging feature. This table is for the BSSRDF model.

Parameter (Absorption)	BSSRDF (σ_a)		
	R	G	B
Accuracy (%)	67.89	67.29	66.25
Total Average Accuracy (%)	67.14		

5.7 Summary

In this chapter, we have provided details regarding an experiment designed to determine whether the light scattering models estimated parameters correlate with the age of various subjects. The behavior of the roughness parameters (σ/T, m and σ_s) and the parameters of all models are in line with the skin optic and computer vision literature; that is to say that the roughness parameter (or skin surface/subsurface roughness) increases with age. The results in this chapter suggest that the selected light scattering models, especially the new models (Exponential and Gaussian variants), can be used to approximately determine the age of a subject. This is proven in the age classification experiment (in Section 5.6) where the model parameters are used as the aging feature for trainig and testing; while the support vector machine is used as the classifier. Meanwhile, light scatter differ across age are more apparent on the forehead section and both the left and right cheeks (when included together). This is understandable since those sections are where aging features tend to appear. However, it should be noted that the confirmation of the results of the experiment regarding the relationship between the model parameter and the subject age would be much stronger if a dataset that featured similar subjects captured as they age progressively was considered, instead of using different subjects with different ages. As outline above, this was not possible because of the time and cost limitations of this study, we made do with the images of the volunteer subjects that were captured.

Chapter 6

Conclusion

Inverse rendering is usually used to test a model's accuracy and to analyzed the parameters estimated by the model. When fitting the light scattering model to the data measurements, each of the model's parameters would have a different role on shaping the behavior (or curve shape) of the model's outgoing radiance. We need to consider what the parameter values would be when applied on different facial skin surfaces that vary with age. Would there be any relation between the parameter values and the subject's age? If yes, then this suggests that a light scattering model has the capacity to be used as an alternative estimator of age, which can be used in conjunction to other face aging extractors. Nevertheless, we need to confirm this first and find out whether it is possible for a model to be used in this manner and investigate any limitations that it may have.

To recap, the aim of this thesis is to study whether a light scattering model is capable of being used as an alternative estimator of age. An investigation into the relationship between the parameters of various models and the age of various subjects was undertaken. The parameter-age test results detailed in Chapter 5 suggests that the roughness parameter for the model chosen for this experiment demonstrate a significant positive relationship with age, and can, therefore, be used to determine the approximate age of a subject. This is true in circumstances where parameters, other than the roughness parameter, are controlled.

The author also has used the estimated model parameters for an age classification experiment, proving that the parameter can be used to approximately determine a subject's age. This thesis has shown that an analytical-based light scattering model parameter can be used as an alternative method of estimating a person's age. Moreover, it can also be used in conjunction with other age extractor/estimator methods so as to strengthen the

estimation accuracy, such as the active appearance model (AAM), which is use for estimating facial shape and Gabor filter, which is an extractor for aging wrinkles . The idea of using the light scattering of the skin to estimate age is a novel idea; one that requires more focus studies to ascertain how to build a robust light scattering AND age estimation model that can directly classify skin traits without directly measuring it. For the rest of this chapter, the author will highlight the thesis contributions and the limitations. The author will also propose some suggestions for future study.

6.1 Thesis contributions

This thesis main contribution is confirming that the parameters of a light scattering model can actually be used as an aging feature for classifying the age of a person. This is proven by the experiments in Chapter 5 where the model parameters are used for classifying the subject's age. Besides this, the thesis also has six other novel contributions, which are:

1. The presentation of a method capable of estimating facial skin characteristics using a photometry technique and a light scattering model.

2. The introduction of a new absorptive laminar light scattering model that defines a simple light absorption term using the conservation of light energy.

3. Testing of the functionality and accuracy of the new model on both the isotropic (CUReT database) and anisotropic (UTIA database) samples.

4. Establishing a justifiable relationship between the model parameters and the captured samples characteristics by correlating their parameter estimations with their degree of polarization.

5. The introduction of a new image alignment technique for aligning image sequence captured in disparate illumination environments.

6. Testing of the correlation between the age of various subjects and the parameters of the model that are related to the skin characteristics. Results that support the skin optic, medical, human perception and psychophysics literature have been highlighted.

Tools have always been adapted and used in situation that they were not necessarily built for. If the tool has the potential to be used for a different task that was not considered

when it was initially designed, why not use it? Expanding the light scattering model so that it can be used for estimating age might have potential benefits for the computer vision and skin optic fields.

6.2 Thesis limitations

The first main limitation of this thesis is the limited subjects (or volunteers) collected for the main parameter-age test. If there were more subjects, especially for subjects aging above 30 years old, the test results will be more concrete. The second main limitation is that there are no real measurements for the estimated parameters to compare with. The estimated parameters were assumed to be true based on the model fitting to the scattering radiance. Meanwhile, there are also other limitations that focus on the proposed models, image acquisition, image alignment, model-polarization test, and the parameter-age experiment. Here, these limitations are described and also highlight some areas of improvement for future reference.

6.2.1 The absorptive laminar light scattering model

The proposed model - the absorptive laminar light scattering model - is a modified version of the Ragheb-Hancock (R–H) model [81]. The new model used the rule of light energy conservation to define an absorption term that is simple and unit-less for easier analysis. The model's absorption, also assumed that the light absorption is instantaneous, so, the distance of light traveled within the subsurface layer can be ignored. Similar to R–H model, the new model assume that the diffuse radiance is scatterd from bi-layered rough surfaces, consisting of an opaque subsurface layer below a transparent one. The surface layer and the subsurface layer are parallel and only single scattering occur in the subsurface layer. The surface layer was modeled by a single surface scattering component, while the subsurface layer was modeled using the combination of both the effects of radiance transmission through the surface layer and a single subsurface scattering component.

6.2.2 The image acquisition and alignment

In this thesis, the light stage [13] and Ma et al. photometry technique [64] were used for capturing both the surface normal map and light reflectance of various objects. The author has presented a new alignment technique for managing errors resulting from small

movements that are likely to occur during image sequences captured in disparate illumination environments. The alignment technique aligns small inter-frame motions captured in spherical gradient photometric stereo. However, the technique does not accurately align inter-frame movements when the photometric images are captured in changing lighting conditions. The reason for this being that illumination-independent transformation failed when it was applied to the flash image (e.g. image captured with the camera flash) as a result of the attenuation difference. This later results in inaccurate movement flow estimation. Due to the equipment limitation, it was difficult to calibrate the LEDs and the camera flash in a manner that would produce the closest attenuation effect. In order to manage this issue in the future, the capturing sequence for the flash image could be reorganized and used in conjunction with the extrapolation technique. This may help to improve the image flow alignment.

6.2.3 The model-polarization test

In the correlation test between the degree of polaization (DOP) and the model parameters, the absorption parameter a of the new model showed no strong relation to the polarization. It may be that there is really no strong relation between the two, or, that there is some hidden property that impacts the overall result. The second option is more likely in the authors opinion. Furthermore, there is no proof that suggests that the relationship between the two is truly weak. In order to do this we would need to measure the sample's absorption properties directly, which would require additional time and special equipment. Nevertheless, this problem should be investigated further in the future.

6.2.4 The parameter-age test and methodology

Older candidates exhibited difficulty entering the light stage, since there was no proper door through which they could enter. The physical condition and comfort of the volunteers should be considered more carefully in the future. The study was limited by the characteristics of the skin of the volunteers. It was difficult to obtain samples from older participants due to the physical set up of the experiment and the importance of consent. Additionally, errors resulting from movement and facial obstruction are unavoidable. So, some adjustments were made by the author (where the adjustments have been thoroughly described in section 4.5).

Most of the volunteers are people who work indoors. People who work indoors would

generally have less photoaging damage and are probably less active, than people who work outdoors. This may cause some of the volunteers to appear younger even when their chronological age is above 30. Additionally, the data collection involved more candidates aged below 29. Most of these volunteers are acquainted with the author, meaning that most of the volunteers are Malaysian (22 people out of 48). Regarding volunteers above the age 50, most were staff who work in the same department as the author who kindly agreed to help. So most of the older volunteers are Englishmen (7 people out of 48). Furthermore, due to time limitations, the dataset used in this experiment consisted of different subjects with different ages. The author will plan to capture subjects over time in order to assess their age as it progresses for the future study.

Finally, the parameter-age test in Chapter 5 suggests that the parameters from an analytical-base light scattering model can be used to approximately determine the age of a subject. This thesis, however, did not extend the study to observe how accurate the chosen parameter (e.g. roughness parameter) is when estimating the subject's age. These further investigations were not within the scope of this thesis, and more time would have been required, not to mention the additional expense that would have been incurred, in order to extend the study. Nevertheless, this thesis suggests that the parameters of an analytical-base light scattering model can be used as an alternative method to estimate a person's age. Moreover, it can be used in conjunction with other age extractor/estimator methods to increase the accuracy of the estimate.

6.3 Future studies

In the future, it would be interesting to test the ability of the model's parameters to accurately estimate the age of a subject. A suitable classifier or a machine learning would be needed to train and classify the age using the parameters. A robust technique that can integrate both the machine learning and the proposed light scattering model would be preferable. Additionally, it is possible that the lighting condition for the current experiment may improve if the LeGendre et al. [56] practical method is used to reproduce and capture multiple incident illumination spectra. This could warrant further investigation. Moreover, the rendering of the skin using the new model should be studied further to observe the capability of the new model in this regard. The author will be conducting a future study regarding the variety of absorption value while using the estimated skin parameters.

Capturing the skin micro-structure may help enhance the skin micro-surface roughness which may, in turn, aid estimation accuracy based on the surface normal map of a subject. Nagano et al. [70] and Graham et al. [33] both presented a 10-micron resolution scanning technique to measure *in vivo* skin samples. Using this technique might help to improve the capturing of the skin micro-traits which would increase our understanding of the effects of aging on the skin surface and, also, the light scattering behavior.

Furthermore, it would be interesting to see whether we can design an absorptive light scattering model with an absorption term that uses standard light absorption measurement, such as the complex refractive index or the attenuation coefficient. Using either of these measurements as the model parameter would mean that the model was based more on the actual physical condition of the skin and would therefore allow for standardized the measurements. With that in mind, the new absorption function would need to be defined in a manner that is consistent with the whole model equation.

Lastly, the refractive index is one of the physicochemical properties of substances (or optical medium). Much like light absorption, it can provide information about the behavior of light when light passes between two different substances, which can provide us with information about the molecules of components in both of the substrates. However, in this thesis, the estimated value obtained while using the new model to estimate the refractive index was too different from the reference value. The author considers that this casts doubt on whether the refractive index estimated by the new model is correct or not. Because of this, the author decided to not use the refractive index in the parameter-age test. Further investigation is required in this regard. Nevertheless, this topic of investigation can help to improve the application of the light scattering model, and may allow for the broadening of its use to computer vision and graphics, security and also potentially in medical fields. Two example applications: 1) the parameters estimated by the model can be used by medical expert to study any aging related diseases that might occur during aging; and 2) the model can be used in security cameras to detect and estimate the age of a person by using their skin's light scattering instead.

References

[1] Index of Refraction. `http://hyperphysics.phy-astr.gsu.edu/hbase/Tables/indrf.html`, 2018. [Online; accessed March 26, 2018].

[2] R. R. Anderson and J. A. Parrish. The optics of human skin. *Journal of investigative dermatology*, 77(1):13–19, 1981.

[3] R. R. Anderson and J. A. Parrish. Optical properties of human skin. In *The science of photomedicine*, pages 147–194. Springer, 1982.

[4] G. A. Atkinson and E. R. Hancock. Recovery of surface orientation from diffuse polarization. *IEEE transactions on image processing*, 15(6):1653–1664, 2006.

[5] L. D. Barron. *Molecular light scattering and optical activity*. Cambridge University Press, 2004.

[6] C. F. Bohren and D. R. Huffman. *Absorption and scattering of light by small particles*. John Wiley & Sons, 2008.

[7] Forest B. H. Brown. The refraction of light in plant tissues. *Bulletin of the Torrey Botanical Club*, 47(6):243–260, 1920.

[8] A. L. Chien, J. Suh, S. S. A. Cesar, A. H. Fischer, N. Cheng, F. Poon, B. Rainer, S. Leung, J. Martin, G. A. Okoye, et al. Pigmentation in african american skin decreases with skin aging. *Journal of the American Academy of Dermatology*, 75(4):782–787, 2016.

[9] S. E. Choi, Y. J. Lee, S. J. Lee, K. R. Park, and J. Kim. Age estimation using a hierarchical classifier based on global and local facial features. *Pattern Recognition*, 44(6):1262–1281, 2011.

[10] H. A. Dahlan and E. R. Hancock. Absorptive scattering model for rough laminar surfaces. In *Pattern Recognition (ICPR), 2016 23rd International Conference on*, pages 1905–1910. IEEE, 2016.

[11] H. A. Dahlan, E. R. Hancock, and W. A. P. Smith. Reflectance-aware optical flow. In *Pattern Recognition (ICPR), 2016 23rd International Conference on*, pages 2860–2865. IEEE, 2016.

[12] K. J. Dana, B. V. Ginneken, S. K. Nayar, and J. J. Koenderink. Reflectance and texture of real-world surfaces. *ACM Transactions on Graphics (TOG)*, 18(1):1–34, 1999.

[13] P. Debevec, T. Hawkins, C. Tchou, H. P. Duiker, W. Sarokin, and M. Sagar. Acquiring the reflectance field of a human face. In *Proceedings of the 27th annual conference on Computer graphics and interactive techniques*, pages 145–156. ACM Press/Addison-Wesley Publishing Co., 2000.

[14] C. Donner and H. W. Jensen. A spectral bssrdf for shading human skin. *Rendering Techniques*, 2006:409–418, 2006.

[15] C. Donner, T. Weyrich, E. d'Eon, R. Ramamoorthi, and S. Rusinkiewicz. A layered, heterogeneous reflectance model for acquiring and rendering human skin. *ACM Transactions on Graphics (TOG)*, 27(5):140, 2008.

[16] A. Dutta. Face shape and reflectance acquisition using a multispectral light stage. Master's thesis, University of York, 2010.

[17] M. A. Farage, K. W. Miller, P. Elsner, and H. I. Maibach. Characteristics of the aging skin. *Advances in wound care*, 2(1):5–10, 2013.

[18] J. Filip and R. Vávra. Template-based sampling of anisotropic brdfs. In *Computer Graphics Forum*, volume 33, pages 91–99. Wiley Online Library, 2014.

[19] J. Filip, R. Vavra, M. Haindl, P. Zid, M. Krupika, and V. Havran. Brdf slices: Accurate adaptive anisotropic appearance acquisition. In *Proceedings of the IEEE Conference on Computer Vision and Pattern Recognition*, pages 1468–1473, 2013.

[20] B. Fink, K. Grammer, and P. J. Matts. Visible skin color distribution plays a role in the perception of age, attractiveness, and health in female faces. *Evolution and Human Behavior*, 27(6):433–442, 2006.

[21] B. Fink, P. J. Matts, D. DEmiliano, L. Bunse, B. Weege, and S. Röder. Colour homogeneity and visual perception of age, health and attractiveness of male facial skin. *Journal of the European Academy of Dermatology and Venereology*, 26(12):1486–1492, 2012.

[22] B. Fink, P. J. Matts, S. Röder, R. Johnson, and M. Burquest. Differences in visual perception of age and attractiveness of female facial and body skin. *International journal of cosmetic science*, 33(2):126–131, 2011.

[23] Thomas B Fitzpatrick. The validity and practicality of sun-reactive skin types i through vi. *Archives of dermatology*, 124(6):869–871, 1988.

[24] D. A. Forsyth and J. Ponce. *Computer Vision: A Modern Approach, 2nd Edition*. Pearson, 2012.

[25] Y. Fu, G. Guo, and T. S. Huang. Age synthesis and estimation via faces: A survey. *Pattern Analysis and Machine Intelligence, IEEE Transactions on*, 32(11):1955–1976, 2010.

[26] Y. Fu, Y. Xu, and T. S. Huang. Estimating human age by manifold analysis of face pictures and regression on aging features. In *Multimedia and Expo, 2007 IEEE International Conference on*, pages 1383–1386. IEEE, 2007.

[27] H. W. Gausman, W. A. Allen, and D. E. Escobar. Refractive index of plant cell walls. *Appl. Opt.*, 13(1):109–111, Jan 1974.

[28] X. Geng, Z. H. Zhou, and K. S. Miles. Automatic age estimation based on facial aging patterns. *Pattern Analysis and Machine Intelligence, IEEE Transactions on*, 29(12):2234–2240, 2007.

[29] A. Ghosh, T. Chen, P. Peers, C. A. Wilson, and P. Debevec. Circularly polarized spherical illumination reflectometry. *ACM Trans. Graph.*, 29(6), 2010.

[30] D. H. Goldstein. *Polarized light*. CRC press, 2016.

[31] A. Golovinskiy, W. Matusik, H. Pfister, S. Rusinkiewicz, and T. Funkhouser. A statistical model for synthesis of detailed facial geometry. In *ACM Transactions on Graphics (TOG)*, volume 25, pages 1025–1034. ACM, 2006.

[32] Y. M. Govaerts, S. Jacquemoud, M. M. Verstraete, and S. L. Ustin. Three-dimensional radiation transfer modeling in a dicotyledon leaf. *Applied Optics*, 35(33):6585–6598, 1996.

[33] P. Graham, B. Tunwattanapong, J. Busch, X. Yu, A. Jones, P. Debevec, and A. Ghosh. Measurement-based synthesis of facial microgeometry. In *Computer Graphics Forum*, volume 32, pages 335–344. Wiley Online Library, 2013.

[34] D. Guarnera, G. C. Guarnera, A. Ghosh, C. Denk, and M. Glencross. Brdf representation and acquisition. *Computer Graphics Forum*, 35(2):625–650, 2016.

[35] H. Han, C. Otto, X. Liu, and A. K. Jain. Demographic estimation from face images: Human vs. machine performance. *Pattern Analysis and Machine Intelligence, IEEE Transactions on*, 37(6):1148–1161, 2015.

[36] P. Hanrahan and W. Krueger. Reflection from layered surfaces due to subsurface scattering. In *Proceedings of the 20th annual conference on Computer graphics and interactive techniques*, pages 165–174. ACM, 1993.

[37] H. C. Hulst and H. C. v. d. Hulst. *Light scattering by small particles*. Courier Corporation, 1957.

[38] J. A. I. Guitian, C. Aliaga, A. Jarabo, and D. Gutierrez. A biophysically-based model of the optical properties of skin aging. In *Computer Graphics Forum*, volume 34, pages 45–55. Wiley Online Library, 2015.

[39] T. Igarashi, K. Nishino, and S. K. Nayar. The appearance of human skin: A survey. *Foundations and Trends® in Computer Graphics and Vision*, 3(1):1–95, 2007.

[40] Don Bliss (Illustrator). Skin Anatomy: Image Details - NCI Visuals Online. `https://visualsonline.cancer.gov/images/4604-preview.jpg`, 2018. [Online; accessed March 19, 2018].

[41] S. L. Jacques. Optical properties of biological tissues: a review. *Physics in medicine and biology*, 58(11):R37, 2013.

[42] S. L. Jacques, J. C. R. Roman, and K. Lee. Imaging skin pathology with polarized light. *Journal of biomedical optics*, 7(3):329–340, 2002.

[43] S. L. Jacques, J. R. Roman, and K. Lee. Imaging superficial tissues with polarized light. *Lasers in surgery and medicine*, 26(2):119–129, 2000.

[44] H. W. Jensen, S. R. Marschner, M. Levoy, and P. Hanrahan. A practical model for subsurface light transport. In *Proceedings of the 28th annual conference on Computer graphics and interactive techniques*, pages 511–518. ACM, 2001.

[45] J. R. Jensen. *Remote sensing of the environment: An earth resource perspective 2/e*. Pearson Education India, 2009.

[46] I. K. Shlizerman, S. Suwajanakorn, and S. M. Seitz. Illumination-aware age progression. In *Computer Vision and Pattern Recognition (CVPR), 2014 IEEE Conference on*, pages 3334–3341. IEEE, 2014.

[47] C. Kennedy, M. T. Bastiaens, R. Willemze, J. N. B. Bavinck, C. D. Bajdik, and R. G. J. Westendorp. Effect of smoking and sun on the aging skin. *Journal of investigative dermatology*, 120(4):548–554, 2003.

[48] M. Kerker. *The scattering of light and other electromagnetic radiation*. Elsevier, 2016.

[49] O. Klehm, F. Rousselle, M. Papas, D. Bradley, C. Hery, B. Bickel, W. Jarosz, and T. Beeler. Recent advances in facial appearance capture. In *Computer Graphics Forum*, volume 34, pages 709–733. Wiley Online Library, 2015.

[50] J. Koenderink and S. Pont. The secret of velvety skin. *Machine vision and applications*, 14(4):260–268, 2003.

[51] E. Kohl, J. Steinbauer, M. Landthaler, and R. M. Szeimies. Skin ageing. *Journal of the European Academy of Dermatology and Venereology*, 25(8):873–884, 2011.

[52] G. P. Konnen. *Polarized Light in Nature*. Cambridge University Press, 1985.

[53] A. Krishnaswamy and G. V. G. Baranoski. A biophysically-based spectral model of light interaction with human skin. In *Computer Graphics Forum*, volume 23, pages 331–340. Wiley Online Library, 2004.

[54] Y. H. Kwon and N. V. Lobo. Age classification from facial images. *Computer Vision and Image Understanding*, 74(1):1–21, 1999.

[55] A. Lanitis, C. J. Taylor, and T. F. Cootes. Toward automatic simulation of aging effects on face images. *Pattern Analysis and Machine Intelligence, IEEE Transactions on*, 24(4):442–455, 2002.

[56] C. LeGendre, X. Yu, D. Liu, J. Busch, A. Jones, S. Pattanaik, and P. Debevec. Practical multispectral lighting reproduction. *ACM Transactions on Graphics (TOG)*, 35(4):32, 2016.

[57] Z. Li, U. Park, and A. K. Jain. A discriminative model for age invariant face recognition. *Information Forensics and Security, IEEE Transactions on*, 6(3):1028–1037, 2011.

[58] S. Liew, W. T. L. Wu, H. H. Chan, W. W. S. Ho, H. J. Kim, G. J. Goodman, P. H. L. Peng, and J. D. Rogers. Consensus on changing trends, attitudes, and concepts of asian beauty. *Aesthetic plastic surgery*, 40(2):193–201, 2016.

[59] T. Lillesand, R. W. Kiefer, and J. Chipman. *Remote sensing and image interpretation*. John Wiley & Sons, 2014.

[60] C. Liu. *Beyond pixels: exploring new representations and applications for motion analysis*. PhD thesis, MIT, 2009.

[61] Z. Liu, Z. Zhang, and Y. Shan. Image-based surface detail transfer. *Computer Graphics and Applications, IEEE*, 24(3):30–35, 2004.

[62] C. Longo, A. Casari, F. Beretti, A. M. Cesinaro, and G. Pellacani. Skin aging: in vivo microscopic assessment of epidermal and dermal changes by means of confocal microscopy. *Journal of the American Academy of Dermatology*, 68(3):e73–e82, 2013.

[63] R. M. Soldado and C. U. Almagro. An overview of brdf models. 2012.

[64] W. C. Ma, T. Hawkins, P. Peers, C. F. Chabert, M. Weiss, and P. Debevec. Rapid acquisition of specular and diffuse normal maps from polarized spherical gradient illumination. In *Proceedings of the 18th Eurographics conference on Rendering Techniques*, pages 183–194. Eurographics Association, 2007.

[65] S. MacMary, J. Sainthillier, and P. Humbert. How to evaluate aging skin: Tools and techniques. *Cosmetic Medicine and Surgery*, 2017.

[66] P. J. Matts, B. Fink, K. Grammer, and M. Burquest. Color homogeneity and visual perception of age, health, and attractiveness of female facial skin. *Journal of the American Academy of Dermatology*, 57(6):977–984, 2007.

[67] Archibald T. McPherson and Arthur D. Cummings. Refractive index of rubber. *Rubber Chemistry and Technology*, 8(3):421–429, 1935.

[68] J. A. Muccini, N. Kollias, S. B. Phillips, R. R. Anderson, A. J. Sober, M. J. Stiller, and L. A. Drake. Polarized light photography in the evaluation of photoaging. *Journal of the American Academy of Dermatology*, 33(5):765–769, 1995.

[69] Swapna Mukherjee. *Physical Properties of Clay and Soil Mechanics*, pages 54–68. Springer Netherlands, Dordrecht, 2013.

[70] K. Nagano, G. Fyffe, O. Alexander, J. Barbic, H. Li, A. Ghosh, and P. E. Debevec. Skin microstructure deformation with displacement map convolution. *ACM Trans. Graph.*, 34(4):109–1, 2015.

[71] S. Neerken, G. W. Lucassen, M. A. Bisschop, E. Lenderink, and T. A. M. Nuijs. Characterization of age-related effects in human skin: a comparative study that applies confocal laser scanning microscopy and optical coherence tomography. *Journal of biomedical optics*, 9(2):274–281, 2004.

[72] K. P. Nielsen, L. Zhao, J. J. Stamnes, K. Stamnes, and J. Moan. The optics of human skin: Aspects important for human health. *Solar Radiation and Human Health*, 1:35–46, 2008.

[73] Beautiful on Raw. Facial Strigil: Skin Exfoliator Tool — Beautiful on Raw. `https://https://www.beautifulonraw.com/skin_exfoliator_tool.html`, 2018. [Online; accessed March 14, 2018].

[74] M. Oren and S. K. Nayar. Generalization of the lambertian model and implications for machine vision. *International Journal of Computer Vision*, 14(3):227–251, 1995.

[75] A. J. O'Toole, T. Price, T. Vetter, J. C. Bartlett, and V. Blanz. 3d shape and 2d surface textures of human faces: The role of averages in attractiveness and age. *Image and Vision Computing*, 18(1):9–19, 1999.

[76] E. Patterson, A. Sethuram, M. Albert, K. Ricanek, and M. King. Aspects of age variation in facial morphology affecting biometrics. In *Biometrics: Theory, Applications, and Systems, 2007. BTAS 2007. First IEEE International Conference on*, pages 1–6. IEEE, 2007.

[77] DR Perry, HM Appleyard, G Cartridge, PGW Cobb, GE Coop, B Lomas, GG Ritchie, C Taylor, MJ Welch, CA Farnfield, et al. *Identification of textile materials*. Textile Institute, 1985.

[78] Mikhail Polyanskiy. RefractiveIndex.INFO - Refractive index database. `https://refractiveindex.info`, 2018. [Online; accessed March 26, 2018].

[79] H. Ragheb and E. R. Hancock. Testing new variants of the beckmann–kirchhoff model against radiance data. *Computer Vision and Image Understanding*, 102(2):145–168, 2006.

[80] H. Ragheb and E. R. Hancock. The modified beckmann–kirchhoff scattering theory for rough surface analysis. *Pattern Recognition*, 40(7):2004–2020, 2007.

[81] H. Ragheb and E. R. Hancock. A light scattering model for layered dielectrics with rough surface boundaries. *International journal of computer vision*, 79(2):179–207, 2008.

[82] N. Ramanathan and R. Chellappa. Modeling age progression in young faces. In *Computer Vision and Pattern Recognition, 2006 IEEE Computer Society Conference on*, volume 1, pages 387–394. IEEE, 2006.

[83] N. Ramanathan, R. Chellappa, and S. Biswas. Computational methods for modeling facial aging: A survey. *Journal of Visual Languages & Computing*, 20(3):131–144, 2009.

[84] N. Ramanathan, R. Chellappa, S. Biswas, et al. Age progression in human faces: A survey. *Journal of Visual Languages and Computing*, 15:3349–3361, 2009.

[85] A. V. Rawlings. Ethnic skin types: are there differences in skin structure and function? *International Journal of Cosmetic Science*, 28(2):79–93, 2006.

[86] M. G. Rhodes. Age estimation of faces: A review. *Applied Cognitive Psychology*, 23(1):1–12, 2009.

[87] R. J. Rohrich and J. E. Pessa. The fat compartments of the face: anatomy and clinical implications for cosmetic surgery. *Plastic and reconstructive surgery*, 119(7):2219–2227, 2007.

[88] S. M. Rusinkiewicz. A new change of variables for efficient brdf representation. In *Rendering Techniques 98: Proceedings of the Eurographics Workshop in Vienna, Austria, June 29July 1, 1998*, page 11. Springer Science & Business Media, 1998.

[89] A. Seck, W. A. P. Smith, A. Dessein, B. Tiddeman, H. Dee, and A. Dutta. Ear-to-ear Capture of Facial Intrinsics. *arXiv:1609.02368*, 2016.

[90] Y. Shirakabe, Y. Suzuki, and S. M. Lam. A new paradigm for the aging asian face. *Aesthetic plastic surgery*, 27(5):397–402, 2003.

[91] G. N. Stamatas, R. B. Estanislao, M. Suero, Z. S. Rivera, J. Li, A. Khaiat, and N. Kollias. Facial skin fluorescence as a marker of the skin's response to chronic environmental insults and its dependence on age. *British Journal of Dermatology*, 154(1):125–132, 2006.

[92] H. C. Stimson, D. D. Breshears, S. L. Ustin, and S. C. Kefauver. Spectral sensing of foliar water conditions in two co-occurring conifer species: Pinus edulis and juniperus monosperma. *Remote Sensing of Environment*, 96(1):108–118, 2005.

[93] J. Suo, F. Min, S. Zhu, S. Shan, and X. Chen. A multi-resolution dynamic model for face aging simulation. In *Computer Vision and Pattern Recognition, 2007. CVPR'07. IEEE Conference on*, pages 1–8. IEEE, 2007.

[94] L. Talakoub and N. O. Wesley. Differences in perceptions of beauty and cosmetic procedures performed in ethnic patients. In *Seminars in cutaneous medicine and surgery*, volume 28, pages 115–129. Frontline Medical Communications, 2009.

[95] K. E. Torrance and E. M. Sparrow. Theory for off-specular reflection from roughened surfaces. *JOSA*, 57(9):1105–1112, 1967.

[96] C. Trojahn, G. Dobos, C. Richter, U. B. Peytavi, and J. Kottner. Measuring skin aging using optical coherence tomography in vivo: a validation study. *Journal of biomedical optics*, 20(4):045003–045003, 2015.

[97] T. L. Troy and S. N. Thennadil. Optical properties of human skin in the near infrared wavelength range of 1000 to 2200 nm. *Journal of biomedical optics*, 6(2):167–176, 2001.

[98] N. Tsumura, N. Ojima, K. Sato, M. Shiraishi, H. Shimizu, H. Nabeshima, S. Akazaki, K. Hori, and Y. Miyake. Image-based skin color and texture analysis/synthesis by extracting hemoglobin and melanin information in the skin. *ACM Transactions on Graphics (TOG)*, 22(3):770–779, 2003.

[99] Vladimir Vapnik. *The nature of statistical learning theory*. Springer science & business media, 2013.

[100] N. A. Vashi, M. B. D. C. Maymone, and R. V. Kundu. Aging differences in ethnic skin. *The Journal of clinical and aesthetic dermatology*, 9(1):31, 2016.

[101] C. L. Vernold and J. E. Harvey. Modified beckmann-kirchoff scattering theory for nonparaxial angles. In *SPIE's International Symposium on Optical Science, Engineering, and Instrumentation*, pages 51–56. International Society for Optics and Photonics, 1998.

[102] T. Vetter. Synthesis of novel views from a single face image. *International journal of computer vision*, 28(2):103–116, 1998.

[103] J. Wang, Y. Shang, G. Su, and X. Lin. Age simulation for face recognition. In *Pattern Recognition, 2006. ICPR 2006. 18th International Conference on*, volume 3, pages 913–916. IEEE, 2006.

[104] T. Weyrich, W. Matusik, H. Pfister, B. Bickel, C. Donner, C. Tu, J. McAndless, J. Lee, A. Ngan, H. W. Jensen, et al. Analysis of human faces using a measurement-based skin reflectance model. In *ACM Transactions on Graphics (TOG)*, volume 25, pages 1013–1024. ACM, 2006.

[105] C. A. Wilson, A. Ghosh, P. Peers, J. Y. Chiang, J. Busch, and P. Debevec. Temporal upsampling of performance geometry using photometric alignment. *ACM Trans. Graph.*, 29(2), 2010.

[106] L. B. Wolff. Diffuse-reflectance model for smooth dielectric surfaces. *JOSA A*, 11(11):2956–2968, 1994.

[107] Joseph T. Woolley. Reflectance and transmittance of light by leaves. *Plant Physiology*, 47(5):656–662, 1971.

[108] C. Wynn. An introduction to brdf-based lighting. *Nvidia Corporation*, 2000.

[109] L. Zhang and E. R. Hancock. A comprehensive polarisation model for surface orientation recovery. In *Pattern Recognition (ICPR), 2012 21st International Conference on*, pages 3791–3794. IEEE, 2012.

[110] L. Zhang and E. R. Hancock. Robust estimation of shape and polarisation using blind source separation. *Pattern Recognition Letters*, 34(8):856–862, 2013.

[111] T. Zickler, S. P. Mallick, D. J. Kriegman, and P. N. Belhumeur. Color subspaces as photometric invariants. *International Journal of Computer Vision*, 79:13–30, 08/2008 2008.

[112] M. S. Zimbler, M. S. Kokoska, and J. R. Thomas. Anatomy and pathophysiology of facial aging. *Facial plastic surgery clinics of North America*, 9(2):179–87, 2001.